MUORGANIC/INORGANIC NANOSTRUCTURED MATERIALS: TOWARDS SYNERGISTIC MECHANICAL AND OPTICAL PROPERTIES

A Dissertation
Presented to
The Academic Faculty

by

Ray Gunawidjaja

In Partial Fulfillment
of the Requirements for the Degree
Doctor of Philosophy in the
School of Materials Science and Engineering

Georgia Institute of Technology
August 2009

ORGANIC/INORGANIC NANOSTRUCTURED MATERIALS: TOWARDS SYNERGISTIC MECHANICAL AND OPTICAL PROPERTIES

Approved by:

Dr. Vladimir V. Tsukruk, Advisor
School of Materials Science & Engineering
Georgia Institute of Technology

Dr. Rina Tannenbaum
School of Materials Science & Engineering
Georgia Institute of Technology

Dr. Kyriaki Kalaitzidou
School of Materials Science & Engineering
Georgia Institute of Technology

Dr. David G. Bucknall
School of Polymer Textile & Fiber Engineering
Georgia Institute of Technology

Dr. Meisha L. Shofner
School of Polymer Textile & Fiber Engineering
Georgia Institute of Technology

Date Approved: [June 05, 2009]

To my parents

ACKNOWLEDGEMENTS

This work is in no way conceivable nor would it be plausible with a solitary effort, but collaborations, discussions, inspirations, and encouragements from a countless number of people. My deepest thank is to my advisor, Dr. Vladimir V. Tsukruk for having trusted me to take-on this daunting task. Surely, without his patience, encouragements, and guidance, this task would have been too great to accomplish. Looking back to my first year of graduate school, I have indeed transformed into a wholly different person. Next, I would like to thank my committee members, Dr. Meisha L. Shofner, Dr. Kyriaki Kalaitzidou, Dr. Rina Tannenbaum, and Dr. David, G. Bucknall for their feedbacks and comments on my work.

Funding from the following agencies is gratefully acknowledged: NSF-CBET-NIRT-0506832, DMR-0646958, AFOSR-FA9550-07-1-0056, AFOSR-FA9550-05-1-0209, NSF-DMR-0756273, and NSF-DMR-0308982.

My personal thank goes especially to Dr. Sergiy Peleshanko (Hewlett-Packard Inc.) who had, hand-in-hand, partially bore the burden and challenges which we faced throughout this journey and lavishly shared his invaluable survival skills. I also would like to thank Dr. Chaoyang Jiang (University of South Dakota) who had given me the opportunity to extend my technical skills and Dr. Eugenia Kharlampieva for her advice, assurance, and friendship. Furthermore, I would like to thank Feifei Huang (Chamblee High School) who had enthusiastically lent her adept hands to help me finish this long-

race. Finally, I would like to acknowledge the people who have worked with me side-by-side: Dr. Kirsten Larson-Genson (Purdue University at Lavayette), Dr. Maryna Ornatska (Clarkson University), Dr. Yen-Hsi Lin (Whirlpool, Inc.), Dr. Hyunhyub Ko (University of California at Berkeley), Srikanth Singamaneni, Sehoon Chang, Libin Liu (Yonsei University, Korea), Grady A. Nunnery, and Ikjun Choi.

Last but not least, I owe my greatest gratitude to my beloved parents who had initially encouraged me to begin this journey. And as the burden grew, they never ceased to give me assurance that I can and I will finish this journey.

TABLE OF CONTENTS

LIST OF TABLES

LIST OF SCHEMES

Page

LIST OF FIGURES

LIST OF SYMBOLS AND ABBREVIATIONS

E	Young's Modulus
α	polarizability
ε	strain
λ	wavelength
φ	volume fraction
σ	stress
<Ae>	excluded area
<Aex>	total excluded area
<Ve>	excluded volume
<Vex>	total excluded volume
AFM	atomic force microscope
AgNW	silver nanowire
AgNPL	silver nanoplate
AgShellNR	gold nanorod with silver shell
AgTipNR	gold nanorod with silver tips
ATRP	atom transfer radical polymerization
AuNP	gold nanoplarticle
AuNR	gold naorod
CLP	controlled living polymerization
LB	Langmuir-Blodgett
SA-LbL	spin assisted layer-by-layer
PAA	polyacrylic acid
PAH	polyallylamine hydrochloride

PEO	polyethyleneoxide
PS	polystyrene
PSS	polystyrene sulfonate
PVP	polyvinylpyrrolidone

SUMMARY

This study utilizes the "bricks" and "mortar" approach to assemble representative organic and inorganic nanostructures into functional hybrid nanomaterials. Zero-dimensional spherical nanoparticles, one-dimensional silver nanowires, and two-dimensional silver nanoplates represent the inorganic functional nanostructured "bricks". Functional-group bearing polystyrene$_2$-polyethyleneoxide$_1$ (PS_2-PEO_1) star polymer, poly(allylamine hydrochloride), and poly(styrene sulfonate) were employed as the "mortar". Mechanical, optical, and electrical properties of the resulting organic/inorganic microstructures were investigated to establish structure-property relationships. Beyond the design, fabrication, and characterization of these novel hybrid nanomaterials two potential applications have been explored: (1) ultra-thin composite film-based pressure sensor and (2) single nanoparticle SERS-based chemical sensors.

One-dimensional silver nanowires (diameter = 80 $\pm$ 5 nm, length = 6 $\pm$ 2 μm) were sandwiched into layer-by-layer (LbL) polyelectrolyte film to yield a series of robust freestanding ultrathin structures (< 100 nm thick). The sandwich architecture allows facile control over volume fraction of silver nanowires ($2.5 \leq \Phi \leq 22.5\%$), and hence their composite Young's moduli. Furthermore, the composite film was found to be conductive (110 – 660 S/cm) within the range of volume fraction in par with percolation threshold predicted for a two-dimensional film. Subsequently, an array of silver nanowires was unidirectionally aligned by means of Langmuir-Blodgett (LB) technique. The unidirectionally oriented silver nanowires were sandwiched into LbL film to give an

anisotropic nanocomposite film with much stiffer (fivefold) mechanical response in the direction of nanowire orientation. In addition to their tailored mechanical and electrical properties, these films are robust and can be easily transferred onto various microfabricated substrates. To fabricate these nanostructures, two experimental techniques were developed to characterize the micromechanical properties of the nanocomposite film and array of one-dimensional metallic nanostructures: interferometry of bulged film and buckling of array of highly-oriented nanowires, respectively.

Next, using the same silver nanowire building block a different design of organic/inorganic hybrid nanostructures was explored. With the aid of a three-arm (X-PEO)1-(PS1-Y)2 star polymer linker, spherical gold nanoparticles were assembled onto a silver nanowire surface. We demonstrated that such hybrid, silver-gold nanowires resembling nanocobs, possess significant SERS ability and can serve as bright anisotropic SERS-markers for Raman-based chemical sensor. The influence of core nanostructure geometries (1-D silver nanowire versus 2-D silver nanoplates) were subsequently investigated for their single-nanoparticle hybrid SERS-enhancing ability and control over optical plasmon absorption within the visible and near infrared range. In the latter design, an improved design of SERS-nanostructure was explored by replacing the three-arm star polymer with polyelectrolyte “mortar” which can absorb chemical analytes into the intra-particle “hot-spots”.

CHAPTER 1

INTRODUCTION

1.1. Functional micro-nano structures: current state of the art

Inorganic nanostructures at 1-100 nm exhibit properties that are different from their bulk counterparts; [1, 2, 3] they can be defect-free and can exhibit unusual or much improved mechanical, optical, and electrical properties. In microelectronics, reduction in size is directly proportional to increased performance. In other types of technologies, miniaturization is a general trend; some examples include nanoreactors [4] and nanocontainers. [5]

A functional micro-nano structure can be fabricated using a classical top-down approach. [6] This involves taking a starting material and carving it down to the desired nanostructure into well-defined shapes and quality, akin to carving a statue from a block of marble. This approach is utilized in semiconductor industries for transistor fabrication that is down to submicron-scales in dimensions. The starting block of material is first covered with a thin layer of polymer, known as photoresist. Next, a protective mask having the desired design pattern is placed over the starting block of material before exposing the coated block of material to light radiation. Subsequently, the light radiation within the exposed region alters the solubility of the resist. Depending on the choice of the resist, it can either become soluble (positive resist) or become insoluble (negative resist) in a developing fluid following the light exposure. The desired pattern is then achieved by etching away the exposed region of the block of material. Finally, the

remaining protective resist is removed to reveal the patterned device. The precision and the quality of the product are determined by the wavelength of the radiation.

On the opposite end, a bottom-up approach requires the availability of distinctive blocks for the construction of a complex hierarchical structure, which is analogous to Lego^{TM} bricks constructions (Figure 1.1a). This necessitates the ability to synthesize nanostructured building blocks with different compositions, sizes and shapes, which indeed have been widely explored in the past years with diversed elemental compositions across the periodic table. [7, 8] Nanowires, nanocubes, nanotriangles, nanospheres, nanoplates, nanobelts, nanoplates, nanostars and nanorods are some examples of nanostructured materials that represent basic building blocks in the field of nanotechnology (Figure 1.1b and Figure 1.1c). In comparison to zero-dimensional structures like nanodots or nanoparticles, one-dimensional nanowires and nanotubes possess additional degrees of freedoms for assembly leading to anisotropic properties. [9]

Another challenge associated with a bottom-up approach is the ability to rationally assemble them precisely over a large area, which will be discussed in section 1.3. Such knowledge is critical in designing rational and useful systems, which is the main focus of this research. Functionality, in addition to well-defined assembly, lies on measurable properties which maybe unique (novel) or simply synergistic of the particular make-up of the assembled structure. [10]

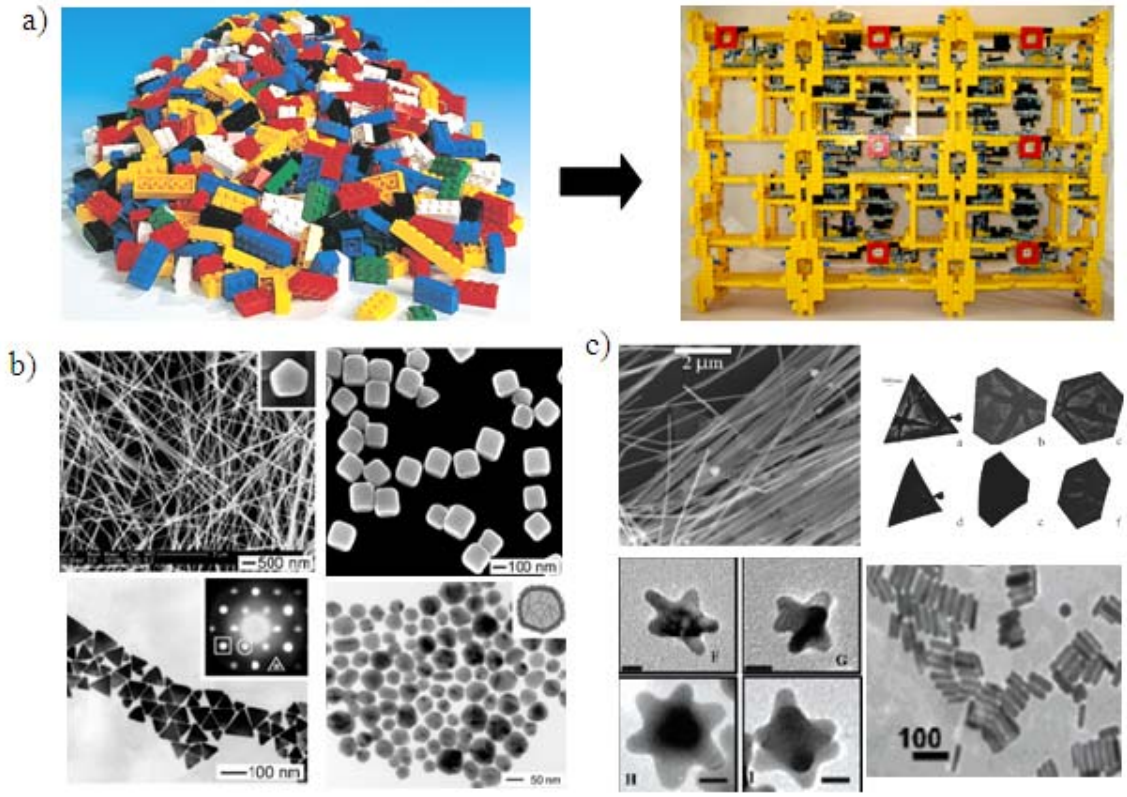

Figure 1.1. (a) individual Lego™ bricks and replica of a multi-story parking-lot made of Lego™ bricks. [11] Representative nanoparticles with well-defined shapes: (b) Silver [12, 13] and (c) Gold. [14, 15, 16, 17]

1.2. Optical and mechanical properties of noble metallic nanoparticles

In addition to their facile synthesis, metallic silver and gold in the nanoscale is a particularly interesting class of plasmonic materials. Since the electrons of silver and gold nanostructures are weakly bound, when exposed to electric field they oscillate from and beyond the neutral state resulting in charge distribution.[18] In nanoparticle case, such oscillation is confined and is also known as localized surface plasmon resonance, LSPR (Figure 1.2a). This is in contrast to a bulk film of silver or gold, where the oscillating

electron could propagate anywhere along the infinitely spacious planar surface, and therefore is not localized and simply called surface plasmon resonance (SPR).

LSPR has a characteristic resonance frequency which, at that particular frequency, strongly absorbs the wavelength of light. The wavelength absorption occurs in the visible range of light and it is distinctive to its shape, dimensions, inter-particle distance, and for—non-isotropic nanoparticles—orientation, as supported by numerous theoretical models (Figure 1.2b). [19] The characteristic plasmon absorption at a certain wavelength of visible light is evident in colored stained glass (burgundy, red, purple, etc.), which indeed contains finely divided colloidal gold or gold nanoparticles.

The oscillating electrons in the presence of a suitable light radiation that is responsible for the LSPR phenomenon amplify the localized electric field which greatly enhances the characteristic Raman shifts of certain organic molecules within their vicinity, which is the fundamental of surface enhanced Raman spectroscopy (SERS). [20] Raman-based sensor eliminates the need of molecular labeling, it is molecular specific, and can be highly-sensitive (down to a single molecule), as demonstrated by Kneip *et al* and Nie *et al*. [21, 22] This was attributed to a simultaneously operating long-range electromagnetic (EM) and short-range chemical (CHEM) enhancement mechanisms. It is now well-established that EM enhancement is best obtained at the interstitial sites between closely neighboring nanoparticles, [23, 24, 25] which as Lee *et al* have shown, changing silver inter-nanowire gap from 35 nm to 10 nm increased the SERS intensity by 200-fold. For the above reasons, silver and gold nanoparticles are gaining popularity as

potential optical-based sensor. [26] Some recent examples of functional organic/inorganic hybrid nanostructures include Raman-based molecular rulers, [27] nanoscale pH-meter, [28] and nanorod-coated thermoresponsive microgel for medical applications. [29, 30] Detailed discussions on surface enhance Raman scattering (SERS) due to gold and silver nanoparticles can be found in Appendix A.

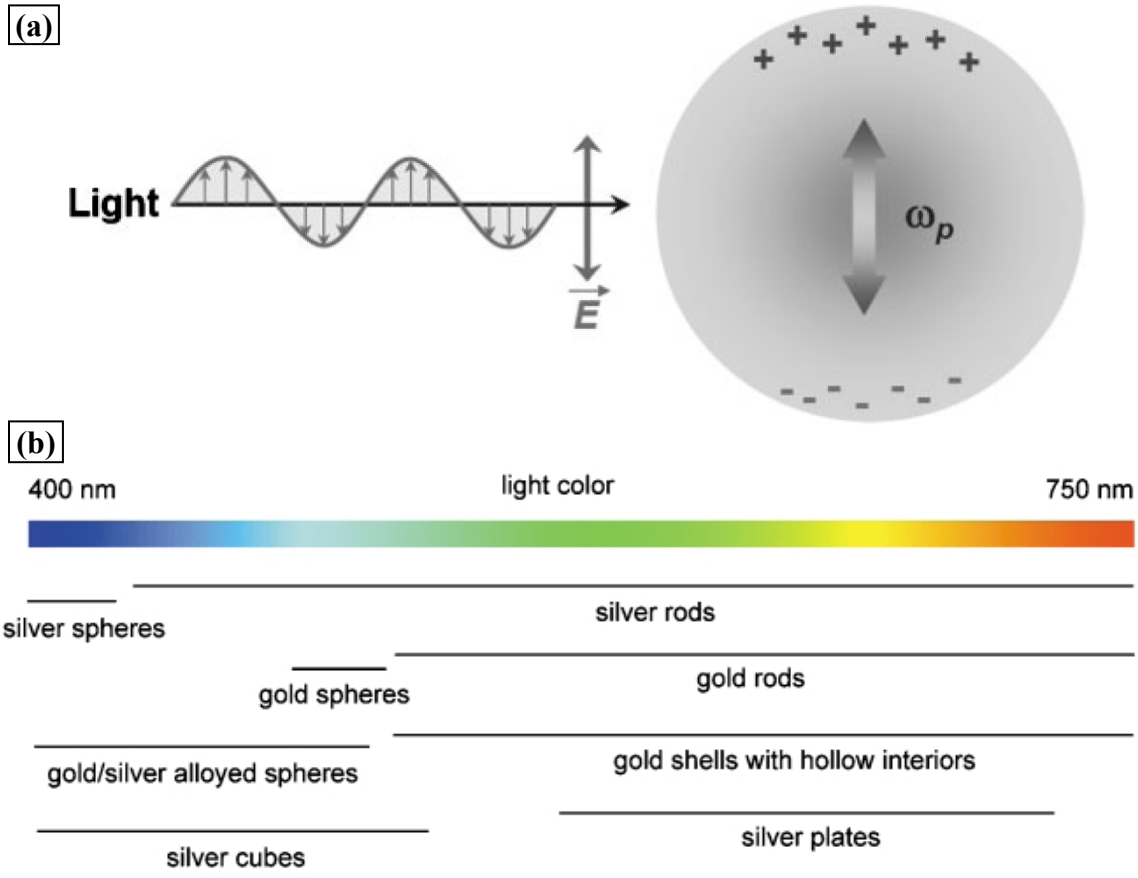

Figure 1.2. (a) Plasmon oscillation at a characteristic plasmon frequency, ω_p, within a spherical metallic nanoparticle in the presence of exciting laser. [18] (b) Plasmon absorption spectrum of some representative shaped gold- and silver-nanoparticles within the visible region. [31]

Another useful property in metallic nanoparticles is their high Young's modulus compared with polymeric materials which makes it useful as mechanical reinforcements in organic/inorganic composite structures. [81] A number of theoretical simulations have been undertaken to elucidate their elastic and plastic deformation under tesile and bending forces. [32, 33] It is worth noting that metallic nanocrystals possess a certain crystalline orientation that in turns dictate their mechanical property. For instance, the Young's modulus of 1D silver nanowire was measured to be 88 $\pm$ 5 GPa by nanoindentation technique on its surface. [34] This value is in par with bulk silver. However, the Young's modulus of a single crystal silver measured along the (100) direction is found to be 124 GPa. [35] The effect of crystal orientation on the mechanical property of metallic nanoparticle can be further seen for gold. Gold nanorods synthesized by wet chemical method have five-times smaller Young's modulus than bulk gold, E = 79 $\pm$ 1 GPa, [36] and a size-dependent Young's modulus was reported for spherical gold nanoparticles. [37] The mechanical property of an organic/inorganic composite film can be well-estimated using the rule of mixture, or the Halpin-Tsai equation for fiber reinforced composites (see Appendix B).

1.3. Shape control of geometrically-defined inorganic nanoparticles

Few of the methods that have been proven successful to synthesize geometrically-defined nanoparticles include: [38] (1) sol-gel process, (2) chemical precipitation, (3) hydrothermal or solvathermal synthesis, (4) pyrolysis, (5) vapor deposition, and (6) soft-template assisted growth, as briefly discussed below.

(1) Sol-gel pocess is a solution technique where the chemical precursor (metal oxides or metal alkoxides) is dissolved in a solvent which undergo hydrolysis condensation—inorganic polymerization—upon heating forming oxo (M-O-M) or hydroxo (M-OH-M) bridges, depending on whether metal oxide or metal alkoxide was used as the precursor. Such transformation is referred to as sol-to-gel transformation because the sol evolves into a gel-like biphasic system due to the formation of the oxo and hyroxo bridges that result in the formation of either a discrete of continuous particles. Metal oxide nanoparticles are typically synthesized in this manner (e.g.TiO_2, SiO_2, SnO_2, ZnO). [39]

(2) Control over the kinetics of nucleation and particle growth in a homogeneous solution can lead to the precipitation of monodisperse nanoparticles. Since nucleation occurs spontaneously when the solution reaches a critical supersaturation of the salt precursor, the monodisperse nanoparticles can be achieved via controlled release of the salt precursor. Some factors that are essential to this process are precursor concentration, pH, and temperature (e.g. γ-Fe_2O_3). [40] Various shapes of $Cu(OH)_2$ nanostructures (nanowires, rectangles, seedlike, beltlike, and sheetlike) were grown in solution when the NaOH concentration is changed with respect to the $Cu(NO_3)_2$ salt precursor. $Cu(OH)_2$ can then be transformed into CuO by subsequent heat treatment for half an hour at 80 ºC. [41]

(3) Some inorganic substances dissolve in water at elevated temperature and pressures and subsequently recrystallize from the fluid and transforming the shape, size, and crystal structure. This process is called hydrothermal if water is used as the solvent,

[42] but it is called solvathermal process if other solvents are used instead. Non-spherical nanoparticles have also been obtained from this method (e.g. nanorods, nanowires, and nanotubes of TiO_2). [43, 44, 45]

(4) Pyrolysis is a process where a chemical precursor is decomposed into a solid compound that is accompanied by evaporation of the unwanted waste under a given thermal process. A controlled thermal process is necessary to yield a product that is monodispersed in shape and compositions that is best achieved when the reaction is done in solution where the reaction rate is greatly reduced. Protecting agents in the form of polymer is sometimes used as well. Some examples include $CoWO_4$, α-Al_2O_3, GaN, and ZnO. [46]

(5) As the name implies, in a vapor deposition process the precursor is first vaporized and deposited via absorption onto the appropriate catalysts to grow into a well-defined structure. This method has been utilized to grow carbon nanotube forests with high aspect-ratio, [47] but also applicable to other types of materials e.g. In_2O_3, BN, LaB_6, MgB_2. [48] Structures other than one-dimensional column have been reported as well (e.g. ZnO nanotetrapods). [49]

(6) A surfactant is usually represented by a molecule having a hydrophobic tail and a hydrophilic head. At a certain minimum concentration in a solvent medium, they form aggregate (or micelle). If the solvent is hydrophilic, *e.g.*, water, the hydrophobic tail is oriented inside the aggregate to avoid contact with water and the hydrophilic head

is oriented outside the aggregate to contact with the surrounding water. In the opposite case, if the solvent is hydrophobic, *e.g.*, hexane, the hydrophobic tail is oriented outside the aggregate to contact with hexane and the hydrophilic head is oriented inside the aggregate to avoid contact with the surrounding hexane. This is known as reverse micelle. The geometry and size of reverse micelles is determined by their chemical compositions and chemical structures, which can be predicted by calculating the packing factor, $V/\alpha_0 l_c$. V is alkyl chain volume, α_0 is headgroup area, and l_c is the maximum length to which the alkyl chain can extend. These micelles can therefore function as soft-template for the reduction of metallic salt precursor in solution. [50, 51] Gold nanoparticles derivatives (e.g. nanorods, nanoplates, nanospheres) have been synthesized in this manner. [52]

1.4. Soft-template assisted growth of FCC metallic nanoparticles

The synthesis of geometrically-defined nanoparticles has particularly been successful for fcc metals (Pd, Pt, Au, Ag) in grams quantity, where polyvinyl pyrrolidone (PVP) functions as the soft-template. [53] This technique involves metallic salt precursor, ethylene glycol reducing agent (EG), and polyvinylpyrrolidone (PVP) capping agent that are heated to elevated temperature. [54, 55] Within the early phase of the reaction, the metal ions precursor is reduced into elemental metal and subsequently forms elemental metal clusters (Figure 1.3). Below the critical nucleation size the silver cluster re-dissolves into solution, but passed the critical nucleation size the cluster continues to grow. Further growth occurs *via* Oswald ripening, where smaller clusters are consumed by larger clusters. The small clusters lower its surface energy by being incorporated onto larger

clusters. To lower the surface energy silver nuclei incorporate twin-boundary defects. Change in defect structure is unfavored as the nuclei grow because it will require additional driving force, therefore the shape of the nuclei from which a crystal grows determine its final shape. In a typical polyol reduction of metallic salt three types of nuclei are formed in the Boltzmann-like distribution that is comprised of single-crystal, multiply-twinned decahedron, quasi-spherical muti-twinned crystal seeds. The five-fold twinned decahedron is the most abundant because its free energy is the lowest.

The ability to selectively enrich a particular nucleus at the start of a polyol reaction means that subsequent nanocrystal growth will result in metallic nanoparticles with a certain geometrical shape. This is determined by the rate of reduction and the $AgNO_3$ precursor to PVP capping agent ratio. Controlled growth subsequently take place due to specific adsoption of PVP onto the {100} facet, which confines the growth in the direction of the exposed facet. In the polyol synthesis of silver salt precursor for example, silver nanocube, silver nanowire, and silver nanosphere can be grown from singly-crystal seed, 5-twinned decahedral seed or multi-twinned quasi-spherical seed, respectively (Figure 1.3).

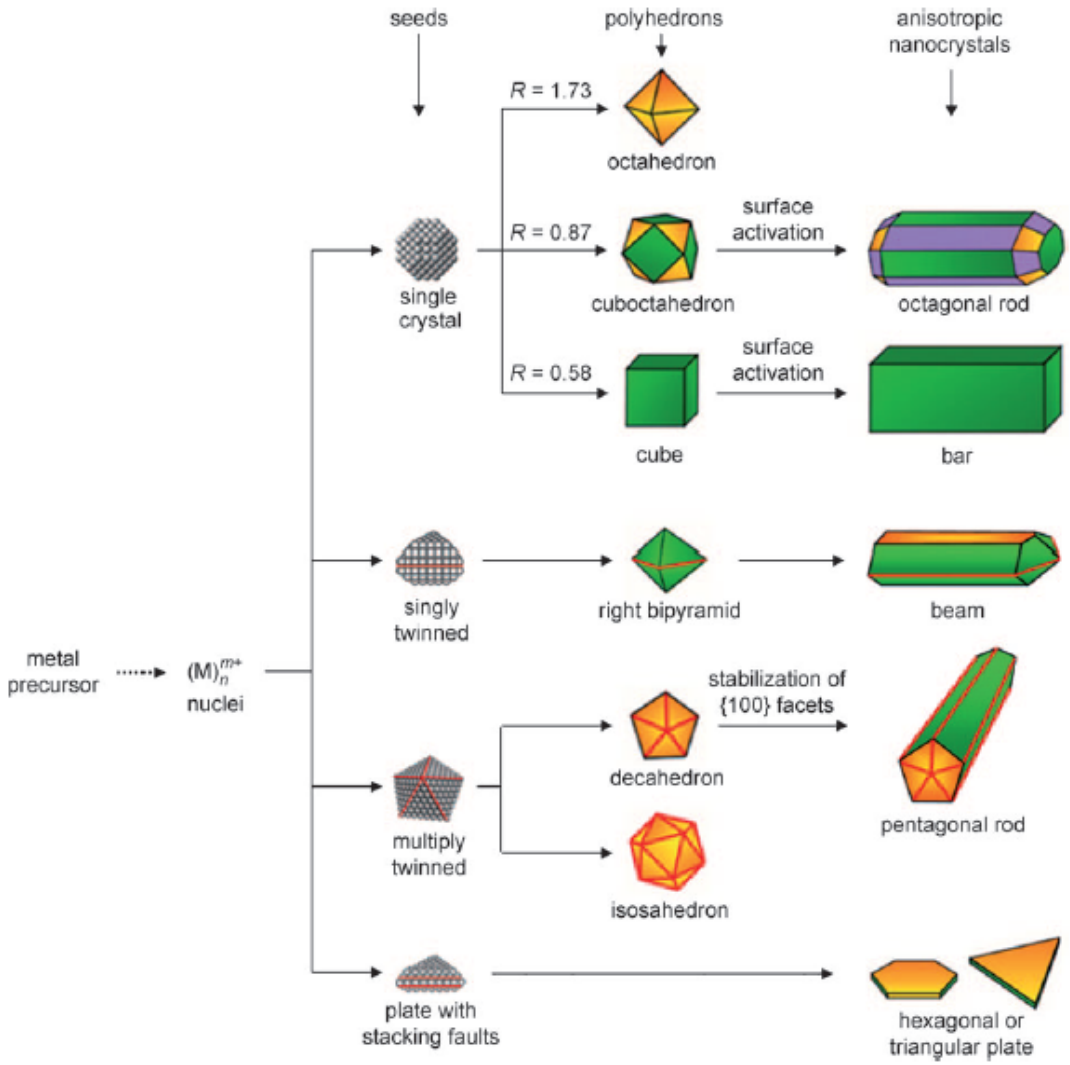

Figure 1.3. The evolution of fcc crystal formation which begins with the reduction of metal salt precursor into silver clusters formation, and followed by nucleus formation, in the form of single crystal, singly-twinned, multi-twinned, and plate with stacking-fault. The various crystalline facets, {100}, {111}, and {110} are represented by green, orange, and purple colors, respectively. The red lines represent twin planes. R is the ratio between the growth rates along the <100> and <111> directions. [53]

Slow decomposition or reduction of silver nitrate precursor can lead to the formation of nuclei and seeds having a random hexagonal close packing (rhcp), which contains stacking faults and/or twin planes. Such kind of nucleating seed is a high energy structure, and has been known as kinetically controlled. It grows into a plate-like seed that is bounded by {111} facets along the top and bottom surfaces, that is separated by the stacking faults and/or twin defects (Figure 1.4a). Due to the large specific surface area provided by their two-dimensional shape, nanoplate particles possess much free energy that is not thermodynamically favored. Therefore, their nucleation and growth is only achievable via kinetic pathways, as follows: a) slow precursor decomposition or reduction, b) employing a weak reducing agent, c) coupling the reduction to an oxidation process, or d) taking advantage of Ostwald ripening. [56] Hence, the underlining principle for a two-dimensional nanoplate growth is to maintain an extremely low concentration of metal atoms in solution to prevent a three dimensional growth into a polyhedral structure, but rather a two-dimensional growth is to be preferred.

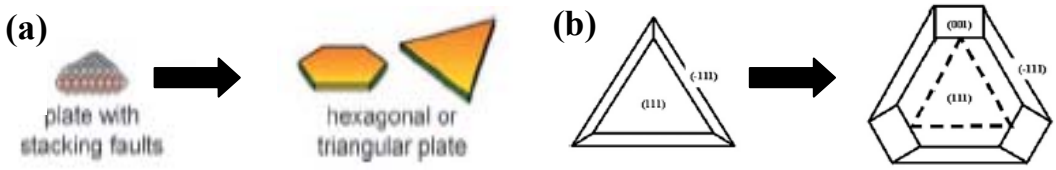

Figure 1.4. (a) Two-dimensional nanoplate is formed from seed particle that contain stacking faults. Red lines indicate twin planes. [56] (b) Geometrical transformation of silver nanoplates from triangular to hexagonal nanoplate.

Two-dimensional silver nanoplate, which is bounded by {111} planes, can be prepared using DMF solvent rather than polyethylene glycol in the presence of PVP capping agent. Wang *et al* proposed that silver nanoplates grow from a single-crystal seed through two-dimensional epitaxial growth (Figure 1.4b). [57] A slightly different growth condition where sodium citrate was used in place of PVP capping agent resulted in a similar silver nanoplate structures. For this system, Jia *et al* suggested that the anisotropic growth is due to faster growth along the (100) side planes than the (111) top and bottom planes, as a result the (100) face vanished quickly and it resulted in the formation of a triangular plate that is bounded completely by the (111) plane. As the capping agent is exhausted the inhibition of growth along the (111) side plane is diminished and the triangular plate transforms into hexagonal plate. [58]

1.5. Assembly of nanostructured materials

Plethora activities involving a bottom-up assembly of nanostructured materials have been reported by means of surfactant, [59] electrospinning method, [60] atomic force microscopy, [61] DNA-assisted assembly, [62] Langmuir-Blodgett technique, [63] controlled nanocrystal growth, [64] template-assisted, [65] and use of physical forces [66, 67] (e.g. electrical, magnetic), among them, self-assembly is becoming the popular choice for manipulating these nanostructures over a wide area. This is due to limitations associated with, for example, atomic force microscopy that can be time consuming or UV lithographic technique which has limited resolution. Moreover, these equipments can be quite costly. Room-temperature solvent-assisted assembly of functional inorganic and organic materials facilitated by self-assembling blocks is the cheaper alternative to conventional

lithography and vacuum deposition techniques for the fabrication of integrated hierarchical system

Shenhar *et al* had classified the self-assembly of inorganic nanoparticles into: (a) 1-D assembly as control of interparticle distance, (b) 2-D uniform assembly on a planar substrate, (c) 3-D control of nanoparticles aggregate shapes and sizes (Figure 1.5). The simplest example for control of interparticle distance in a 1-D scheme is to use n^{th} generation dendrimer. Rotello and co-workers used poly(amido amine) PAMAM dendrimer to control the distance between gold nanoparticles. As confirmed from small-angle X-ray scattering (SAXS), the distance between gold nanoparticles increase with dendrimer generation. [68] And recently, Maye *et al* demonstrated a two-step nanoparticle dimer assembly in high-throughput, which is rarely achieved in solution-based assembly, by first confining isolated DNA-encoded gold nanoparticles on a solid support and subsequently attaching a second nanoparticle on the top-exposed side of the tethered nanoparticle. The dimer nanoparticle can then be released from the solid support. [69]

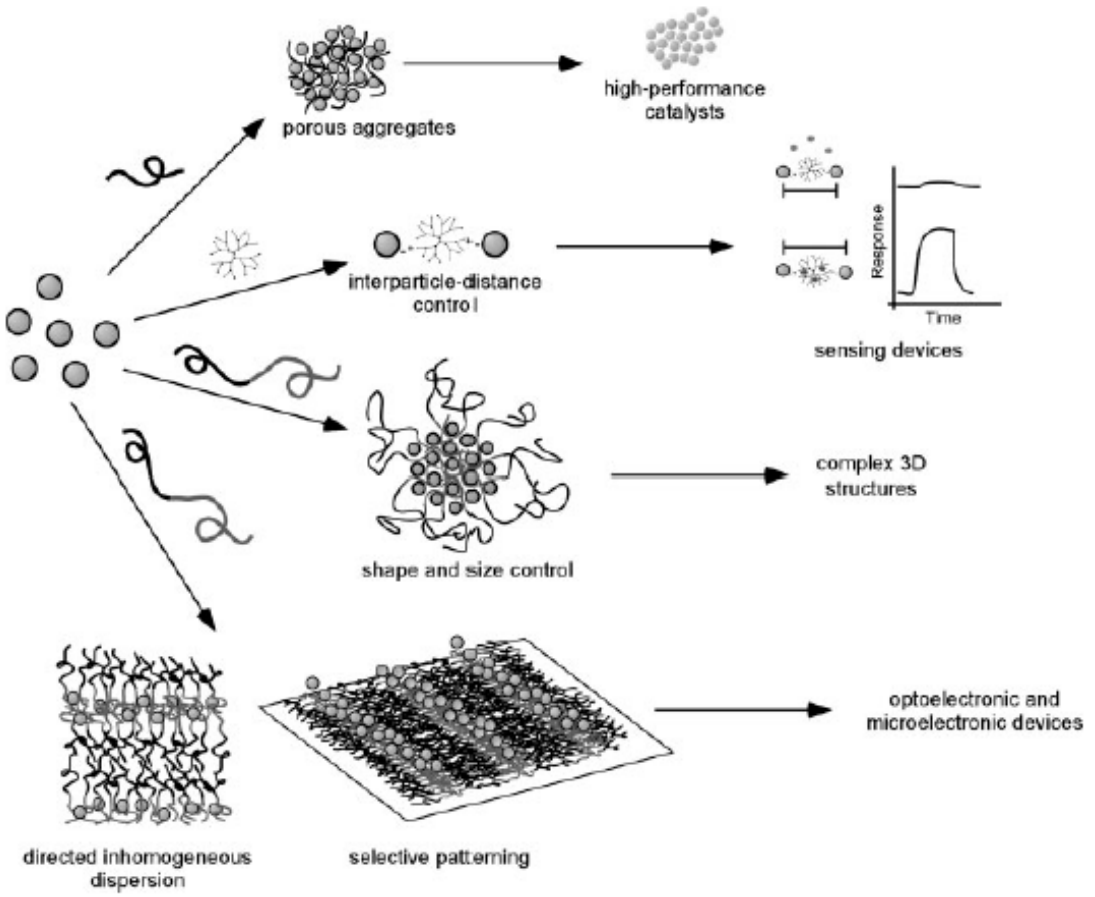

Figure 1.5. Various assembly approaches using organic templates in 1-D, 2-D, and 3-D schemes.

Two-incompatible polymeric blocks that phase separate into distinct spherical or lamella domains can function as a pre-patterned 2-D template for nanoparticles assembly. A selective interaction between the nanoparticle surface with either of the phase-separated domains leads to organized assembly. Bockstaller *et al* have selectively confined oligo-styrene functionalized gold nanoparticles within the polystyrene domain in a polystyrene-polyethylene/propylene block copolymer (PS-PEP). [70] Alternatively, two-dimensional assembly of inorganic nanoparticles can be obtained at the air-water

interface using a technique known as Langmuir-Blodgett (LB), provided that they form a stable monolayer on the water surface.

For instance, gold nanoparticles (3.0 $\pm$ 1.0 nm) functionalized with mixed hydrophilic poly(N-isopropylacrylamine) (NIPAAM) and hydrophobic polystyrene (PS) possess an amphiphilic behavior at a room temperature at the air-water interface and forms well-defined microstructure as viewed on solid substrate (Figure 1.6a).[71] Its Langmuir isotherm shows distinctive plateau region, which is characteristic for amphiphilic monolayer (Figure 1.6b). From the Langmuir isotherm, transitions are seen at an area per molecule that is larger than the area occupied by a single gold nanoparticle. TEM image of the functionalized gold nanoparticle shows that the uniform spacing between gold nanoparticles is determined by the molecular weight of the polymer shell.

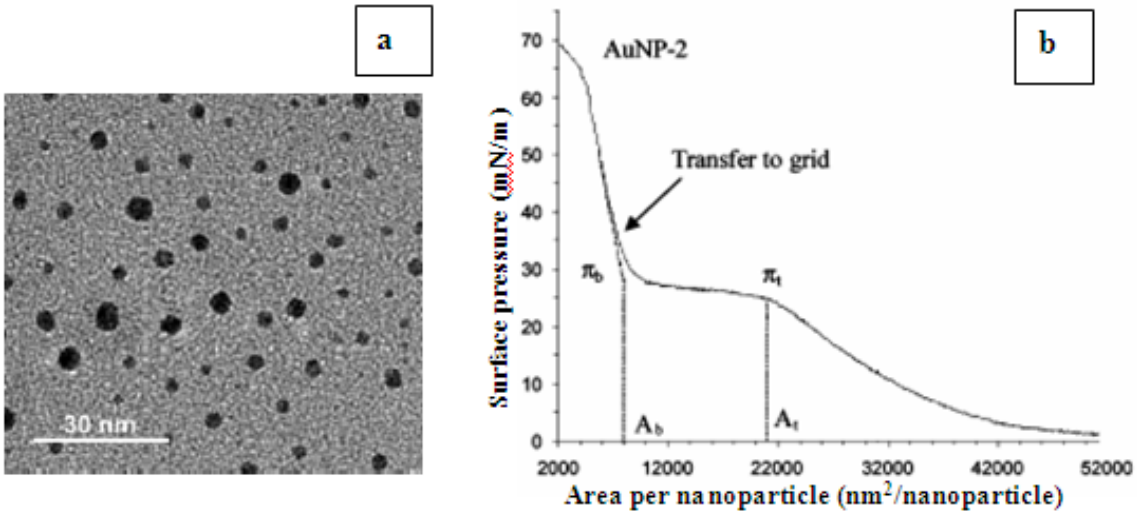

Figure 1.6. (a) TEM image of NIPAAM-PS functionalized gold nanoparticle and its (b) Langmuir isotherm.

In contrast to the zero-dimensional gold nanoparticles, one-dimensional nanoparticles can exhibit anisotropy. Kim *et al* demonstrated that one-dimensionl $BaCrO_4$ nanorod stabilized with 2-(ethylhexyl)sulfosuccinate sodium salt (AOT) surfactant at the air-water interface could form a nematic phase (Figure 1.7a). A more complex assembly of one-dimensional nanoparticle is a three dimensional assembly of bi-layer silicon nanowires stack, where the bottom array is 90º in orientation with respect to the top layer (Figure 1.7b). [72] Another recent intriguing example of a three-dimensional nanoparticles assembly is the works of Nykypanchuk *et al* and Park *et al*. Both teams have used DNA linker to assemble two distinct nanoparticles into a body-centered-cubic arrangement as in CsCl crystals. [73]

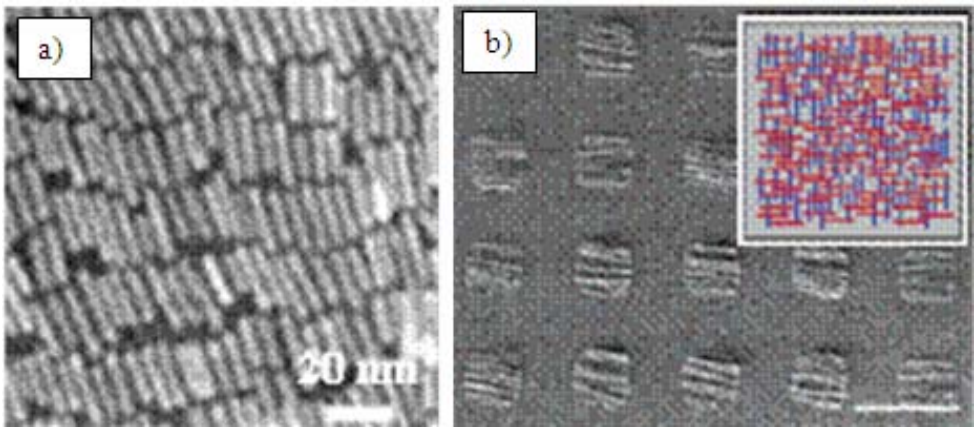

Figure 1.7. Langmuir-blodgett assisted assembly of: (a) hydrophobic $BaCrO_4$ nanorod [74] and (b) silicon nanowires.

In the point of view of micro-nano materials fabrications layer-by-layer (LbL) assembly is a facile approach for incorporating organic/inorganic structures. In contrast to other techniques, such as chemical vapor deposition, atomic layer deposition, or

molecular beam epitaxy, LbL approach does not require well-controlled and sophisticated pieces of equipment. [75] LbL approach is a wet technique where, typically, two oppositely charged polyelectrolytes are sequentially adsorbed onto a solid substrate to form a film with controlled thickness (Figure 1.8). Inorganic component can be incorporated to give a composite structure. A highly-tunable property of LbL film can be successfully designed depending on the availability of the functional polymeric matrix and functional inorganic filler components. The readers are referred to the following reviews for further information on LbL assembly: Kotov *et al*, [76] Hammond *et al*, [77] Tsukruk *et al*, [78] and Sukhishvili *et al*. [79]

Since the design is not limited to a 2D film structure, LbL-based micro-nano structures have found applications in drug delivery systems, battery electrolytes, and sensors. That is, a 3D film has been successfully fabricated if the LbL film is built upon a 3D substrate. [80] Jiang *et al* showed that a freestanding LbL-based nanometer-thick film containing gold nanoparticles freely suspended over a cavity can serve as a highly-sensitive deflection-based sensor. [81] The unique feature of this design is, in contrast to most inorganic sensors, it does not require cooling. Kotov and co-workers had also shown that an exceptionally strong single wall carbon nanotube reinforced LbL film (σ_{ult} = 220 $\pm$ 40 MPa) with a tensile strength approaching ceramics could be fabricated, [82] and a nacre-like nanocomposite that fails at σ_{ult} = 320 MPa. [83]

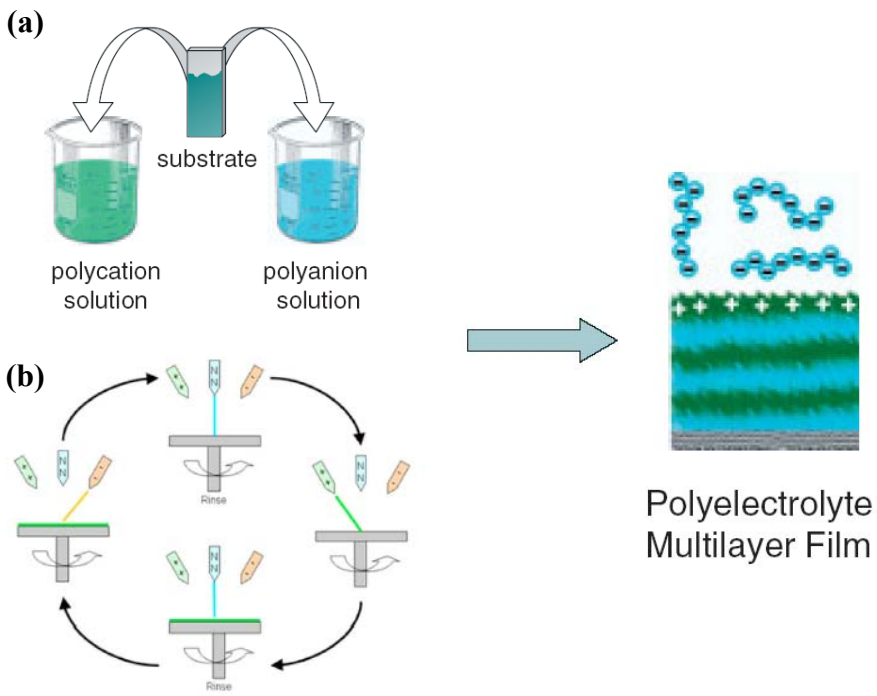

Figure 1.8. LbL assembly of alternating polycation and polyanion on a flat substrate by means of: (a) dip-coating[75] or (b) spin coating. [84]

1.6. Challenges and motivations of current study

Bottom-up assembly is a promising path towards the design of functional materials because it allows control over compositions and, in contrast to the top-down approach, is not severely limited limited in spatial resolution. Furthermore, there is growing varieties of techniques discovered for the synthesis of well-defined inorganic building blocks that serve as the necessary starting components for a bottom-up assembly, which spans from a dry-state to solution-based techniques. Solution-based technique is often preferred because it does not require expensive setup. For solution-based technique, one can choose between templated versus non-templated approach. In a templated approach, the formed nanoparticles are usually stable and well-dispersible in

various solvents. On the other hand, non-templated approach leads to bare-nanoparticles that allow surface modifications, however, they maybe prone to aggregations.

If inorganic nanoparticles provide the functional properties, organic molecules could aid their assembly into rational hierarchical structures. A wide range of organic molecules containing specific functional groups are available for this purpose. For instance, a two- and three-dimensional polymeric film with controlled nanometer-resolution thickness can be easily fabricated using LbL technique, and block copolymers are capable of phase-separating into patterned domains with defined nanoscale spacings. Furthermore, selective deposition of nanoparticles onto patterned block copolymer domain yields a uniform nanoparticles array. The assembly of LbL film requires ionic interaction that is provided by charged functional groups, while the formation of patterned block copolymer domains can be controlled by functional groups within each polymeric block.

While much fundamental studies have been achieved in understanding the mechanisms of geometrically-specific nanoparticles growth and surface modifications, the next step was to combine the organic/inorganic nanostructures into 1-D, 2-D, and 3-D micro-nano-structures has not been explored in great detail. Studies have concluded that precise control of noble nanoparticles over inter-particle distance and configurations can lead to the designs of functional micro-structures with tunable optical, mechanical, and electrical properties, but in order to realize the full capability of hybrid nanostructures

with performance exceeding the current technology, the gap between fundamental study and engineering needs to be bridged.

The general challenges associated with the bottom-up assembly of such organic/inorganic nanostructures into functional micro-nano-materials can thus be summarized as follows: (1) many nanoparticles that possess novel properties have only been synthesized in a low-yield, (2) they tend to aggregate due to their high-surface area, (3) it is difficult to obtain a uniform long-range assembly over a large area, (4) in contrast with bulk materials, micro-nano-structures are harder, or even imposible, to handle, and finally (5) there is limited number of characterization techniques to understand their physical properties at the nanoscale.

CHAPTER 2

RESEARCH GOAL AND OBJECTIVES

2.1. Research goal and objectives

The current work is aimed to utilize the fundamental knowledge of shape-controlled nanoparticles synthesis and their surface modification using functional polymers to systematically engineer a proof-of-concept design of novel nanostructured materials over large microfabricated areas. The ultimate goal of this work is to understand the fundamentals of bottom-up assembly of inorganic and organic building-blocks for the designs of engineered functional hybrid organic/inorganic large-scale micro-nano-structures with focus on synergistic mechanical, electrical, and optical properties (Figure 2.1).

We have selected silver and gold nanostructures as the representative inorganic building blocks due to their facile and high-yield synthesis, well-established surface chemistry, and shape-dependent optical plasmonic properties. For the hierarchical assembly of these inorganic blocks, we employed the metal-ligand binding interactions using the thiol chemistry and ionic interactions. The representative inorganic blocks are zero-dimensional spherical gold nanoparticles, one-dimensional silver nanowires, and two-dimensional silver nanoplates. The representative organic building blocks are positively- and negatively-charged polyelectrolytes and three-arm star polymers.

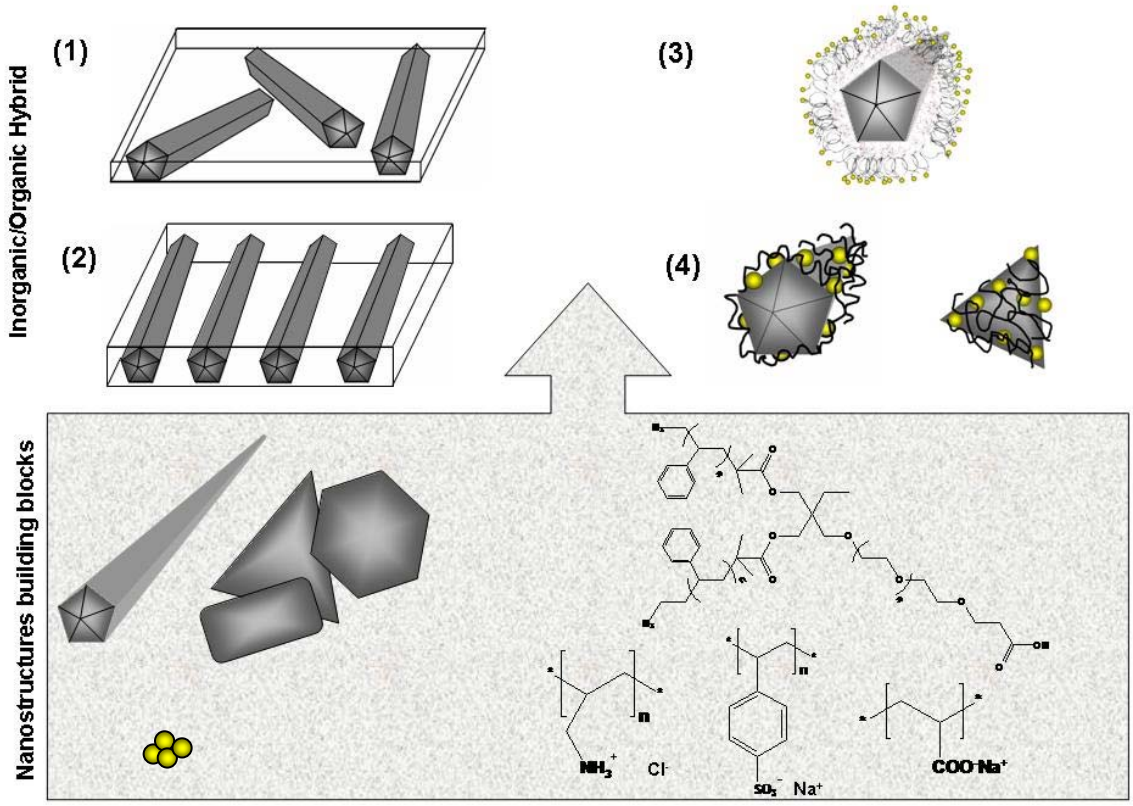

Figure 2.1. (Top) The two classes of bricks and mortar blocks, respectively: 0-D spherical gold nanoparticles, 1-D silver nanowire, and 2-D silver nanoplates and end-functionalized star polymer and polyelectrolytes. (Bottom) Four designs of hierarchically assembled inorganic/organic hybrid microstructures: (1) randomly-oriented and (2) unidirectionally-oriented silver nanowire reinforced LbL film. (3) Covalently-bound and (4) electrostatically-bound bimetallic silver-gold core-shell nanostructures.

2.2. Objectives

The design, fabrication, and characterization of the organic/inorganic micro-nano-structures are undertaken in several stages in the order of increasing design complexity with focus on mechanical, electrical, and optical properties, as follows:

a) Mechanically robust and electrically conductive freestanding films with controlled mechanical properties and can be handled and transferred onto various substrates
   - Synthesize one-dimensional (1D) metallic silver nanowires.
   - Incorporate the 1D silver nanowires into an LbL film with controlled density.
   - Relate nanoparticles volume fraction with mechanical properties of the silver nanowire–reinforced LbL composites.

b) Mechanically anisotropic freestanding film
   - Align 1D nanostructures array by Langmuir-Blodgett technique.
   - Incorporate the aligned nanoparticles array into LbL film.
   - Relate mechanical properties of anisotropic composite film with silver nanowires orientation.

c) Single-nanoparticle anisotropic SERS structures with a broad plasmon absorption
   - Synthesize 0D gold nanoparticles and 1D silver nanowires.
   - Attach 0D gold nanoparticles onto a 1D silver nanowires.
   - Compare SERS effect due to a bare 1D silver nanowires with 0D gold nanoparticles-decorated 1D silver nanowires.

d) Designs of single-nanoparticle SERS substrate with various geometries
   - Synthesize 0D gold nanoparticles, 1D silver nanowires, and 2D silver nanoplates.
   - Attach 0D nanoparticles onto the 1D and 2D nanoparticles
   - Quantify and relate SERS effect with nanoparticles geometry.

e) Elucidation of mechanical, optical and electrical properties of freestanding organic/inorganic nanocomposite films and silver-gold hybrid nanostructures
   - Developed micromechanical characterization technique to measure Young's modulus, toughness, ultimate stress, and ultimate strain of nanocomposite.
   - Measure electrical conductivity of silver nanowire-reinforced LbL film.
   - Measure optical absorption of silver-gold hybrid nanostructures.

- Compare SERS performance of various designs of one- and two-dimensional core-shell hybrid nanostructures.

2.3. Thesis Organizations

Chapter 1: This chapter provides the general overview of micro-nano structures fabrications, *i.e.*, top-down approach versus bottom-up approach. The properties, preparation and the various assembly techniques of the starting components for bottom-up assembly are also discussed here.

Chapter 2: Research goal and objectives of the current study are delineated in this chapter.

Chapter 3: Experimental procedures including nanoparticles synthesis, materials preparations, and characterization methods are described in this chapter.

Chapter 4: At the initial stage, an array of randomly oriented one-dimensional silver nanowires was sandwiched into polymer film by means of LbL technique. The sandwich approach allows control over density of silver nanowires, and LbL technique allows control over film thickness within the nanometers range (< 100 nm). Control over silver nanowires density can lead to tailored mechanical properties. One-dimensional filler possess high surface area, which is essential for optimum matrix-filler interaction. Furthermore, the critical percolation network for one-dimensional filler is less than zero-dimensional filler to obtain an electrically conductive film. Since the nanowires are randomly oriented, this design of nanocomposite films exhibit isotropic mechanical

properties. The fabricated film is robust, can be made freestanding, and can be easily transferred onto various substrates.

Chapter 5: Next, the fabrication of anisotropic silver-nanowires reinforced nanocomposite film is described. The one-dimensional silver nanowires were chemically functionalized with polyethylene-oxide to render it amphiphilic. The polyethylene oxide ligand is bound onto the silver nanowire surface by thiol terminal group. The amphiphilic silver nanowires float on water surface and could be unidirectionally oriented by parallel compressions, analogous to "logs on river". The unidirectionally oriented silver nanowires were sandwiched into the LbL film to give an anisotropic nanocomposite film.

Chapter 6: Terminal group modification of a multi-arm star polymer, $(X\text{-}PEO)_2$-$(PS1\text{-}Y)_2$, that is to be utilized as an alternative "mortar" component is discussed in this chapter.

Chapter 7: An asymmetrical star polymer linker, $(X\text{-}PEO)_1$-$(PS1\text{-}Y)_2$, with the appropriate terminal groups was then used as a linker to decorate gold nanoparticles onto silver nanowires surface. The resulting silver-gold hybrid nanostructure resembles a nanocob and the $(X\text{-}PEO)_1$-$(PS1\text{-}Y)_2$ organic linker trapped between the two nanoparticles surfaces experienced enhanced Raman scattering (SERS). The extent of this enhancement is polarization-dependent, which is determined by the orientation of the polarized excitation laser with respect to the one-dimensional silver nanowire.

Chapter 8: Subsequently, the star-polymer linker was replaced with polyelectrolyte "mortar", which is capable of adsorbing chemical analytes within the particle-particle "hot-spot". Furthermore, the SERS ability of silver nanowire core and two-dimensional nanoplate core are compared with dense array of bare silver nanowires and silver nanoplates.

Chapter 9: The major lessons from each chapter (Chapter 4 through Chapter 8) are outlined here, and potential applications for the silver nanowire-reinforced LbL films and the silver-gold hybrid nanostructures are discussed as a result of this study.

Appendices A, B, and C: The basic principles behind Raman scattering, surface enhanced Raman spectroscopy (SERS); mathematical equations and matrix operations needed to determine the micromechanical properties of the nanocomposite films studied here; prediction of mechanical properties of fiber-reinforced composite; and the discussions on percolation theory are separated from the main discussions and presented here.

CHAPTER 3

EXPERIMENTAL AND METHODS

3.1. Materials

Silver nanowire synthesis. High-yield silver nanowires were synthesized according to the well-known procedure. [85,86,87] All glassware were washed with soap, *aqua regia*, and rinsed thoroughly with de-ionized water. A 60 mL solution of poly(vinylpyrrolidone) (PVP, 0.36 M, M_n=1.3 million g/mol) in ethylene glycol was heated at 160 ºC under constant stirring for one hour to remove water from the solution. Next, a separate 30 mL solution of silver nitrate in ethylene glycol ($AgNO_3$, 0.12 M) was prepared at room temperature by vigorous vortexing. Sonication or heating was avoided, since it could lead to the unwanted formation of silver nanoparticles. Next, 50 μg of $Fe(acac)_3$ in 0.5 mL ethylene glycol solution was added into the hot PVP solution, followed by dropwise addition of the homogeneous silver nitrate solution. The dropwise addition was done manually by means of pipette. The solution mixture was allowed to stir for a minimum of one hour, or until the solution turns silhouette opaque-gray. The formation of silver nanowires could be easily confirmed from optical microscope with 20x-50x objectives, which is best observed in the dark field mode.

Silver nanoplates synthesis. A 30 mL solution of $AgNO_3$ (0.025 M) was added dropwise at room temperature into a stirring solution of PVP (0.05 M, M_n=40,000 g/mol). [88] The solution mixture gradually turns dark orange during the addition. The solution mixture is contained in an autoclave and then placed in a temperature-controlled oven at a

constant temperature, 165 ºC for 24 hours. The final product is tan-brown, which tends to aggregate into a mirror-like film on the wall of a flask.

Both silver nanowires and silver nanoplates were purified from excess of ethylene glycol and PVP by multiple centrifugations and re-dispersion cycles in methanol.

Gold nanoparticles synthesis. [89] 4.1 mL aqueous solution of gold chloride ($HAuCl_4$.HCl, 30 mM) was mixed with 6.8 mL toluene solution of tetraoctylammonium bromide (TOAB, 25 mM) and vigorously stirred. As soon as all of the gold chloride salt has transferred from the aqueous phase into the organic phase, as seen from the distinctive yellow-orange color, a freshly prepared 4.1 mL ice-cold aqueous solution of sodium borohydride ($NaBH_4$, 0.4M) solution is added dropwise into the two-phase solution mixture. The solution mixture gradually turns dark purple, almost black, accompanied by vigorous bubbling. The final solution mixture is left to stir overnight. The next day, the purple organic-phase is extracted using pipette and washed with 0.1 M sulfuric acid, followed by washing with 0.1 M sodium hydroxide, and finally washed three times with nanopure water. Equal volume of aqueous solution of 4-dimethylaminopyridine (4-DMAP, 0.1 M) is then added to the gold nanoparticles solution. Within one hour, the gold nanoparticles moved into the aqueous phase.

3.2. Fabrication and Characterization methods

3.2.1. Chemical structure characterization

NMR spectroscopy. ^{1}H NMR spectra were obtained using Varian VXR-300 MHz employing chloroform, $CDCl_3$ and methanol, CD_3OD as solvents. Synthesized compounds between 30-60 mg was dissolved in the solvents and filtered into NMR tube (diameter 5 mm, length 9 inches). Tetramethylsilane (TMS) or the appropriate solvent residual signals are used as internal standards.

UV/VIS Spectroscopy. UV/Vis absorption peaks that are characteristic for metallic nanostructures and conjugated molecules were measured using *Avantes* spectrophotometer ($180 < \lambda < 1100$ nm).

Raman Spectroscopy. SERS -related phenomenon were studied on an alpha300R Witek Confocal Raman microscope, $\lambda = 514.5$ nm.

Gel Permeation Chromatography, GPC. GPC analysis was performed in THF (flow rate is 1ml/min) using Water Breeze GPC system equipped with Waters 1515 pump, Waters 717/plus auto-sampler, Waters 2414 RI detector ad Wyatt Technologies MiniDAWN light-scattering detector. Double columns set (PL-Gel mixed C 5 μm) is used. Polymer concentration of 0.5-1.5 mg/ml is prepared and filtrated through 0.2 μm filter in GPC vials.

3.2.2. Nanostructures Assembly

LB technique. The surface behavior at the air-water interface and LB monolayer depositions onto the silicon substrate were conducted at room temperature using a

rectangular-shaped KSV1000 LB trough. Dilute solution in chloroform (HPLC grade) is deposited drop-wise (5-6 drops, uniformly distributed) onto the Nanopure water surface (Nanopure, > 18MΩxcm) and left to evaporate and spread evenly over a period of 30 minutes at room temperature. A graph of surface pressure (mN/m) versus area per molecule (nm^2) was plotted during monolayer compression using symmetrical barriers. During LB deposition, the surface pressure was held constant as the submerged silicon substrate is slowly lifted up at a velocity of 1-3 mm/min.

Spin Coating. A uniform thin-film assembly was conducted in a semi-clean-room environment on a Headway Research, Inc. spin coater. The typical spin rate was 1,000-3,000 rpm for 10-20 seconds, adjusted depending on the desired film thickness.

3.2.3. Materials characterization

Atomic Force Microscopy, AFM. Surface morphology was studied with Dimension-3000 (Digital Instruments, Inc.) in the "light" tapping mode. [90, 91] The AFM tip radii are between 20 and 35 nm and the spring constants of these cantilevers are in the range 40-60 N/m. Images were obtained within 40 x 40 μm^2 to 1 x 1 μm^2 scan size.

Optical Microscopy. Leica optical microscope with up to 1,000x magnifications were used to obtain microstructural images in dark-field, differential interference contrast, fluorescence, and bright-field modes.

Scanning Electron microscopy. Scanning electron microscopy images were obtained with a LEO 1550 TFE scanning electron microscope equipped with EDX spectrometer.

Transmission Electron Microscopy. Transmission electron microscopy images were obtained with a JEOL 100C transmission electron microscope.

X-Ray Diffraction. X-ray diffraction spectra were obtained using X'Pert PRO MRD X-ray diffractometer to confirm the crystal structures of inorganic nanoparticles

Electrical conductivity. Electrical conductivity was measured by a two-probe method using a HP 4155 parameter analyzer. Membrane piece was deposited on a thick silicon oxide layer (200 nm) of a silicon substrate with photolithographically patterned Au / Ti (30 nm/ 5 nm) electrodes. The electrodes were rectangular with 200 μm channel width and 40 μm gap covered with LbL membrane. Voltage was varied between -1 and 1 V.

3.2.4. Measurement of micromechanical property

Bulging Test. Bulging test was developed following the procedures described in detail in the literature. [92,93,94,95,96] Bulging test was performed using a custom-made interferometer equipped with a CCD camera (Logitech) and He-Ne laser (λ=632.8 nm). Pressure (up to 5,000 Pa) was exerted using 60 mL syringe regulated by automatic pump (Kent Scientific, Inc.) and monitored with automatic pressure gauge, DPM 0.1 (SI Pressure

Instruments). Bulging data analysis was conducted by using the model for elastic deformation of circular membranes according to the routine described earlier. [97]

For a typical bulging measurement, a 2 x 2 mm^2 film was freely suspended over a copper pinhole having a 150 μm hole. The film was first inspected under optical microscope and minimum pressure (2,000 Pa) was exerted to check for symmetrical Newton's ring pattern that indicates membrane homogeneity (Figure 3.1a inset). While monitoring pressure, the slightly pressurized membrane was idled for a few minutes to ensure the absence of any leaks. A Visual Basic program was written (SEMA research laboratory, PI: Prof. Vladimir V. Tsukruk) to simultaneously monitor both the film and copper substrate deflection with increasing pressure. As pressure increased, film deformation is indicated by changes in color from bright to dark at the center of film (Figure 3.1b). A plot of color intensity with respect to pressure can therefore be generated (Figure 3.1a). The number of rings, n, that is accumulated with increasing pressure is directly proportional to the amount of film deflection, d, as such, $d = n.\lambda/2$. Throughout experiment, the copper can deform as much as 40% with respect to membrane. The actual membrane deflection was determined by subtracting the copper deflection from the observed membrane deflection. The result of this experiment yields a curve of Pressure versus deflection. The mechanical properties of the film can be derived from the P and d curve as delineated in Appendix B.

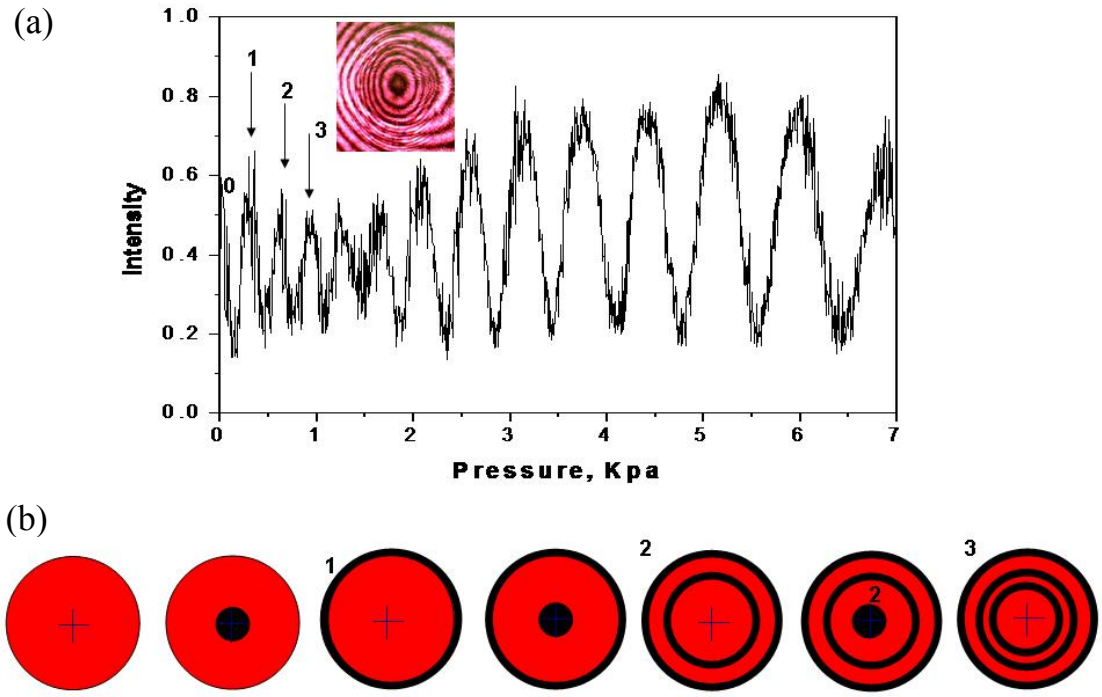

Figure 3.1. (a) Plot of intensity versus Pressure at the center of film that is freely suspended over a circular cavity and subjected to pressure. Inset is an optical image of Newton's ring interference of bulged film. (b) Pictorial illustration of Newton's ring formation with increasing deflection.

Buckling Test. A film residing on an elastic substrate undergoes buckling instability when subjected to a critical compressive stress. This measurement assumes a perfect adhesion between the film and the PDMS substrate, *i.e.*, no delamination during buckling. While taking into account the Young's modulus of the substrate and the film thickness, the characteristic wavelength, λ, of the buckled film can lead to the film's Young's modulus. [98,99, 100] To initiate the buckling pattern, a 2 x 2 mm^2 membrane piece was placed over a 0.6

x 0.6 cm^2 x 0.4 cm PDMS substrate which was slowly compressed with a micron-sized increment. The total compressive distance was generally less than 15 μm. The compression was monitored under optical microscope in differential interference contrast (DIC) mode adjusted for maximum contrast.

For anisotropic buckling test, the Ag-LbL film was transferred on an elastic PDMS substrate (0.6 cm x 0.6 cm x 0.4 cm) and the compressive force was exerted perpendicular and parallel to AgNW orientation at micrometer-size increments. Fourier transformations of these images were done with *ImageJ* to estimate the buckling spacing.

Refer to Appendix B for equations related to bulging and buckling measurements.

3.2.5. Electrical conductivity measurement

Electrical conductivity was measured by a two-probe method using a HP 4155 parameter analyzer. Film was deposited on a thick silicon oxide layer (200 nm) of a silicon substrate with photolithographically patterned Au / Ti (30 nm/ 5 nm) electrodes. The electrodes were rectangular with 200 μm channel width and 40 μm gap. Voltage was varied between -1 and 1 V. Film resistance was determined from the slope of the V-I curve. Its conductivity, $1/\rho$ ($\Omega^{-1}cm^{-1}$ or S/cm), can be calculated according to Equation 3.1, where ρ is resistivity (Ω/cm), R is resistance (Ω), w is film width, t is film thickness, and l is film length.

$$\frac{1}{\rho} = \frac{l}{Rwt} \qquad \text{(Equation 3.1)}$$

CHAPTER 4

DESIGN OF ULTRATHIN SILVER NANOWIRES REINFORCED COMPOSITE FILM WITH TUNABLE MECHANICAL PROPERTIES

4.1. Introduction

Silver nanoparticles can be synthesized in the form of traditional nanospheres, [101] and anisotropically-shaped cubes, [102] rods, [103,104,105,106,107] tubes, [108] prisms, [109] dendrites, [110] plates, [111] disks, [112] and nanowires. [113] These silver nanoparticles can be exploited as nanoscale building blocks with unique properties such as geometrical-dependent optical properties [114,115] or surface enhanced Raman scattering. [116] Nascent studies have already shown fascinating behavior and potential applications unique for 1D nanoparticles. [117,118] However, handling of these nanoparticles and their integration into microfabricated electronic structures is a great challenge. Different ways to accomplish this task include microprinting, using sacrificial nanopores templates, selective surface adsorption, and microfluidic driven alignment. [119]

Particulate reinforced composites are widely utilized in plethora applications. [120] The overall property of composite materials is governed by the nature of the reinforcement (*e.g.* geometry, distribution, interaction among them) and its volume fraction. In coping with the demand for more compact devices, similar approach is actively undertaken at a much reduced scale.[121] Particularly for ultrathin-film preparation, layer-by-layer (LbL) assembly technique [122] is regarded to be the most versatile approach allowing nanoscale thicknesses, controlled thickness, internal organization, and molecular structure.[123] These

films can be made into ultrathin nanocomposites with alternating inorganic nanoparticles and polyelectrolyte layers simply deposited on substrates or as free-standing nanostructures integrated with microfabricated devices.[124,125,126,127,128,129,130] Fabricating freely suspended metal nanoparticle arrays encapsulated into elastic polymer films and integrated with microfabricated MEMS structures is a challenging task which was accomplished only in a few instances. [131] Significant reinforcement of micromechanical properties along with peculiar optical response was reported for these films including stress-dependent Raman response, formation of tunable Raman gratings, record high stability and self-recovery ability. [132,133] Integration of these free-standing structures onto silicon-based array of optical cavities enabled thermal imaging by the direct conversion of IR flux into visible optical response *via* photothermal mechanism.

A key element of these prospective sensing elements is nanoparticulate materials with unique stimuli responsive properties. For instance, the well-tuned noble metal nanoparticles suitable for ultrathin nanocomposite films are widely exploited. [134]

In this study, we tested the feasibility of incorporating metal nanowires into elastic free-standing structures by using LbL assembly. We report the detailed micromechanical study of the resulting flexible 2D silver nanowire (Ag-NW) array including the evaluation of elastic modulus, ultimate strength, and ultimate fracturing behavior (toughness) for a wide range of silver nanowire contents. We demonstrate that a planar array of scarcely and densely packed silver nanowires with random orientation can be robust enough to sustain significant deformations. Furthermore, we will also demonstrate that a significant in-plane

conductivity of LbL nanomembranes is observed when the silver nanowires content exceeds the 2D percolation limit. [135]

4.2. Fabrication of silver nanowires reinforced polymer composite film

The free standing LbL films were fabricated by SA-LbL according to the procedure described elsewhere. [132,136,137,138,139,140,141,97] Briefly, cellulose acetate sacrificial layer (2.5 wt% solution in acetone containing 3 wt% water) was spin-coated on a clean silicon wafer. Alternating positive and negative PAH and PSS were spin coated to form ten bottom PAH/PSS bilayers terminated with PAH, followed by casting of the Ag nanowire solution in methanol (1-2 mg/mL, 100 μL or one drop). The density of AgNW was controlled by casting the 100 μL solution multiple times. In between casts, the coated surface was rinsed once with Nanopure water. This is to remove unattached AgNWs. Upon casting, the gray AgNW solution uniformly wet the whole surface, and dried within 30 seconds. Another ten top PAH/PSS bilayers were assembled after rinsing the final nanowire layer twice with Nanopure water. Two-times rinsing with Nanopure water was done for each deposited polyelectrolyte layer to remove unattached polyelectrolytes.

Films with silver nanowires sandwiched between $(PAH/PSS)_{10}$ films is designated as $(PAH/PSS)_{10}$ Ag $(PAH/PSS)_{10}$ (ϕ), where ϕ refers to the different densities of nanowires within central layer in percent volume fraction. The volume fraction ϕ is calculated as volume occupied by silver nanowire (assume cylindrical cross-section) divided by total volume of membrane (taking into account the membrane asymmetrical geometry discussed later in text). The above procedures were performed in Cleanroom class 100.

Finally, LbL film was cut into approximately 2 x 2 mm^2 squares using stainless steel micro-needle. They were then released by submersion in acetone, which preferably dissolves the cellulose acetate layer. [142] The LbL composite film did not dissolve in acetone. For easy deposition on a 3 mm diameter copper substrate with 150 μm opening or on TEM grid, the floating membranes were transferred into another Petri dish containing Nanopure water. Upon transfer from acetone into water, the films float flatly on the water surface and can be easily placed onto various substrates.

For thickness determination, some membranes were deposited on a silicon substrate. Membrane thickness was measured from AFM cross-sectional analysis across the edge of film (Figure 4.1).

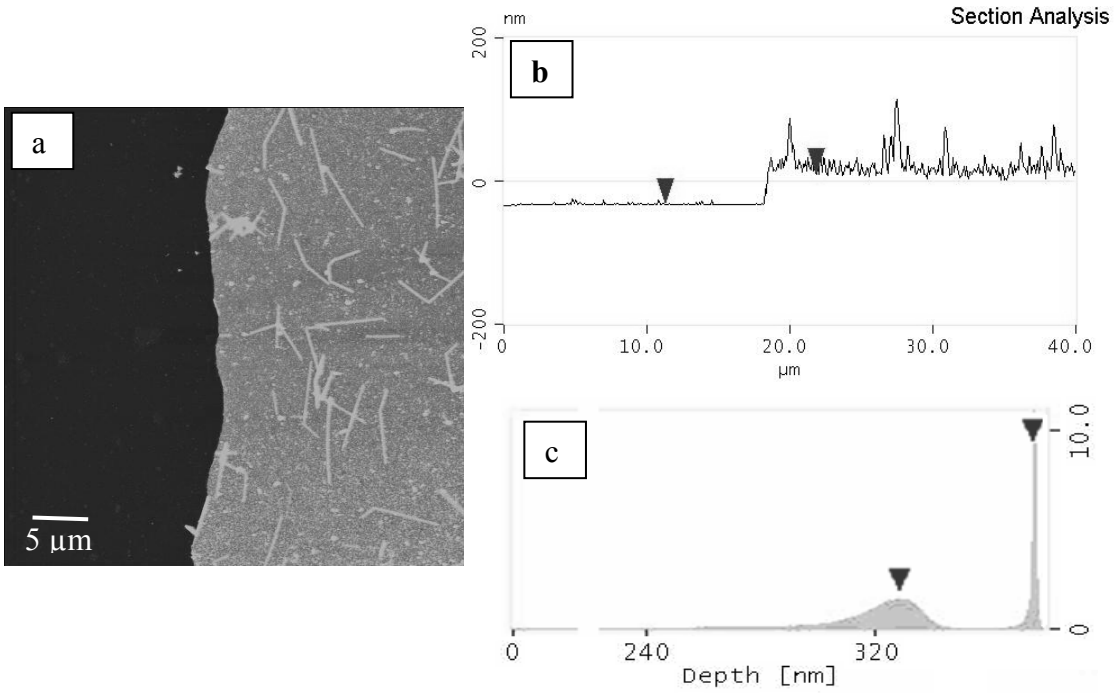

Figure 4.1. (a) AFM image, (b) cross-section, and (c) height histogram of the edge of $(PAH/PSS)_{10}$ Ag $(PAH/PSS)_{10}$ (2.5%) membrane deposited on a bare silicon wafer. Z scale is 500 nm.

4.3. Results and discussions

4.3.1. Analysis of the silver nanowires composite film

The diameter of silver nanowires estimated from AFM cross-sectional analysis was 73 $\pm$ 11 nm with the average length reaching 6.1 $\pm$ 2 µm (Figure 4.2). These values were averaged from over 100 nanowires. These dimensions give an aspect ratio of 84 which is higher than that observed for typical metallic nanorods,[143] and is a common characteristic of nanowire structures thus justifying to call them nanowires. Sharply bent and zig-zag nanostructures were occasionally observed in addition to dominating straight morphology reminiscent that reported by Chen *et al* for gold seeded polyol synthesis of silver nanowire.

[144] High resolution AFM image revealed regular shape with smoothened faceted cross-section expected for polyol synthesized silver nanowires (Figure 3b). [145,146] The content of PVP material on a nanowire surface after purification should be within 3-5 wt % according to the literature. [147] By applying a core-shell cylindrical model, we estimate the thickness of PVP coating to be within 4-6 nm which leaves 61-65 nm for a silver core, a value which was used to calculate a theoretical composite modulus (see below).

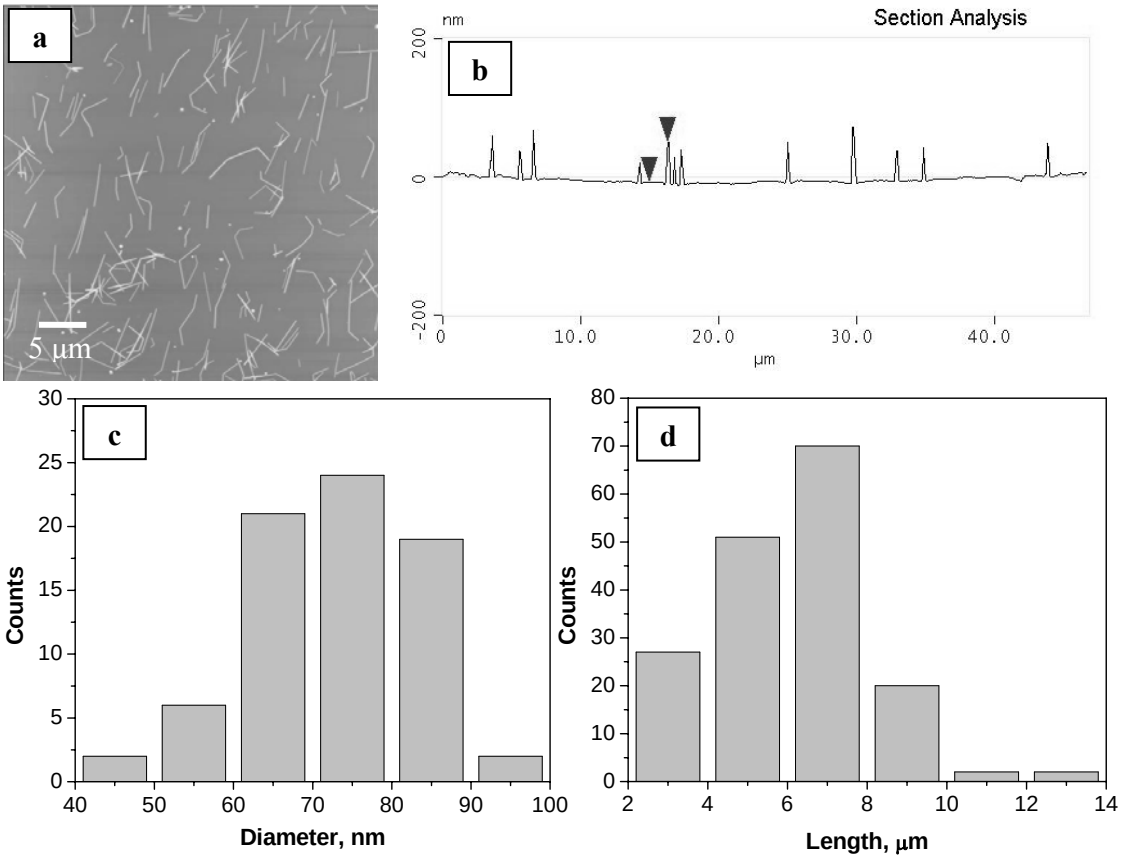

Figure 4.2. (a) AFM topography of silver nanowires deposited on PAH/PSS/PAH film and its corresponding AFM cross-sectional analysis (b). Z scale is 300 nm. (c) Diameter and (d) length distributions of the silver nanowires.

4.3.2. Controlling nanowire surface density

By casting different amounts of solution, silver nanowire arrays with four different surface coverages were prepared on LbL films (Figure 4.3, Table 4.1). The surface coverage was determined by counting the number of nanowires over 40 x 40 μm^2 surface areas (Figure 4.3). The plot of the surface coverage versus number of solution drops used for deposition was used to determine the surface coverage for the highest density using a linear relationship between number of drops and nanowire density. The nanowires formed predominantly random planar array with vast majority of them confined to planar surface and modest aggregation even at the highest surface coverage (Figure 4.3).

Table 4.1. Effective thickness and Young's moduli of $(PAH/PSS)_{10}$ Ag $(PAH/PSS)_{10}$ (ϕ) membranes measured from bulging and buckling methods, and calculated from Halpin-Tsai and rule of mixture equation.

Area coverage (%)	**Volume fraction, ϕ (%)**	**Effective film thickness (nm)**	**Bulging Young's Modulus**	**Buckling Young's Modulus (Gpa)**	**H-T Young's Modulus (GPa)**	**Rule of Mixture Young's Modulus (GPa)**
0	0.0†	55 ± 2	2.2 ± 0.5	1.7 ± 0.5	2.0	2.0
2.1	2.5	46 ± 2	1.6 ± 0.4	2.5 ± 0.5	2.4	4.2
6.3	7.5	49 ± 2	2.2 ± 0.5	3.5 ± 0.4	3.2	7.9
12.6	15	54 ± 2	2.8 ± 0.6	5.0 ± 0.4	4.5	13.7
18.9	22.4	60 ± 2	4.6 ± 0.5	5.7 ± 0.5	5.7	19.5

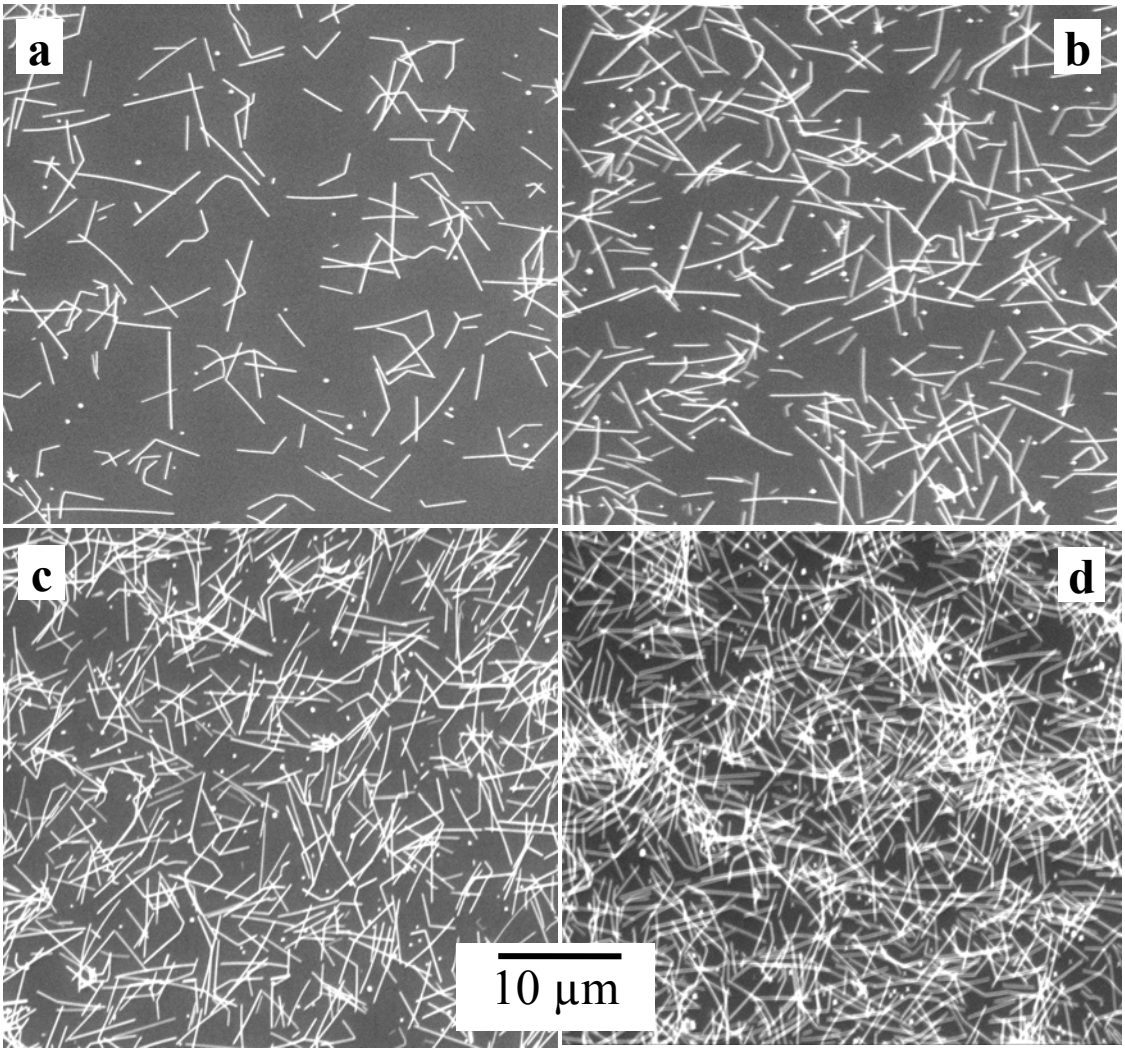

Figure 4.3. SEM images of silver nanowires with different surface coverages on PAH/PSS/PAH film which correspond to different volume fractions, ϕ: (a) 2.5%, (b) 7.5%, (c) 15%, and (d) 22.5%.

Uniform nanowires distribution without any significant aggregation was preserved after their encapsulation within LbL films (about 26 nm thick on each side) and upon transfer onto a copper substrate with a microfabricated hole (Figure 4.4a). High resolution optical imaging showed random in-plane distribution of silver nanowires which is uniform across the edge of the hole as well (Figure 4.4b). AFM images obtained *directly* on free-

suspended film showed predominantly planar arrangement of silver nanowires coated with polymer multilayer show modest protrusions created by the nanowires having diameter larger than the effective thickness of the polymer film (see below) (Figure 4.4d).

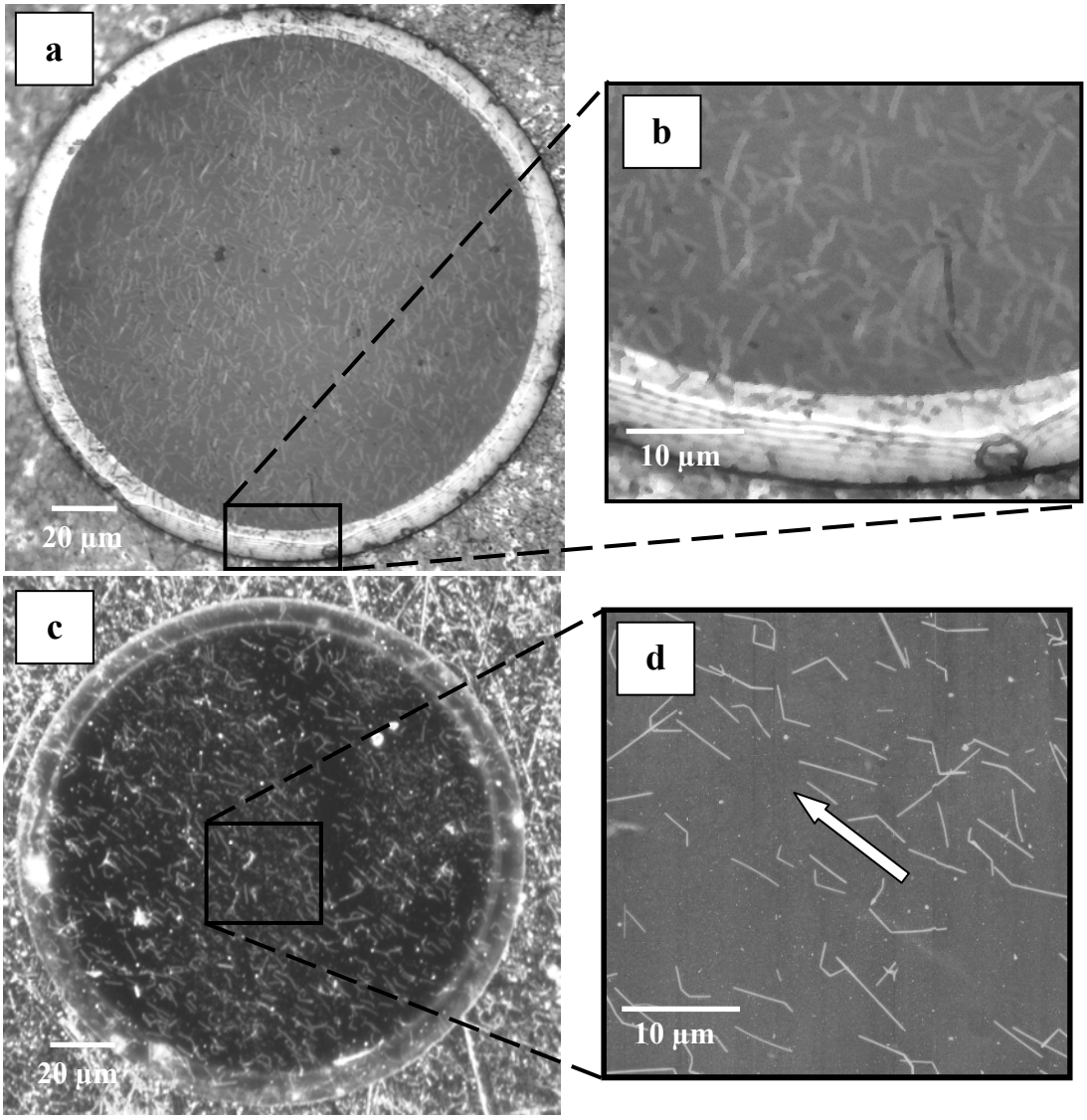

Figure 4.4. (a-c) Representative optical microscopy images of $(PAH/PSS)_{10}Ag(PAH/PSS)_{10}$ films suspended over 150 µm diameter opening demonstrating nanowire distribution within the LbL films with ϕ = 2.5%: (a) randomly oriented nanowires with higher

magnification of the film edge (b); (c, d) LbL film with preferentially oriented nanowires indicated by an arrow; (d) AFM image of corresponding freely suspended membrane (c), Z-scale is 300 nm. (a) and (b) were captured in bright-field mode, while (c) was captured in dark field mode.

4.3.3. Shape of freely suspended membranes

To elucidate the morphology of the free-suspended LbL film with encapsulated silver nanowires, we conducted *direct* AFM scanning with extremely light tapping mode conducted *on both sides* of the LbL film within the same surface (top and bottom sides) area. The result is corresponding "mirror-like" AFM images displaying identically shaped nanowires (see marks in Figure 4.5a,b). Cross-sectional analysis of these images revealed that the free-suspended LbL film has a "wavy" contour with elevated features extending beyond the planar nanowire-free surfaces to different degrees (see cross-sections across identical spots in Figure 4.5). High-resolution AFM confirmed that the nanowires are completely covered with PAH/PSS polymer on both sides. The RMS microroughness of 20 x 20 μm^2 surface areas on the top-side increases from 15.5 $\pm$ 2 nm to 70 $\pm$ 6 nm for ϕ increasing from 2.5 to 22.5 %, while the microroughness of the bottom side increased only slightly from 11.9 nm $\pm$ 2 nm to 19.1 $\pm$ 2 nm.

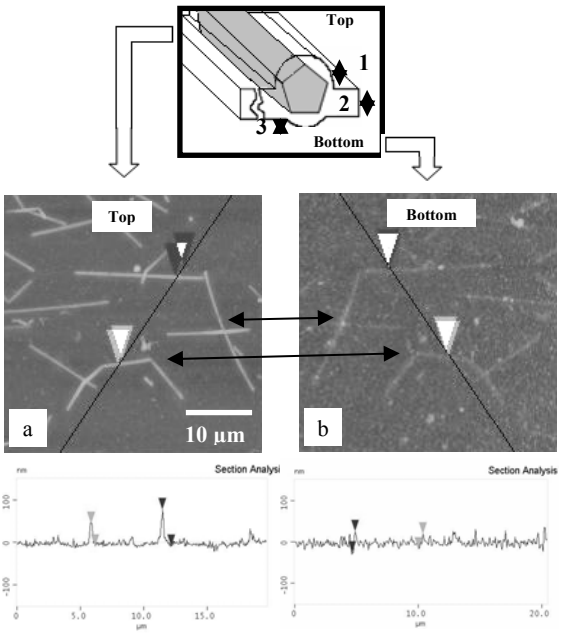

Figure 4.5. AFM topography of freely suspended $(PAH/PSS)_{10}Ag(PAH/PSS)_{10}$ (2.5%) membrane scanned on top (a) and bottom (b) surfaces for identical selected surface area along with their corresponding cross-sections. Pay attention to mirror symmetry of the images with identical surface features. Top: cartoon representation of an encapsulated nanowire.

This morphology can be understood considering that the overall diameter of silver nanowires is 73 nm and the thickness of each $(PAH/PSS)_{10}$ is only about 26 nm as determined from independent AFM scans. The different protrusion heights on top and bottom sides for the same encapsulated nanowires from AFM cross-sectional analysis (compare Figures 4.5a and b) suggest an asymmetrical morphology of silver nanowires encapsulated within LbL membrane. A key element of this model is the silver nanowires encapsulated within thinner polymer film, where the polymer film conformally covering the nanowires (Figure 4.5). We suggest that the asymmetrical cross section is caused by different fabrication conditions for the bottom LbL film assembled on the CA planar substrate and top LbL film deposited directly onto silver nanowires.

The protruding portions of silver nanowires are characterized by different heights **1** and **3** with the film thickness **2** (Figure 4.5). These values were determined from both cross-sectional and bearing analysis of AFM images of both sides of the LbL films as demonstrated in Figure 4.1. Surface histograms were also used to calculate the effective thickness of the LbL film required for the evaluation of the micromechanical properties of the free-suspended films (see below). These dimensions were estimated to be fairly consistent for all LbL films studied here with 45 $\pm$ 10 nm for **1**, 44 $\pm$ 3 nm for **2**, and 15 $\pm$ 2 nm for **3**. These values suggest that the top LbL film covered nanowires conformally and nanowires are partially embedded into the bottom supporting LbL film in the course of multi-step assembly. It is worth to note that the film thickness, **2**, was only 44 nm which is less than that for the nanowires-free LbL film fabricated independently (62 nm) and indicate that the encapsulation of silver nanowires does in fact affect overall microstructure in interparticulate areas.

4.3.4. Micromechanical properties of LbL films with silver nanowires

The bulging test generates a set of experimental data for the deformed free-suspended films, deflection d (μm) with respect to variable pressure, P (Pa) (Figure 4.6). These data were analyzed using the theoretical model for circular elastic plate clamped to stiff edges as has been discussed in detail in literatures, also described in Appendix B: [148,149]

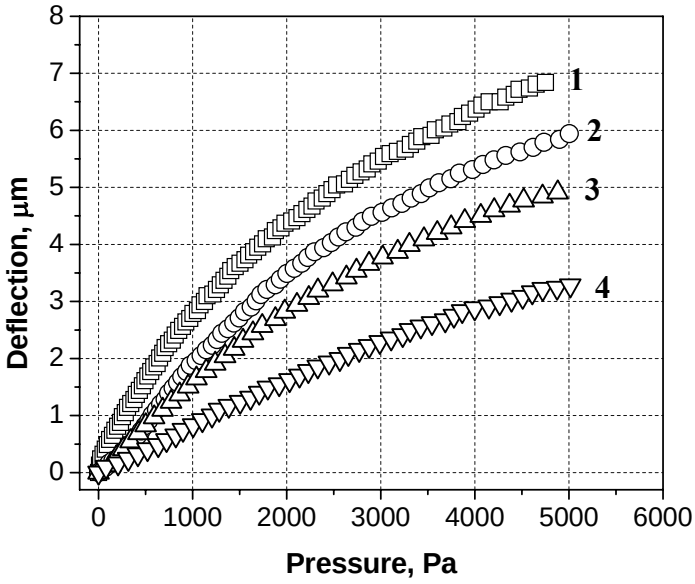

Figure 4.6. Deflection versus pressure measurements for $(PAH/PSS)_{10}$ Ag $(PAH/PSS)_{10}$ (ϕ) membrane: **1.** ϕ = 2.5%, **2.** ϕ = 7.5%, **3.** ϕ = 15.0%, and **4.** ϕ = 22.5%.

The fitting of the experimental data for bulged membranes with different volume content of silver nanowires allowed for the evaluation of their elastic moduli in tensile regime (Figure 4.6). The elastic moduli were determined to be from 2 GPa up to 4.6 GPa for the film with the highest content of nanowires (Table 4.1 and Figure 4.7). The asymmetrical microstructure of nanowires-containing LbL films had no influence on the film deflection in different directions under positive and negative pressure differentials as demonstrated in Figure 4.8 indicating that major elastic deformation takes place in-between encapsulated nanowires.

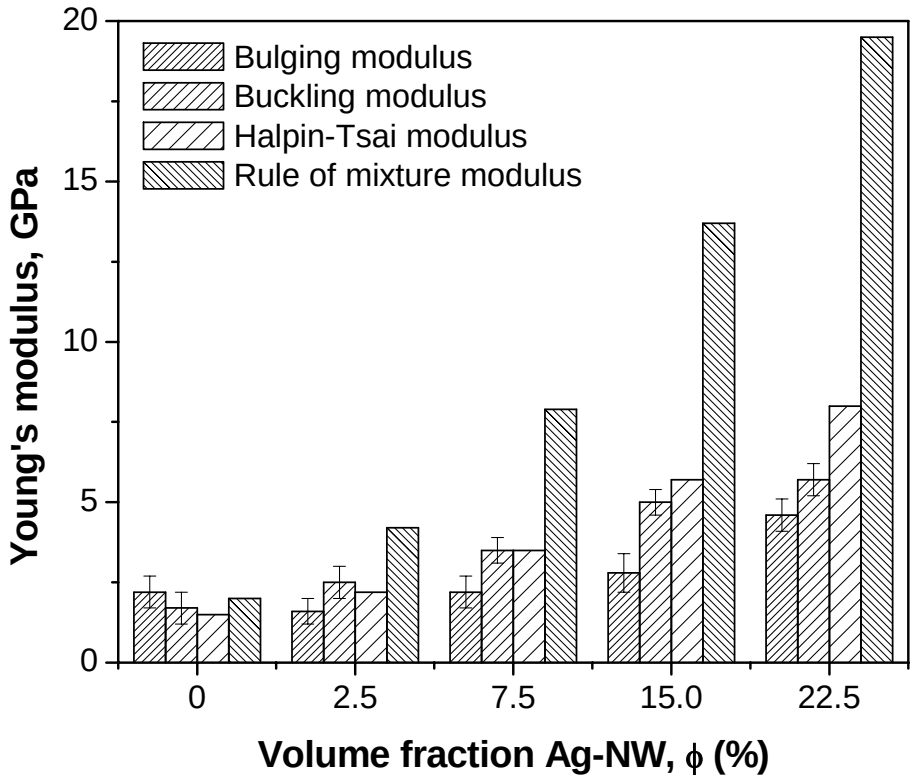

Figure 4.7. The variation of Young's modulus versus the volume fraction of silver nanowires, ϕ, as evaluated from bulging and buckling techniques in comparison with the theoretical composite modulus.

Independent values of the elastic modulus in compression mode were obtained with buckling instability test. The overall buckling pattern was observed to be fairly uniform for different LbL films and the wrinkles were extended over several hundred microns (Figure 4.9). Smoother surface areas were observed in the vicinity of nanowires indicating higher local stiffness which, however, did not affect the overall spacing. The Young's modulus of the LbL films, E_{film}, that is subjected to buckling instability was calculated according to the equation described in the literature for LbL films (Appendix B). The characteristic wrinkle wavelength, λ, ranged from 2.11 μm and 3.60 μm for the different films (ϕ = 2.5%-

22.5%) was determined from the 2D Fourier transform of the optical images. [150] The elastic modulus of PDMS substrate was 1.8 MPa as measured from independent tensile stress experiments. The Poisson's ratio for LbL membrane and PDMS substrate were taken as 0.3 and 0.5, respectively.

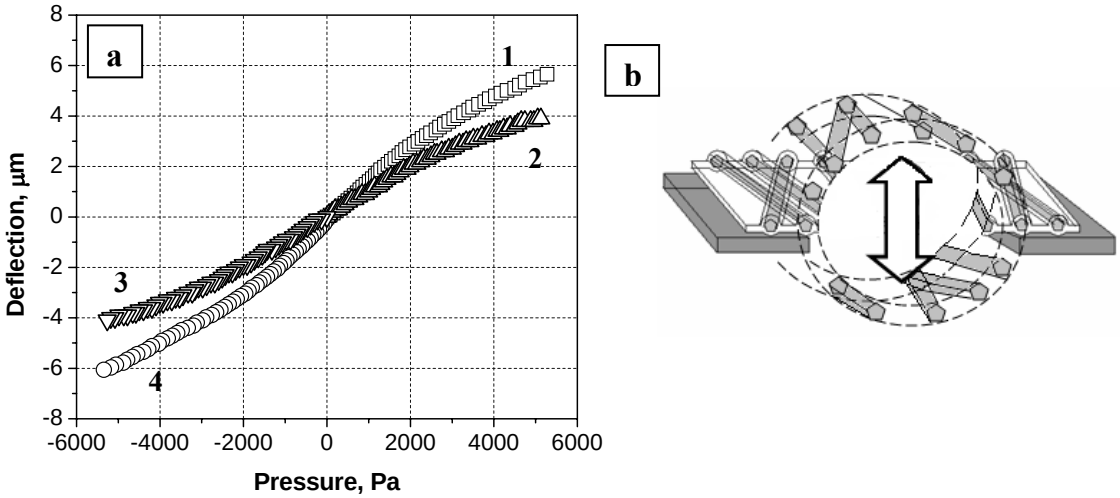

Figure 4.8. (a) Deflection versus pressure plots for $(PAH/PSS)_{10}$ Ag $(PAH/PSS)_{10}$ (ϕ) membranes: (1, 4) ϕ = 2.5%, and (2, 3) ϕ = 22.5%. **1** and **2** are bulged-up (positive pressure), and **3** and **4** are bulged-down (negative pressure). (b) Cartoon representation of concave and convex shapes of bulged membrane.

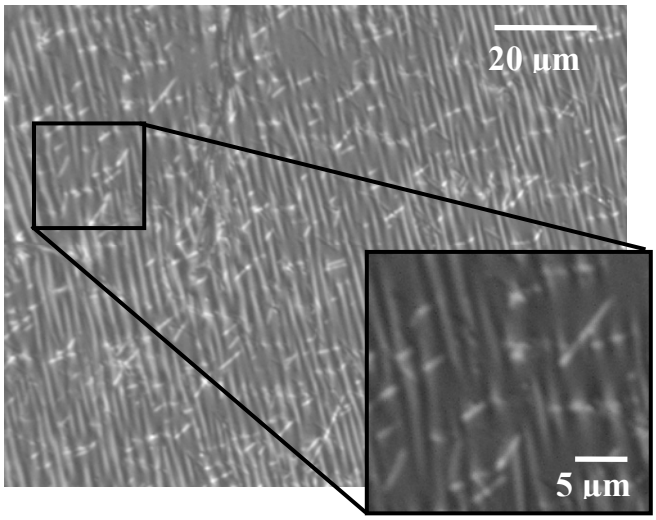

Figure 4.9. Optical microscopy images of buckling instability for $(PAH/PSS)_{10}$ Ag $(PAH/PSS)_{10}$ (2.5%) membrane at different magnifications (differential interference contrast (DIC) mode).

The Young's moduli calculated in this manner yield a value of 1.7 up to 5.7 GPa for increasing content of silver nanowires (Table 4.1). The values obtained for buckled LbL films were fairly close to those obtained from bulging experiment (Figure 4.7). All differences observed for LbL films are within or close to the experimental deviation with a general trend for the elastic modulus from buckling experiments being on a high side. Lower elastic modulus for freely suspended LbL films can be related to higher residual stresses and greater role of defects ("weak points") in tensile deformation of freely suspended films. Therefore, tensile (bulging experiments) and compressive (buckling) properties of LbL films are similar as expected for small elastic deformations of composite materials with random orientation of one-dimensional fillers.

4.3.5. Micromechanical behavior of LbL membrane with encapsulated silver nanowires

To analyze the micromechanical behavior of nanowire-containing LbL films and corresponding filler reinforcement phenomenon we employed Halpin-Tsai and rule-of-mixture model for the evaluation of the composite modulus with randomly oriented fibers, E_{random}. (Appendix C). [151] The Young's modulus of the unfilled LbL film was taken to be E_m= 1.5 GPa for-PAH/PSS film [152] and the Young's modulus of silver nanowire filler was taken to be E_f= 88.0 GPa. [153]

The calculated values of the composite moduli for LbL membranes with different content of nanowires in comparison with experimental values are summarized in Table 4.1 and in Figure 4.7. Clearly, the rule-of-mixture prediction does not accurately model the Young's modulus of nanowires-containing LbL composite films. The predicted Young's moduli calculated according to the Halpin-Tsai model, on the other hand, closely match with those measured from bulging and buckling techniques, which thus suggest a strong filler-to-matrix bonding. The high aspect ratio silver nanowires confined within 2D planar state apparently resulted in the formation of dense network even for relatively low nanowire content significantly enhancing the elastic modulus of the nanocomposite films without considerably affecting their compliance. On the other hand, above certain critical concentration of nanowires multilayer network of nanowire should be predominantly formed which was indeed observed for the highest nanowires content tested here. Excessive nanowire junctions and protrusions from the planar film should compromise the integrity of the 2D film, hence the overall micromechanical properties. We suggest that the ultimate combination of these two phenomena falls within a narrow window skewed towards lower concentration of nanowires.

For LbL films that exhibit low ultimate deformation, a full pressure versus deflection curve can be converted into stress (σ) versus strain (ε) curve which can be used to estimate the film toughness from the area under the stress-strain curve. For circular geometry, the conversion can be done by using relationships [154,155] $\sigma = Pa^2/4hd$ and $\varepsilon = 2d^2/3a^2$, where a is radius of opening (75 μm), d is vertical deflection, and h is film thickness (see one example in Figure 4.10). For the most part, the stress-strain curve is linear. Deviation from the linear behavior is observed as the membrane deflection approaches a failure (Figure 4.10). This deviation can be attributed to the start of plastic deformation or material's yield point. The linear portion of the curve can be expressed as $\sigma = \sigma_0 + [E/(1-\nu^2)]\varepsilon$ and thus used to calculate the elastic modulus (Figure 4.11). The residual stress (σ_o), Young's modulus, the ultimate strain (ε_{ult}), the ultimate stress (σ_{ult}), and the static fracture toughness (U_t) can all be estimated from the full stress-strain plots (Table 4.2).

Table 4.2. Residual stress (σ_o), ultimate stress (σ_{Ult}), ultimate strain (ε_{Ult}), and toughness (U_t) of (PAH/PSS) $_{10}$ Ag (PAH/PSS) $_{10}$ films.

Nanowire vol. fraction, ϕ (%)	**Residual Stress, σ_o (Mpa)**	**Ultimate Stress, σ_{Ult} (Mpa)**	**Ultimate Strain, ε_{Ult} (%)**	**Toughness, U_t (kJ/m^3)**
0	13.5 ± 2.5	49 ± 12	1.5 ± 0.2	440 ± 60
2.5	9.9 ± 5.4	64 ± 17	1.5 ± 0.3	590 ± 70
7.5	16.1 ± 2.9	77 ± 12	1.8 ± 0.3	860 ± 270
15	11.7 ± 2.9	64 ± 3	1.4 ± 0.1	540 ± 40
22.4	15.9 ± 6.0	73 ± 12	1.1 ± 0.1	510 ± 50

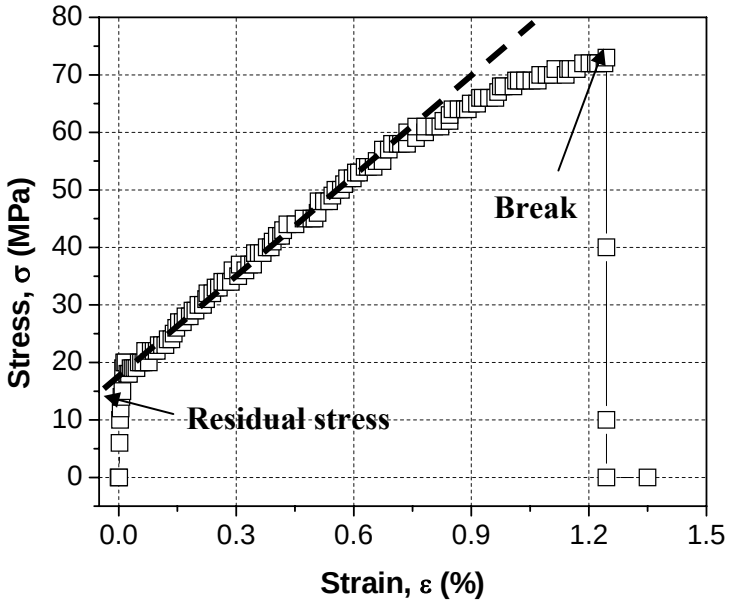

Figure 4.10. A stress (σ) versus strain (ε) plot for $(PAH/PSS)_{10}$ Ag $(PAH/PSS)_{10}$ (2.5%) membrane. Initial sharp increase results from the residual stress and final sharp drop is caused by film fracture.

The ultimate strain decreased slightly (from 1.5% to 1.1%) with an increasing volume fraction of nanowires reflecting higher stiffness due to the presence of silver nanowires filler (Figure 4.11). The ultimate stress varies significantly from specimen to specimen but stays within 70 $\pm$ 7 MPa for all compositions studied here. These values are much higher than purely polymeric LbL films (49 MPa) (Figure 4.11 and Table 4.2). On the other hand it is comparable to those reported for other reinforced LbL films containing carbon nanotubes and gold nanoparticles. [126, 129,97] Finally, the toughness of the LbL films (total energy required to fracture the film) varies within 400-1000 kJ/m^3 with a trend towards lower values for stiffer LbL films and for purely polymeric LbL films. The lowest value of 440 kJ/m^3 for purely polymeric LbL is close to that of common glassy polymers [156] and can be understood considering that both polyelectrolytes for our LbL films are in glassy

state at room temperature. The maximum toughness of about 1000 kJ/m^3 was reached at the intermediate composition (7.5%) due to a combination of higher strength and the ultimate strain (Figure 4.11). This value is on par with tough carbon nanotubes-containing LbL membrane estimated from area under stress-strain curve. On the other hand, due to the limited compliance it is still below the record values reachable for partially-crystalline tough plastics where high strength is combined with high elasticity and plasticity. [157]

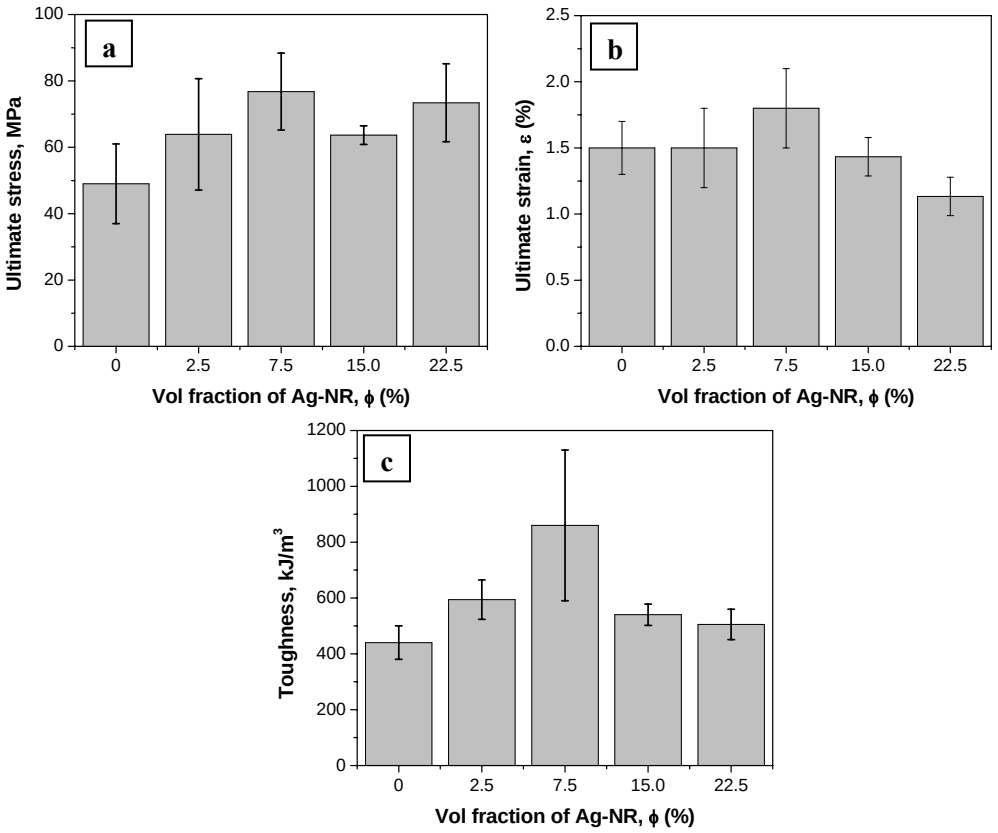

Figure 4.11. The variation of the ultimate stress (a), the ultimate strain (b), and the fracture toughness (c) versus nanowire volume fraction for $(PAH/PSS)_{10}$ Ag $(PAH/PSS)_{10}$ LbL membrane.

4.3.6. Conductivity of silver nanowires reinforced film

It is known that thin polymer films with encapsulated conductive nanoparticles should show electrical conductivity if the nanoparticle content exceeds the percolation threshold. [158] In fact, LbL films with low nanowire content were insulating but the 22.5% volume fraction of silver nanowires induced overall conductivity (Figure 4.12). This concludes that the percolation threshold of AgNW LbL membrane is between 15 - 22.5%. The conductivity value calculated from the linear voltage-current curve for the given membrane thickness (60 $\pm$ 3 nm) according to [159] was 110 $\pm$ 20 S/cm for LbL nanomembranes deposited on electrodes with bottom-down and 660 $\pm$ 35 S/cm for films with bottom-up orientation. These values place silver nanorod LbL nanomembranes on par with highly doped conducting polymers and just below metals. [160] The six-fold difference in in-plane conductivity for bottom-down and bottom-up orientations of LbL nanomembranes is caused by their asymmetric cross-sectional structures discussed above (Figure 4.5). This suggests that the LbL membrane is thicker at the bottom, since the conductivity is inversely proportional to the thickness of an insulating layer.

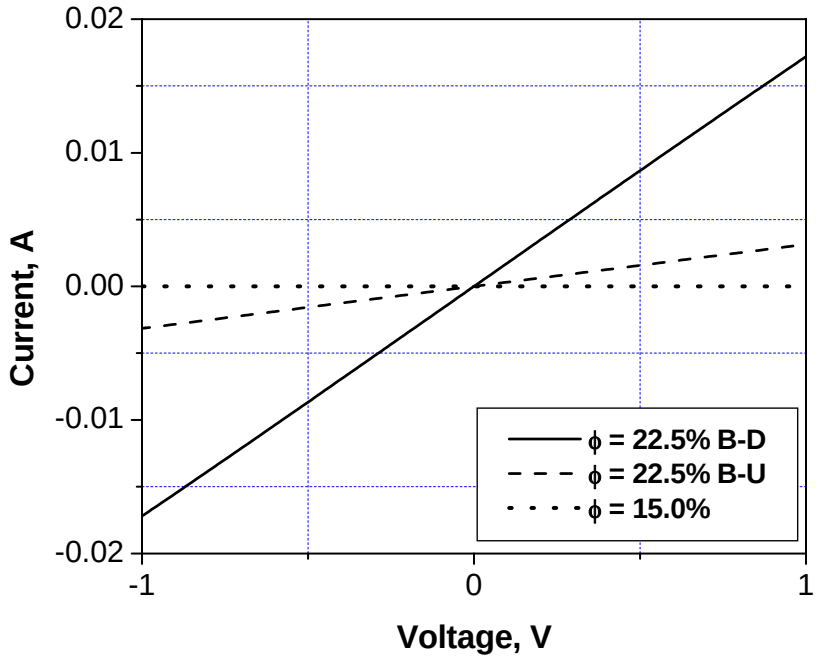

Figure 4.12. A plot of current versus voltage, for the nanomembranes deposited between gold electrodes for silver nanorod volume fractions, ϕ = 15.0 % and ϕ = 22.5% (different orientations of nanomembranes). B-D and B-U are bottom-down and bottom-up orientations, correspondingly.

Surprising relatively high percolation limit within 15 - 22.5% seems to be much higher than that expected for composites containing conductive rod-like particles. In fact, for bulk polymer composites filled with conductive fibers, the percolation threshold usually lies in the range 5 - 15% for short fibers decreasing to 0.2 - 2% for very long fibers. [161] This discrepancy, however, can be understood considering the confinement of nanorods into 2D planar space and the peculiar microstructure of nanorod-containing nanomembranes as follows. First, 2D confinement is known to result in a significant increase in the percolation limit caused by "elimination" of the third dimension for a possible conducting path. Indeed, in a 3D setting, the thickness of the polymeric

membrane should be greater than the average nanorod length to allow 360º spatial rotations thus effectively reducing the filler volume fraction (Figure 4.13). A model derived by Balberg *et al* provides means for the estimation of percolation thresholds for anisotropic particles confined within 2D and 3D space (refer to Appendix C for details):

$$\phi_{c,2D} = 1 - Exp\left(-\frac{< A_{ex} >}{< A_e >} \times A\right) \qquad \text{for 2D}$$

$$\phi_{c,3D} = 1 - Exp\left(-\frac{< V_{ex} >}{< V_e >} \times V\right) \qquad \text{for 3D}$$

, where $<A_{ex}>$ ($<V_{ex}>$), $<A_e>$ ($<V_e>$), and A (V) are total excluded area (volume), local excluded area (volume), and area (volume) of particles. The above equations take into account rod-to-rod maximum disorientation angle and the dimensions of object. For high aspect-ratio rod-like objects in 2D and 3D, $<A_{ex}> = 3.57$ and $<V_{ex}> = 1.41$, respectively.[162]

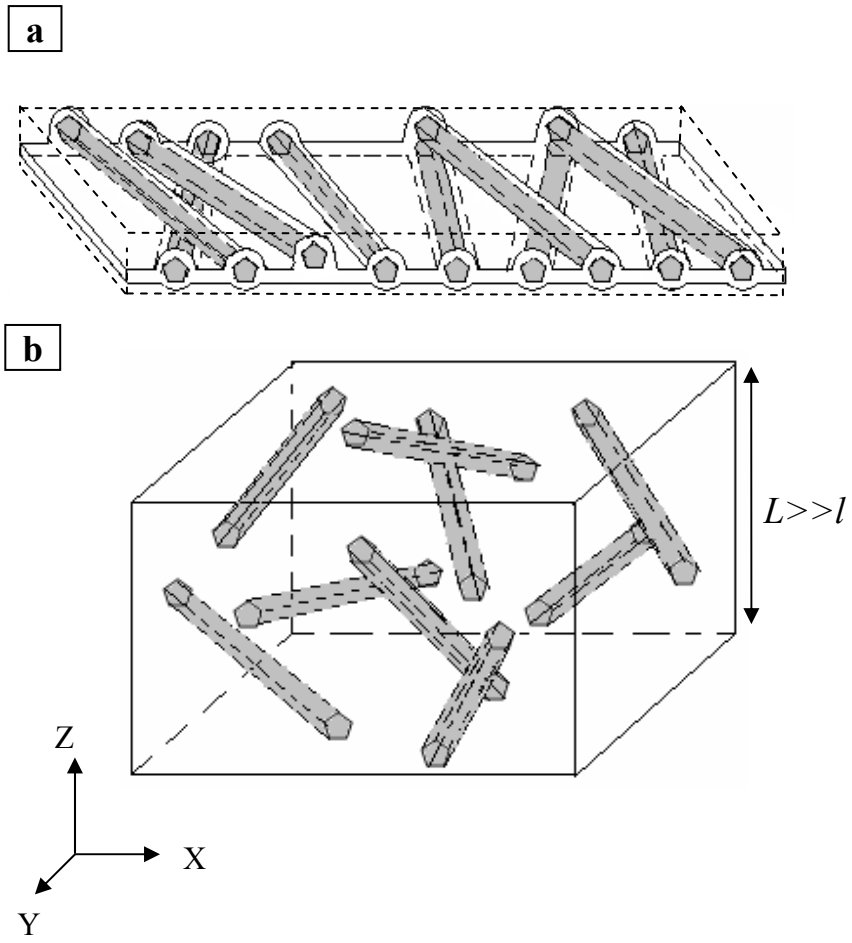

Figure 4.13. (a) 2D arrangement of silver nanowires encapsulated into LbL membrane (thickness L much smaller the nanowire length l). (b) Randomly oriented nanorods in 3D space (thickness L much larger the nanorod length l).

The corresponding calculation for nanowires with dimensions measured for nanowires in our experiments yields $\phi_{c,2D}$ = 8.6 % which is much higher than the corresponding threshold value for 3D setting, $\phi_{c,3D}$ = 0.81 %. On the other hand, for high concentration of silver nanowires protruding from the planar LbL nanomembranes their 2D projection should be considered rather than overall volume content (Figure 4.13). The 2D nanowires content should be estimated by considering a perfectly 2D projection

of nanowires having rectangular cross-section eliminating the effect of silver nanowire diameter (Figure 4.143). This rescaling yields 8.0 % < $\phi_c \leq$ 12.0 % for the experimental percolation threshold boundaries measured here for a single layer of nanowires complies with the theoretical value of 8.6% predicted for a 2D array of our silver nanowires.

In summary, one-dimensional silver nanowires (Diam = 80 + 5 nm, Length = 6 + 2 μm) were sandwiched into layer-by-layer film to yield a series of robust freestanding ultrathin-film (< 150 nm thick). The sandwich architecture allows facile control over volume fraction of silver nanowires (2.5-22.5%). The measured Young's moduli were in agreement with the Halpin-Tsai model for fiber-reinforced composites, and it is tunable with volume fraction of silver nanowires. It ranges from 2 to 6 GPa for pristine up to the highest fraction of silver nanowires (22.5%). Furthermore, the film was found to be conductive (110 – 660 S/cm) within the range of volume fraction in par with theoretical percolation threshold for two-dimensional film. We therefore suggest that these robust, elastic free-standing nanomembranes containing 2D arrays of silver nanowires could serve as prospective sensing elements for acoustic, pressure, and photothermal sensors.

CHAPTER 5

DESIGN OF ANISOTROPIC SILVER NANOWIRES REINFORCED POLYMER COMPOSITE FILM

5.1. Introduction

Uniformly oriented assembly of one-dimensional (1D) nanostructures can lead to novel anisotropic physical properties. For instance, oriented arrays of silver nanowires exhibit polarization-dependent UV-Vis extinction spectra. Similarly for 1D gold nanorods, its small size and its polarization-dependent property make them ideal for plasmon-based optical sensing material. [163,164] Recently, plasmon propagation along the silver and gold nanowires was reported, thus making them good candidates for photonic or guide fibers applications as well. [165,166,167,168] Furthermore, it has been demonstrated that unidirectional carbon nanotube composites can exhibit significant electrical and mechanical anisotropy. [169,170] In another example, Jin *et al* demonstrated silicon nanowires utilization for the fabrication of a field-effect transistor. [171,172] For applications where the directional mechanical load matters, anisotropic reinforced nanocomposites can be tailored to assure a greater strength-to-weight ratio. However, a uniform alignment of nanorods or nanowires is a challenging task and is rarely achieved by using traditional processing approaches. [173]

Thus, there are currently limited accounts on incorporating 1D nanoparticles (especially in a highly oriented state) into ultrathin polymeric films which can be free standing. [174] The ability to freely suspend 1D nanoparticles bears potential in thermal,

acoustic, and chemical sensing applications that demand miniaturizations and enhanced capabilities. [175,176,177,178] Despite numerous techniques put forth to assemble 1D nanoparticles within ultrathin composite films in an anisotropic manner, the uniform orientation combined with a high density of packing is rarely achieved. [179,180,181] In one of successful examples, Langmuir-Blodgett (LB) technique was demonstrated as a powerful tool which enables controlled density and inter-particle distance but this approach cannot be easily used for the fabrication of stable nanoscale polymeric films. [182]

Here, we focus on fabricating uniformly oriented silver nanowires (AgNWs) encapsulated into a flexible and ultrathin polymeric film which is robust enough to exist in the free-standing state without the need for a supporting solid substrate. In doing so, we combined Langmuir-Blodgett and spin-assisted layer-by-layer assembly techniques. Unidirectionally aligned silver nanowires were obtained using the Langmuir-Blodgett technique and the resulting uniform arrays were encapsulated into polyelectrolyte layer-by-layer (LbL) films. Their highly anisotropic mechanical properties were revealed with a buckling test. An interesting phenomenon of polymer matrix-induced longitudinal buckling of silver nanowires observed here was utilized for a fast and straightforward measurement the elastic modulus of these nanowires.

5.2. Sample preparations

DL-6,8-thioctyl ester PEO (5,000 Daltons) was synthesized as follows: the hydroxyl terminated PEO (5g, 1 equiv) solution in 55 mL benzene was first refluxed in a dean-stark flask to remove water. After reflux, there was approximately 25-30 mL

benzene left in a flask. The solution was cooled in an ice bath before 4-dimethylaminopyridine, 4-DMAP (30.5 mg, 0.25 equiv), and DL-6,8-thioctic acid (268 mg, 1.3 equiv) were added under stirring. Finally N, N′-dicyclohexylcarbodiimide, DCC, (268 mg, 1.3 equiv) dissolved in a minimum amount of dry benzene was added. The solution was allowed to stir for 24 hours. The product of hydration, dicyclohexylurea (DCU) white precipitate, was first removed by centrifugation at 7,000 rpm. Next, DL-6,8-thioctyl ester PEO was isolated by the precipitation in diethyl ether (yield about 70%). The chemical structure of the dry powder was confirmed using proton nuclear magnetic resonance technique, ^{1}H-NMR (δ, ppm, $CDCl_3$). Chemical structure shown in Figure 1b was confirmed by NMR as follows: 1.4-1.55 (m, 2H), 1.55-1.80 (m, 4H), 1.85-2.0 (m, 1H), 2.35 (t, 2H), 2.40-2.55 (m, 1H), 3.05-3.25 (m, 2H), 3.65 (s, 310H), 3.88 (t, 2H), 4.23 (s, 2H).

For LB deposition, a portion of the silver nanowire (AgNW) solution was treated with DL-6,8-thioctyl ester polyethylene oxide (PEO) by stirring the mixture in methanol (4% water) for one week to yield Ag-PEO. In 60 mL methanol, 1.3 g DL-6,8-thioctyl ester PEO was used for 67 mg AgNWs (estimated mass). From here onwards, the notation Ag-PEO will be used throughout the manuscript to denote DL-6,8-thioctyl ester-PEO treated AgNWs. Ag-PEO material was isolated by multiple filtrations through a nylon filter (pore size 5 μm), and re-dispersed in an excess volume of metanol. Finally, Ag-PEO material was dispersed in chloroform (HPLC grade) to give a concentration of 3 mg/mL. The gray-silhouette Ag-PEO solution precipitates over-time, thus a brief sonication treatment was necessary prior to each LB deposition.

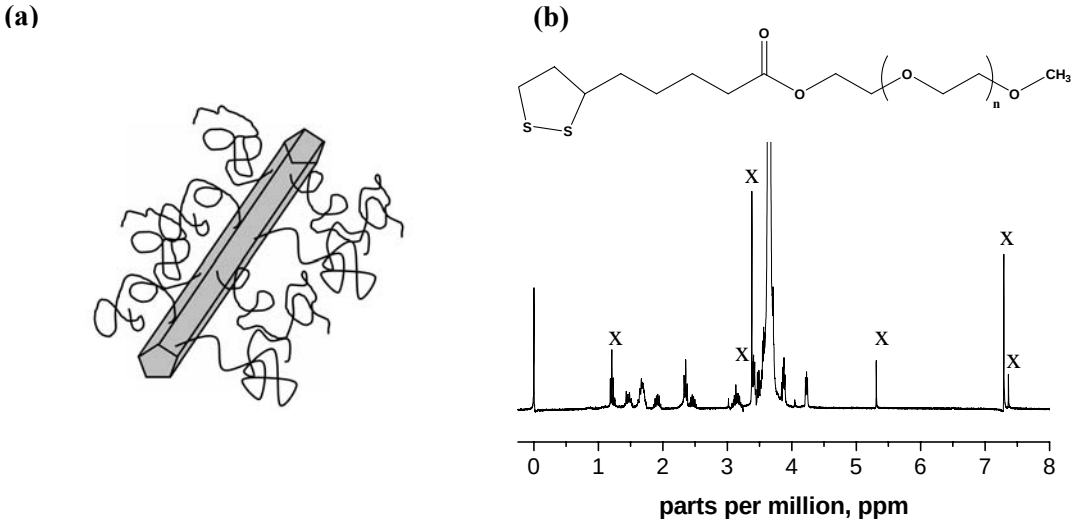

Figure 5.1. (a) Purified polyol synthesized silver nanowire with PVP on surface. (b) ^{1}H-NMR spectrum of DL-6,8-thioctyl ester PEO. "x" designate traces of solvent (benzene, diethyl ether, chloroform, dichloromethane, and methanol).

5.3. Results and discussions

5.3.1. Ag-PVP-PEO nanowires within Langmuir and LB monolayers

Ag-PEO were placed at the air-water interface and oriented by directional compression. Chemical modification of silver nanowires with water soluble PEO chains was critical for inducing the amphiphilic behavior. These modified nanowires display a stable Langmuir isotherms under compression up to about 50 mN/m surface pressure (Figure 5.2). A reversible behavior was observed within the liquid state at the low surface pressure P < 5mN/m. [183,184] The overall isotherm shape suggests the stable amphiphilic behavior after modification with the PEO chains with an initial gradual increase in the surface pressure to be attributed to the submerging of the PEO chains into

the water subphase. [185,186] The steep increase in the surface pressure was detected for the surface areas below 10 μm^2 per nanowire (Figure 5.2).

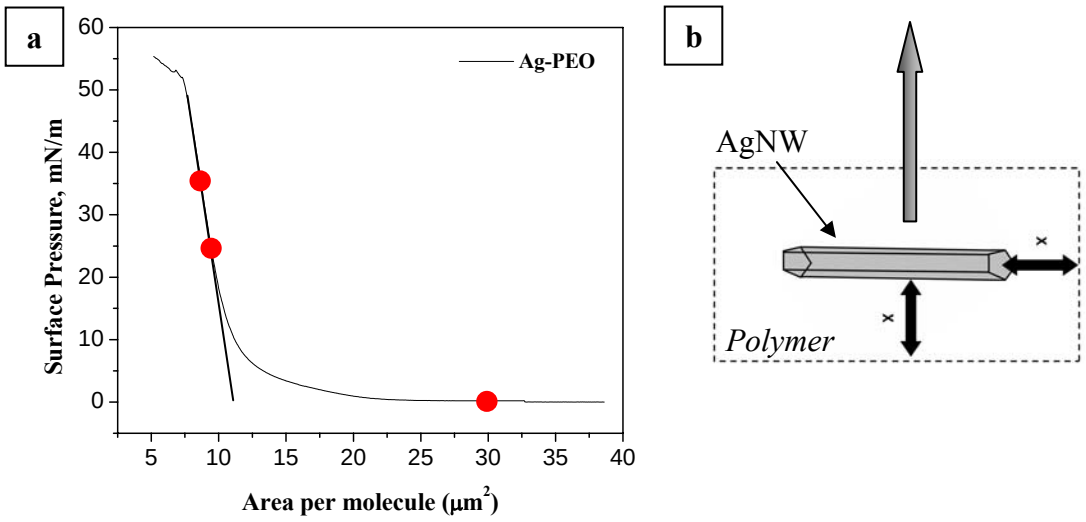

Figure 5.2. (a) Langmuir isotherm of Ag-PEO nanowires, dots indicate the surface pressures at which depositions were performed. (b) Schematic representation of the surface area occupied by a single nanowire, Ao. Vertical arrow represents the dipping direction relative to water surface.

From Langmuir isotherms, the limiting area, A_o, 11 μm^2, was determined at the steep rise in the surface pressure. On the other hand, at P = 25 mN/m, the surface coverage with silver nanowires was 3.0 $\pm$ 0.6 % as determined by counting a number of nanowires in the selected surface areas using their average length and diameter. The surface area occupied by a single nanowire divided by A_o yields the surface coverage 4.0 %, which is consistent with the independent image analysis conducted after transfer to the solid support. Some difference is the result of Ag-PEO monolayer not fully transferred

onto the substrate due to "cracking" and other defects (see below). Assuming a uniform spacing between silver nanowires, the surface area per a single nanowire is estimated to be 1,430 nm^2 which is much larger than that estimated for a PEO-modified nanowire using the limiting area of 0.28 nm^2 per a monomeric unit of ethylene oxide (Figure 5.2b). [187] On the other hand, by taking the limiting area of N-vinyl pyrrolidone monomer as 0.1 nm^2, the calculated surface area occupied by PVP, 1,170 nm^2, is estimated to be close to the experimental value indicating that PVP chains control the monolayer compression in the solid state even after modification with PEO chains. [188,189]

The Langmuir monolayer with Ag nanowires was deposited on the silicon wafers at three different surface pressures, P = 0.5, 25, and 35 mN/m (Figures 5.2 and Figure 5.3). As we observed, the nanowires were randomly distributed at very low pressure, P = 0.5 mN/m, but at P = 25 and 35 mN/m they become orientated parallel to LB barriers or perpendicularly to the dipping direction (represented by arrows in Figure 5.3). This type of orientation is the well known phenomenon for rod-like structures often compared to the behavior of rafted logs on a river. [87,171,172] Highly packed AgNWs showing excellent orientation are usually seen at the top of the silicon wafer but uniformity gradually decreases towards the bottom of the wafer due to the meniscus formed along wafer/water interface during dipping, a common behavior for a PEO-containing material (Figure 5.4a). [185,186] Closer examination of LB monolayers reveals occasional anisotropic voids with silver nanowires oriented along their boundaries (Figure 5.4b,c). AFM cross-sectional analysis yields the monolayer thickness of 3.5 $\pm$ 1 nm in the regions free of nanowires (Figure 5.4d). Despite these occasional defects, the Ag-PEO monolayer at the

highest surface pressure can be picked up on a copper plate with a pinhole with a 150 μm diameter (Figure 5.3d). The successful transfer of these monolayers indicates a fairly stable structure (although with some defects, such as big holes) with the overall strength sufficient to be freely suspended over the hole over extended periods of time. The angular disorientation of the LB-assisted silver nanowires is about 17^{o} with no nanowires deviating more than 30^{o} from the orientation direction (Figure 5.5) at a surface pressure, p=25 mN/m.

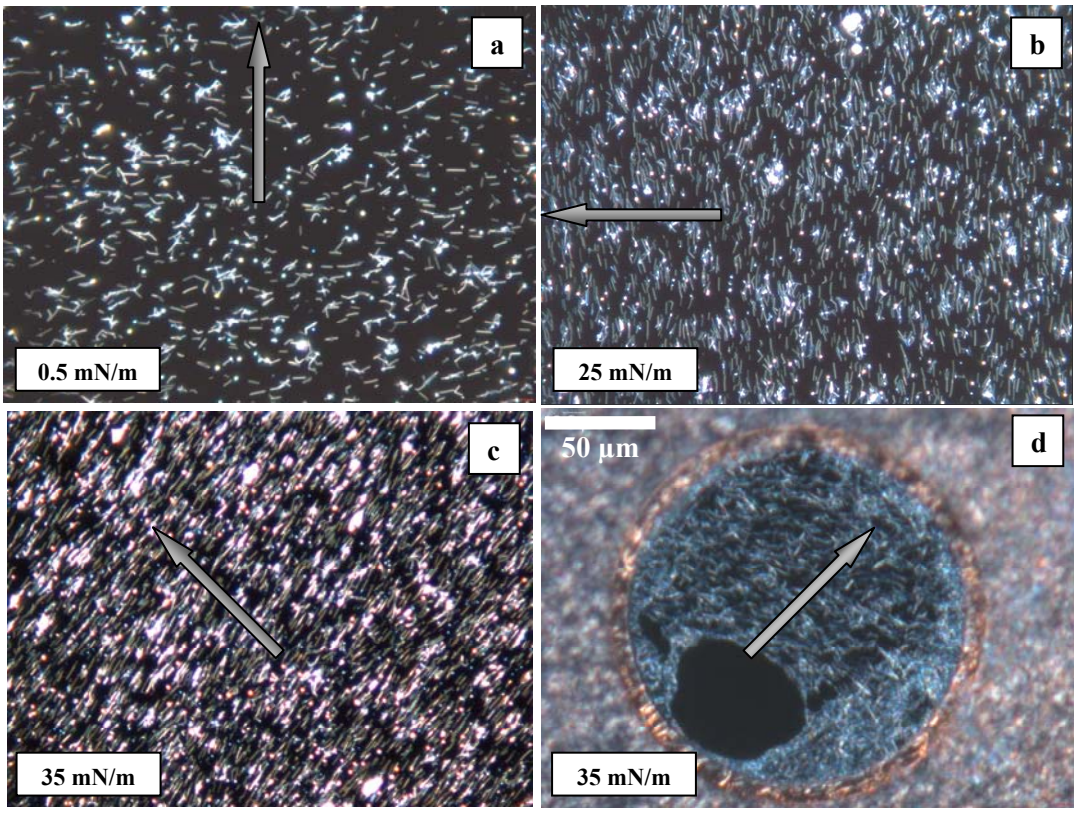

Figure 5.3. (a) Randomly oriented Ag-PEO nanowires deposited at low surface pressure. (b and c) Unidirectional orientation of Ag-PEO nanowires deposited at different surface pressures. (d) Unidirectional orientation Ag-PEO nanowires deposited over 150 μm hole. Arrows represent the dipping direction.

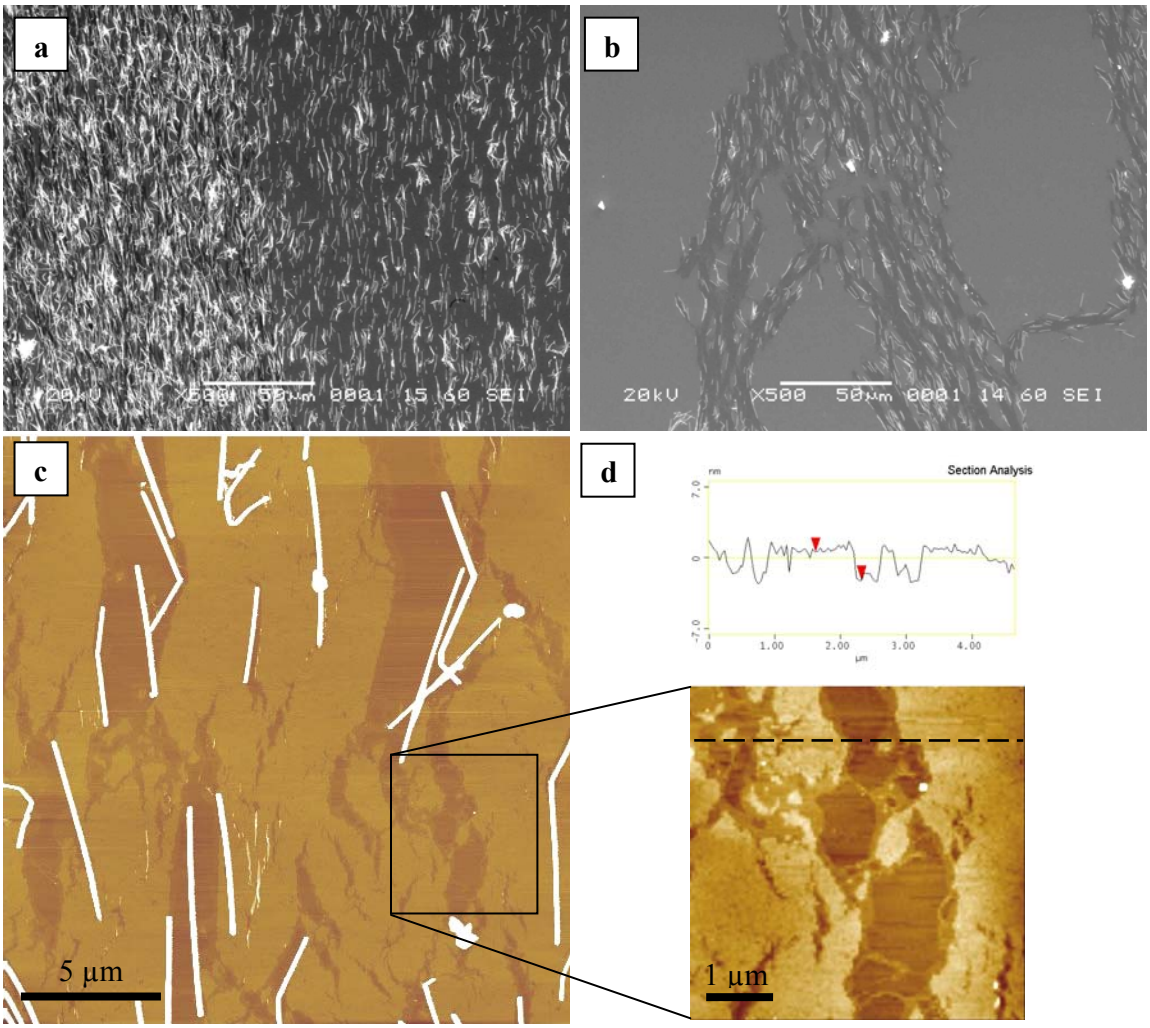

Figure 5.4. Ag-PEO nanowires monolayer deposited on a silicon wafer. SEM images for monolayer deposited at P = 25 mN/m at the (a) top and (b) bottom of the wafer (P = 35 mN/m). (c and d) AFM images of monolayer deposited at P = 35 mN/m with its corresponding cross-sectional analysis.

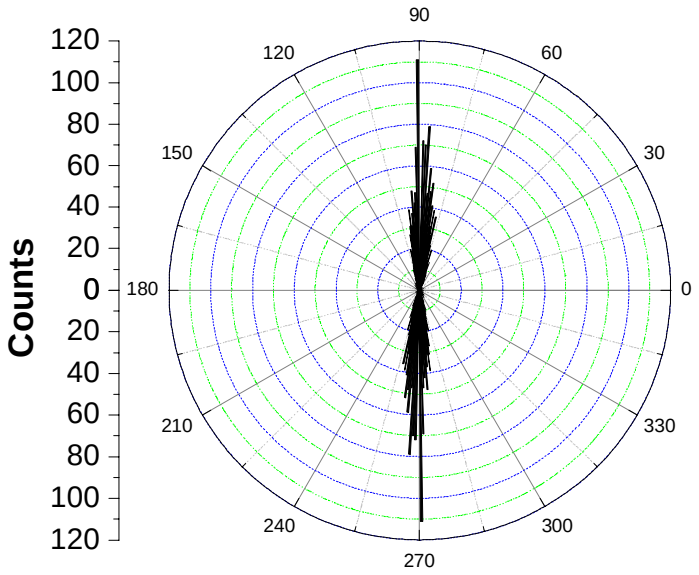

Figure 5.5. Angular distribution of nanowire orientations (°), Y-axis is count. Silver nanowires were oriented by LB compression at surface pressure, P = 25 mN/m).

5.3.2. Freely suspended polymer films with encapsulated silver nanowires

An array of uniaxially oriented silver nanowires was deposited at P = 25 mN/m in between two $(PAH/PSS)_{10}$ LbL films assembled on 200 nm thick SiO_2 layer, to form supported Ag-LbL film (Figure 5.6a). A thick SiO_2 layer rather than cellulose acetate in the previous chapter (Chapter 4) because SiO_2 layer is atomically smooth. A rough sacrificial layer can disrupt the orientation of silver nanowires during transfer. The films were released by dissolving the SiO_2 layer in 5% hydrofluoric acid solution (*hazardous solution!*). [190] The released films were transferred into another Petri dish containing acetone *via* pipette, and back into a fresh pool of nanopure water. Upon release from the SiO_2 sacrificial layer, LbL films were strong enough to survive the release and transfer procedures and moreover, can be freely suspended for a long time preserving nanowire

orientation, as demonstrated with a TEM copper grid (Figure 5.6b). Ag-LbL film deposited on a quartz substrate was used for UV/Vis measurement in comparison with solution state (Figure 5.7). AgNW solution has an absorption peak at 350 nm (with a shoulder around 380 nm), where the former resembles the bulk silver and the latter corresponds to the transversal plasmon mode. [186] For LbL films, a very similar shape is observed with main peak around 359 nm with a minor blue shift indicating changing environment. Minor shift indicates little interparticle interaction.

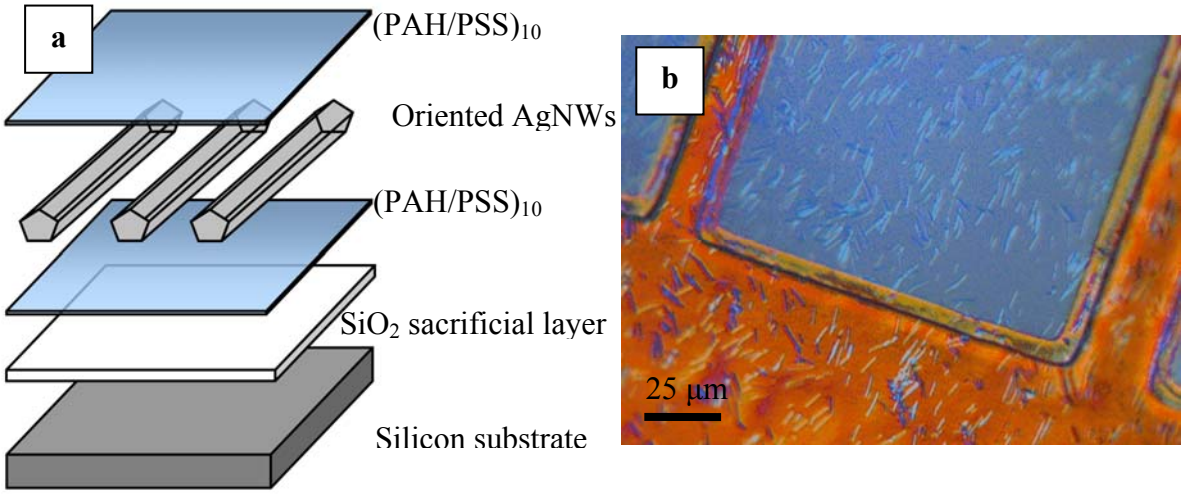

Figure 5.6. Fabrication of oriented silver nanowires sandwiched between two $(PAH/PSS)_{10}$ LbL films on a SiO_2 sacrificial layer. (b) Ag-LbL film suspended over the TEM grid.

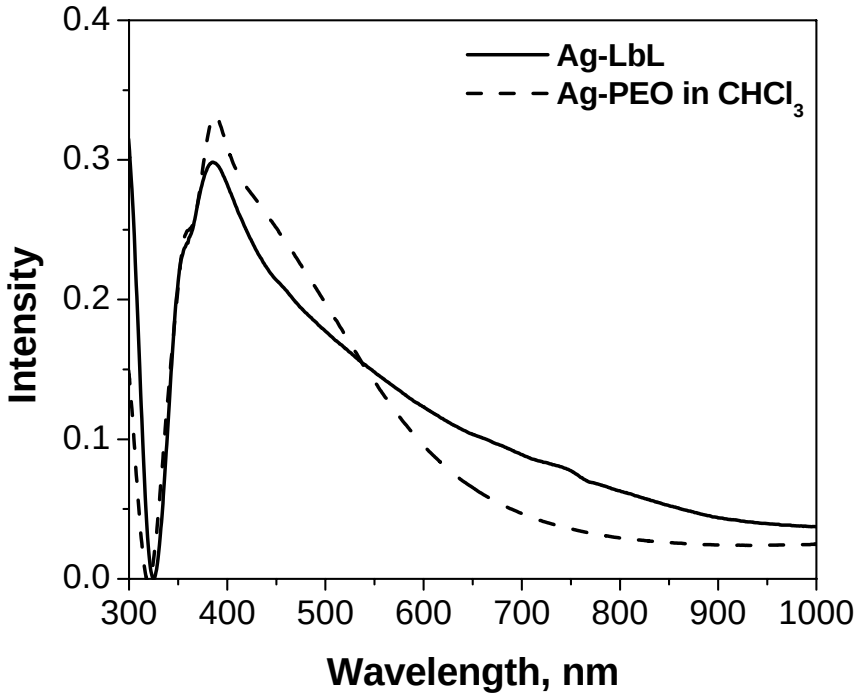

Figure 5.7. UV/Vis spectra of *Ag*-PEO nanowires in solution and encapsulated within LbL film.

5.3.3. Anisotropic mechanical behavior of LbL film with encapsulated oriented nanowires

To test the mechanical properties of ultrathin LbL films, they were deposited onto a PDMS substrate and a compressive stress was applied both parallel and perpendicular to the orientation of silver nanowires (Figure 5.8a). For both experiments, we observed long-range buckling instability patterns which differ by spacing and distribution of wrinkles (Figure 5.8 b,c). For the perpendicular compression, the buckling spacing, λ, was 2.6 ± 0.24 μm, while for the parallel compression, the average buckling spacing decreased to 1.5 ± 0.15 μm. It is worth noting that while for parallel compression the buckling spacing is more or less uniform, for perpendicular compression buckling

spacings are sporadic and localized in the regions where AgNWs directly oppose the compressive stress. This agrees with the observation of the two-stage buckling phenomenon for micropatterned encapsulated gold nanoparticle array composite films composed of regions with different stiffness. [191] This observation justified the application of the buckling theory to the composite films for the evaluation of the local mechanical properties because of highly superpositional nature of buckling instabilities occurring independently in regions with different local properties.

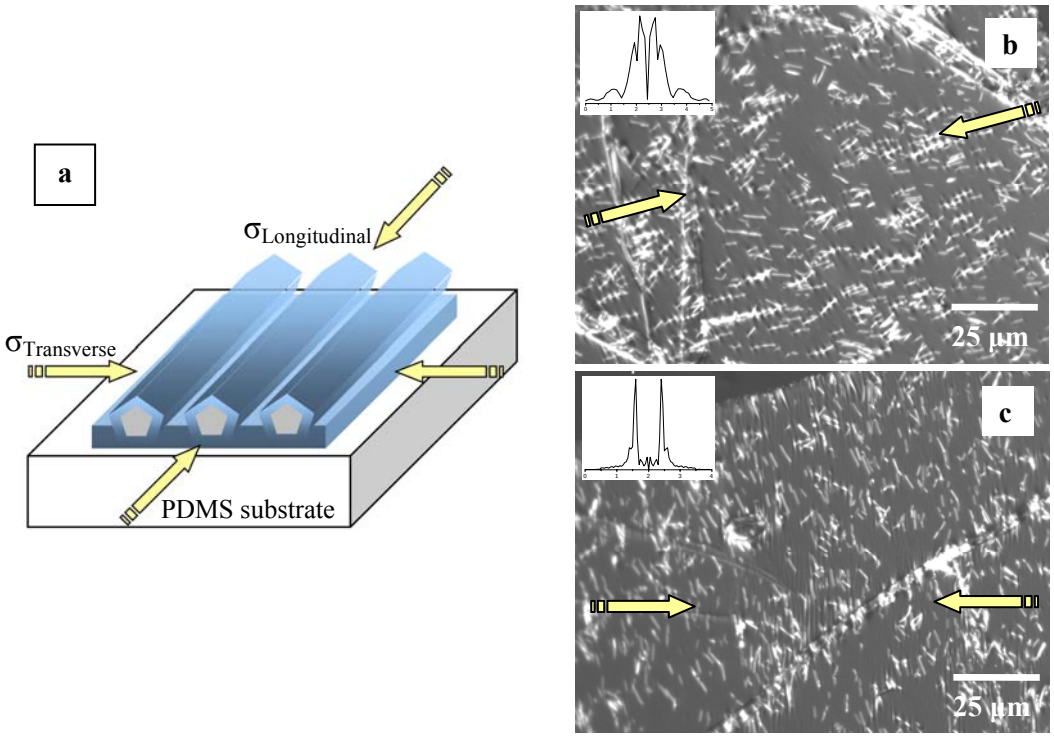

Figure 5.8. LbL film deposited on PDMS substrate and buckled in the longitudinal and transversal directions (a) and corresponding optical images (b, c). Insets are a representative 1D FFTs for selected cross-sections of buckled nanowires. X-axis is 1/λ (1/μm).

The application of the buckling instability theory yields the Young's modulus of 0.73 $\pm$ 0.5 GPa for the direction perpendicular to the nanowire orientation with much higher value of 3.82 $\pm$ 0.5 GPa obtained for the direction along the nanowire orientation. Using the Young's modulus for bulk silver, 88 GPa[192] and the Young's modulus of unfilled PAH/PSS polyelectrolyte film, 1.0 GPa , the theoretical Young's modulus of the composite film can be calculated both in the longitudinal and transversal directions using the Halpin-Tsai equation for anisotropic fiber reinforced composites (Appendix C). [193] These calculations yield E_T = 1.10 GPa and E_L = 2.95 GPa for transversal and longitudinal directions, respectively, for ϕ = 3.4%, in close agreement with the experimental data.

5.3.4. Buckling of silver nanowires

It is logical to expect that upon buckling in the longitudinal direction silver nanowires with the elastic modulus two orders of magnitude higher than that the polymeric matrix will keep their shape intact. However, optical images showed that the wrinkles were concentrated along the nanowires, an intriguing distribution (Figure 5.8b). Thus, to understand what takes place during buckling in longitudinal directions, LbL films were imaged with AFM while being subjected to the compressive force. For longitudinal buckling, AFM imaging reveals that the silver nanowires closely follow the undulated shape of the wrinkle pattern (Figure 5.9a, c). The silver nanowires are indeed buckled with amplitude exceeding 100 nm (Figure 5.9b). This is the well known phenomenon which is observed in bulk unidirectional, fiber-reinforced composites when subjected to significant compression loading. Fiber buckling in bulk can in fact occur

when the matrix stresses are in the elastic range for sufficiently low fiber volume fraction (< 40%). Due to silver nanowires confinement to the interior of the planar LbL film, even minor compressive strain below 0.2% initiate the nanowire buckling with 2-3 smooth modulated segments per nanowire (Figure 5.9).

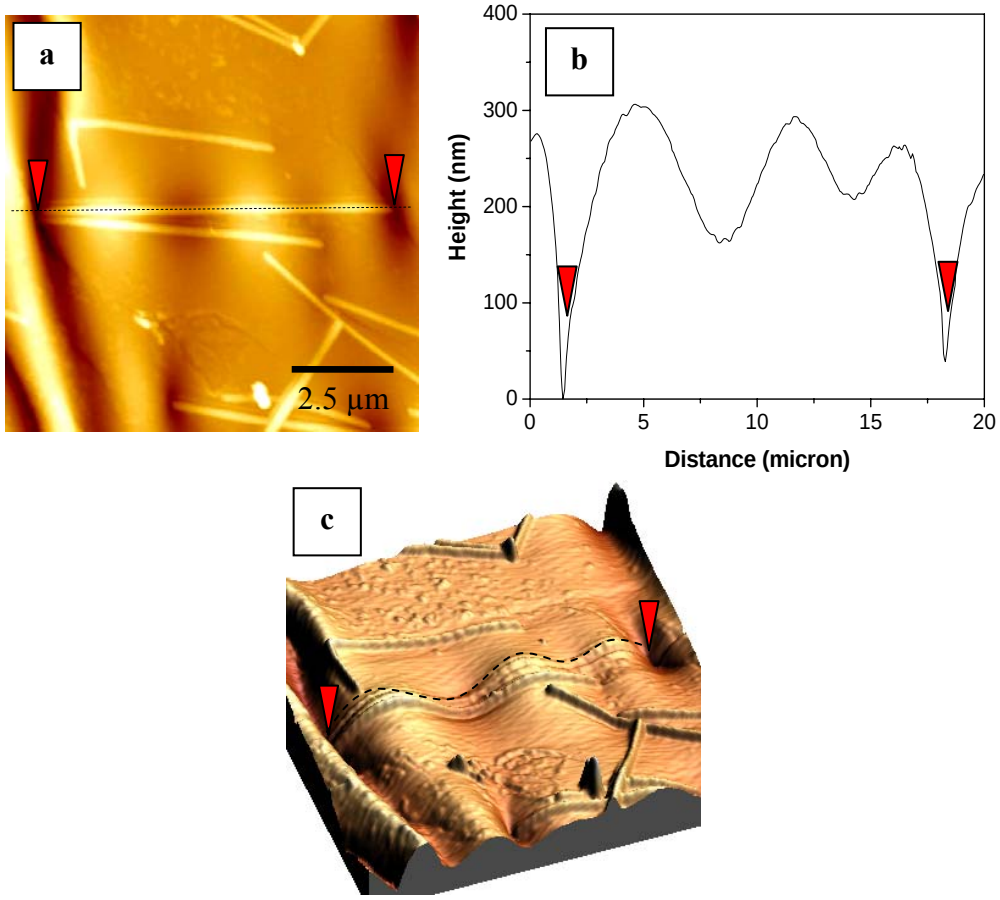

Figure 5.9. AFM images of Ag-LbL film buckled in the longitudinal direction, height is 500 nm, (a, c) and corresponding cross-section profile along a single buckled nanowire (along dotted line) (b). Red arrows mark the two ends of the undulated nanowire.

To elucidate if the compressive stress transferred by the polymer matrix is sufficient to deform silver nanowires, we estimated the stress developed by the

compressed PDMS substrate (see Appendix B) and compared this value with that needed to initiate the buckling instability of a column derived from Euler's equation: [194,195]

$$\sigma_{critical} = F / A = \left[\frac{(K\pi^2 E_{AgNW} I)}{l^2} \right] / (\pi r^2) \qquad (Equation\ 5.1)$$

with K = 4 (for a column fixed ends), $I = \pi \cdot R^4 / 4$ is moment of inertia, l is average nanowire length, and r is its average radius. This analysis confirmed that the compression stress developed by the polymer matrix can cause the nanowire buckling.

From this analysis we directly evaluated the elastic modulus of the silver nanowire in the longitudinal direction E_{AgNW} = 118 $\pm$ 14 GPa. This value is close to the 124 GPa determined for the (100) direction of silver single crystal [196] and within the range of elastic moduli determined by direct buckling of an individual nanowire from corresponding force-displacement measurements, 100-120 GPa. [197] However, this number is higher than that usually measured for the bulk silver as well as one measured for silver nanowires by nanoindentation (83-88 GPa). The higher Young's modulus of silver nanowire having penta-twinned cross section compared to bulk silver can be related to the grain boundary hardening effect imposed by the nanowire lateral facets as suggested earlier. Some differences could also be ascribed to the role of surface stiffness and different directions of mechanical deformations. [198] The readers are also recommended to see reference 199 for an alternative Young's modulus determination for buckled rod placed on PDMS substrate. The phenomenon of the buckling of the silver

nanowires encapsulated into ultrathin polymer film by the application of the compressive stress along their long axis represents the straightforward and fast way for the evaluation of the elastic properties of the metal nanowires by measuring their buckling periodicity.

In Chapter 4, the prediction of Young's modulus of the randomly oriented nanowire-filled LbL film ($0 \leq \phi$ (%) ≤ 22.5) was determined according to the Halpin-Tsai equation using the literature silver nanowire Young's modulus, E_{AgNW} = 88 GPa, and was found to be in a close agreement for $\phi \leq 7.5\%$. At a higher volume fraction of silver nanowires they form multilayer and compromise the nanowire-to-matrix interactions, and hence the overall micromechanical properties. If the Young's modulus of these silver nanowires were in fact E_{AgNW} = 118 GPa, it is worth considering how much difference would the predicted Young's modulus of randomly oriented nanowire-filled LbL film would be. Figure 5.10 compared the Young's moduli calculated according to the two assumed Young's modulus of silver nanowire. It can be seen from Figure 5.10 that the error in the prediction is within 20%. Furthermore, the Halpin-Tsai prediction for the longitudinal and transversal modulus for E_{AgNW} = 118 GPa would be, E_L = 3.4 GPa E_T = 1.1 GPa, which is in a closer agreement with experimental, *i.e.*, the experimentally measured Young's moduli were: $E_L = 3.82 \pm 0.5$ GPa and $E_T = 0.73 \pm 0.5$ GPa.

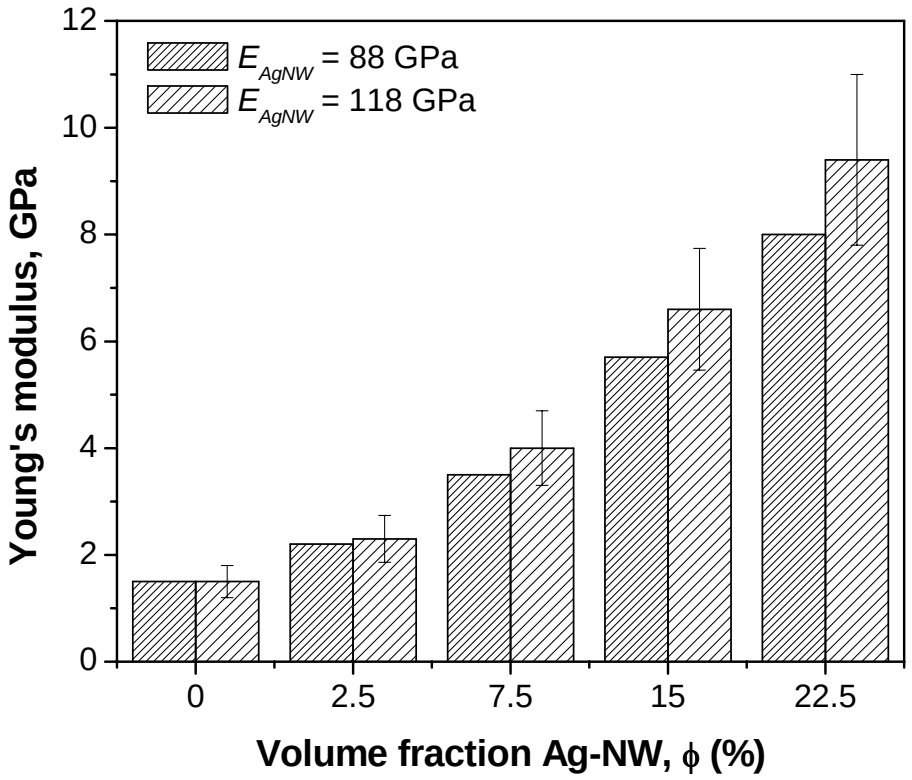

Figure 5.10. Comparing the predicted Young's modulus according to Halpin-Tsai equation for randomly oriented nanowire-reinforced composite film ($0 \leq \phi\ (\%) \leq 22.5$). Error bar indicates 20% standard deviation.

In summary, as an extension from previous work, an array of silver nanowires was unidirectionally aligned by means of Langmuir-Blodgett technique. The unidirectionally oriented silver nanowires were sandwiched into layer-by-layer film to give an anisotropic composite film with much stiffer (fivefold) properties in the direction of nanowire orientation. The value is 0.73 ± 0.5 GPa for the direction perpendicular to the nanowire orientation with much higher value of 3.82 ± 0.5 GPa obtained for the direction along the nanowire orientation. This difference is caused by the fact that under a longitudinal compressive stress (parallel to the direction of orientation), the individual

nanowires undergo the buckling process, thus, contributing into the higher composite stiffness of the film. This matrix-induced buckling phenomenon can be used as a fast and straightforward method of measuring the elastic modulus of metallic nanowires from the buckling spacing with good precision. Using Euler's equation for the buckling instability of a slender column, the Young's modulus of the buckled silver nanowires array was determined to be 118 $\pm$ 14 GPa, which is higher than the bulk silver but falls within the range of values obtained with other independent measurements.

CHAPTER 6

TERMINAL GROUP MODIFICATION OF FUNCTIONALIZED $(X\text{-}PEO)_2\text{-}(PS\text{-}Y)_2$ STAR POLYMER LINKER

6.1 Introduction

Novel macromolecular architectures such as highly-branched and star-shaped block copolymers have been found to exhibit novel aggregation behavior [200,201,202,203,204] and complex intramolecular interactions [205] in solution, surfaces, and interfaces. [206,207,208,209,210,211,212,213] Unique morphologies were found in branched and star block copolymers that were not observed for linear block copolymers. [214,215,216,217,218,219] Recent studies have extended towards more sophisticated copolymer architectures ranging from H-shaped, π-shaped,[220,221] Vergina-star,[222] dumbbell-shaped,[223] ABC star-shaped,[224] and dendrimer-like star block copolymer[225] motivated and made possible by recent rapid development in controlled living polymerization (CLP) techniques.[226] In order to obtain polymers with such architectural intricacy, combining two or more polymerization techniques is required. The result is a polymer with dissimilar end-functional groups.

In this work, a previously synthesized four-arm $PEO_2\text{-}PS_2$ star polymer that was synthesized from a combination of ionic and ATRP living polymerization was undergone terminal group modifications. The different terminal groups on the PEO arms than the PS arms allows it to be used as a linker, as to be described in the next chapter. In a related publication, we had also demonstrated that the nature of terminal groups

(hydrophobic or hydrophilic) with respect to the hydrophilic PEO and hydrophobic PS arms can affect their self-aggregation behavior in a two-dimensional scheme.

6.2 Chemicals and materials

Using 2,2-dimethyl-5,5-bis(hydroxyl methyl)-1,3-dioxane as a core, amphiphilic heteroarm PEO_2-PS_2 star copolymers were initially synthesized by growing two PEO arms by anionic polymerization of ethylene oxide, which was then terminated with tert-butyl diphenyl silane (TBDPS) protecting group. Two polystyrene arms were then grown by atom transfer radical polymerization (ATRP) to make star copolymer $(TBDPS\text{-}PEO)_2$-$(PS\text{-}Br)_2$ (**1**), shown in Scheme 6.1. The detailed synthetic procedure for PEO_n-PS_m heteroarm star copolymers used here is described earlier. [227] These star-block copolymers possess a low polydispersity index, as confirmed by gel-permeation chromatography (GPC) and nuclear magnetic resonance (NMR) (Table 6.1). In the molecular weight calculation using proton NMR, TBDPS group was used as the reference peak highlighted in gray in Table 6.1. Without the TBDPS reference peak, molecular weights of the rest of the polymers are assumed to be the identical. Hydrodynamic behavior of star copolymers in GPC measurement is responsible for the substantial difference in the measured molecular weight values with respect to those measured by NMR.[228]

Scheme 6.1. Synthesis of $(Br\text{-}PS)_2\text{-}(PEO\text{-}TBDPS)_2$

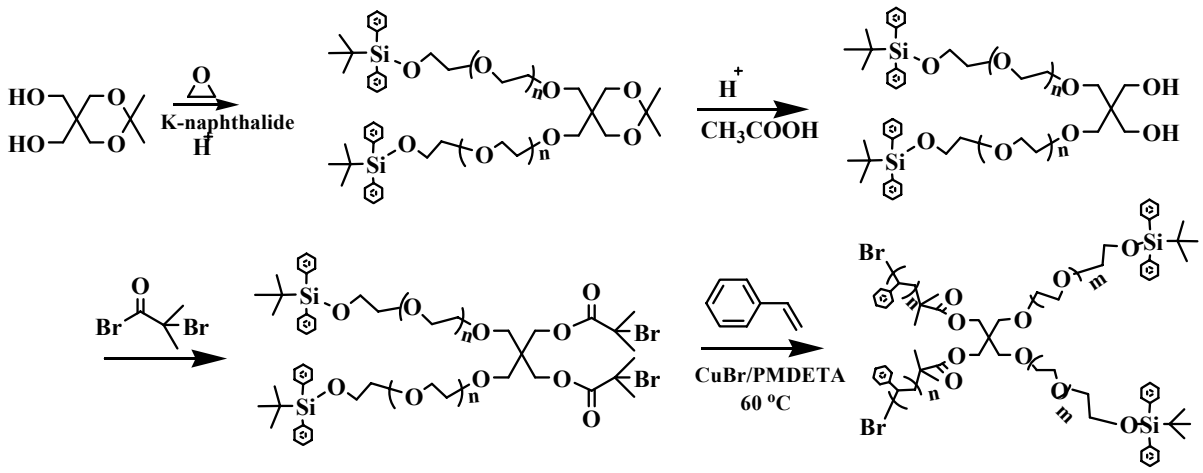

Table 6.1. Properties of heteroarm star block copolymers.

No.	Polymer	GPC data			NMR Data					
					PEO arm			PS arm		Total M_n, 10^3
		M_n, 10^3	M_w, 10^3	PDI	M_n, 10^3	N	φ	M_n, 10^3	N	
1	$(Br\text{-}PS)_2\text{-}(PEO\text{-}TBDPS)_2$	14	18	1.31	7.5	170	0.32	14	135	43
2	$(Br\text{-}PS)_2\text{-}(PEO\text{-}OH)_2$	17	20	1.20	7.5	170	0.32	14	135	43
3	$(Br\text{-}PS)_2\text{-}(PEO\text{-}COOH)_2$	17	20	1.18	7.5	170	0.32	14	135	43
4	$(NH_2\text{-}PS)_2\text{-}(PEO\text{-}TBDPS)_2$	19	23	1.22	7.5	170	0.32	14	135	43
5	$(NH_2\text{-}PS)_2\text{-}(PEO\text{-}OH)_2$	17	21	1.22	7.5	170	0.32	14	135	43
6	$(NH_2\text{-}PS)_2\text{-}(PEO\text{-}COOH)_2$	16	19	1.20	7.5	170	0.32	14	135	43

M_n is number average molecular weight, M_w is weight average molecular weight, N is number of monomeric units, and φ is a volume fraction of PEO block.

6.3. Results and discussions

Scheme 6.2 summarizes the synthetic procedures as described in literature and presented briefly here. The treatment of polymer **1** (0.0154 mmol, 630 mg) with 1 M tetrabutylammonium fluoride, TBAF (1.54 mmol, 401.8 mg), in THF (25 mL) overnight gives polymer **2**.[229] ^{1}H-NMR spectra demonstrate successful removal of TBDPS protecting group as indicated by the disappearance of peak **a** and **b** in Figure 2a.

Polymer **2** (0.00266 mmol, 209 mg) was reacted overnight with succinic anhydride (0.053 mmol, 5.3 mg) in the presence of 4-dimethylaminopyridine, DMAP (0.00260 mmol, 0.32 mg), in pyridine (1.5 mL) to give polymer **3**.[230,231] The succinic acid anhydride signal is notated by letter **i** in Figure 6.1b. ^{1}H-NMR spectrum of $(Br)_2$-**S**-$(TBDPS)_2$, and ^{1}H-NMR spectrum of $(Br)_2$-**S**-$(COOH)_2$ (δ, ppm, $CDCl_3$): 7.3-6.3 (m, 20H, aromatic), 3.6 (s, 4H, $(CH_2CH_2$-O)n, PEO block), 1.32 ppm (s, 6H), 1.05 (s, 18H, $C(CH_3)_3$), 2.5-2.7 (t, succinic acid). "x" are solvent signals.

The bromine functional groups of polymers **1** through **3** were each converted into amine groups in three steps to give polymers **4**, **5** and **6** respectively, according to the procedure described in literature.[232] The transformation of the bromine group into azide (N_3) and further to triphenylphosphine group was confirmed by the presence of a peak at about 33 ppm in ^{13}P-NMR spectrum, Figure 6.1c. The signal for non-chemically bonded triphenylphosphine occurs at about -10 ppm. The absence of a peak at 33 ppm following hydrolysis of triphenylphophine group yields amine functional groups. ^{13}P-NMR of $(NH_2)_2$-**S**-$(OH)_2$ (δ, ppm, $CDCl_3$): -4.4 (s, triphenyl phosphine) and 30.5 (s, chemically bonded triphenyl phosphine). Purification of the polymers at every stage was done by precipitation in methanol that resulted in an average yield of 65 to 75%.

Scheme 6.2. Synthetic path for functional group modification of $(Br\text{-}PS)_2$-$(PEO\text{-}TBDPS)_2$ and conditions: (a) TBAF/THF; (b) azidation by NaN_3/DMF; (c) $P(Ph)_3$/THF; (d) hydrolysis by H_2O/THF (e) succinic anhydride, DMAP/pyridine.

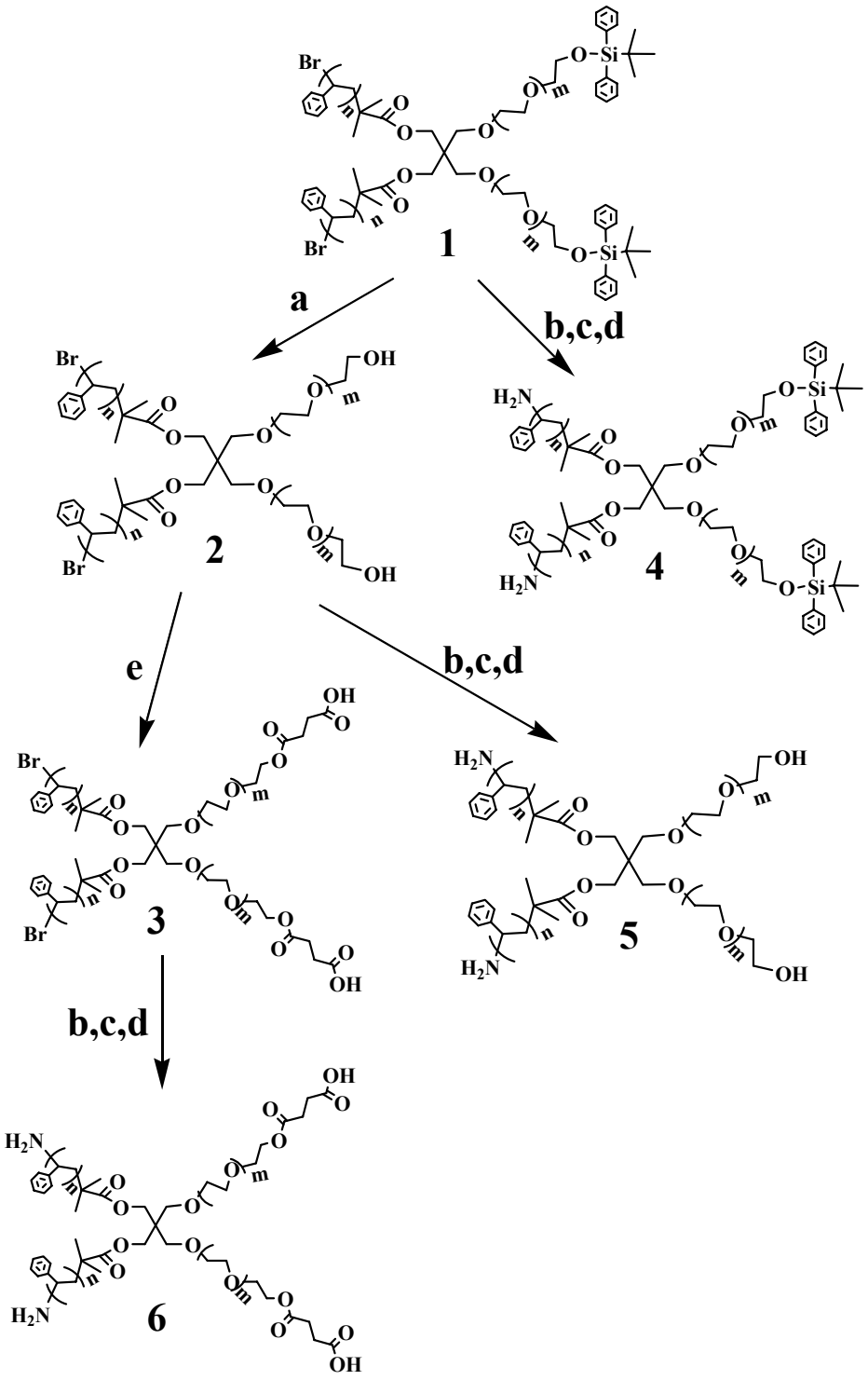

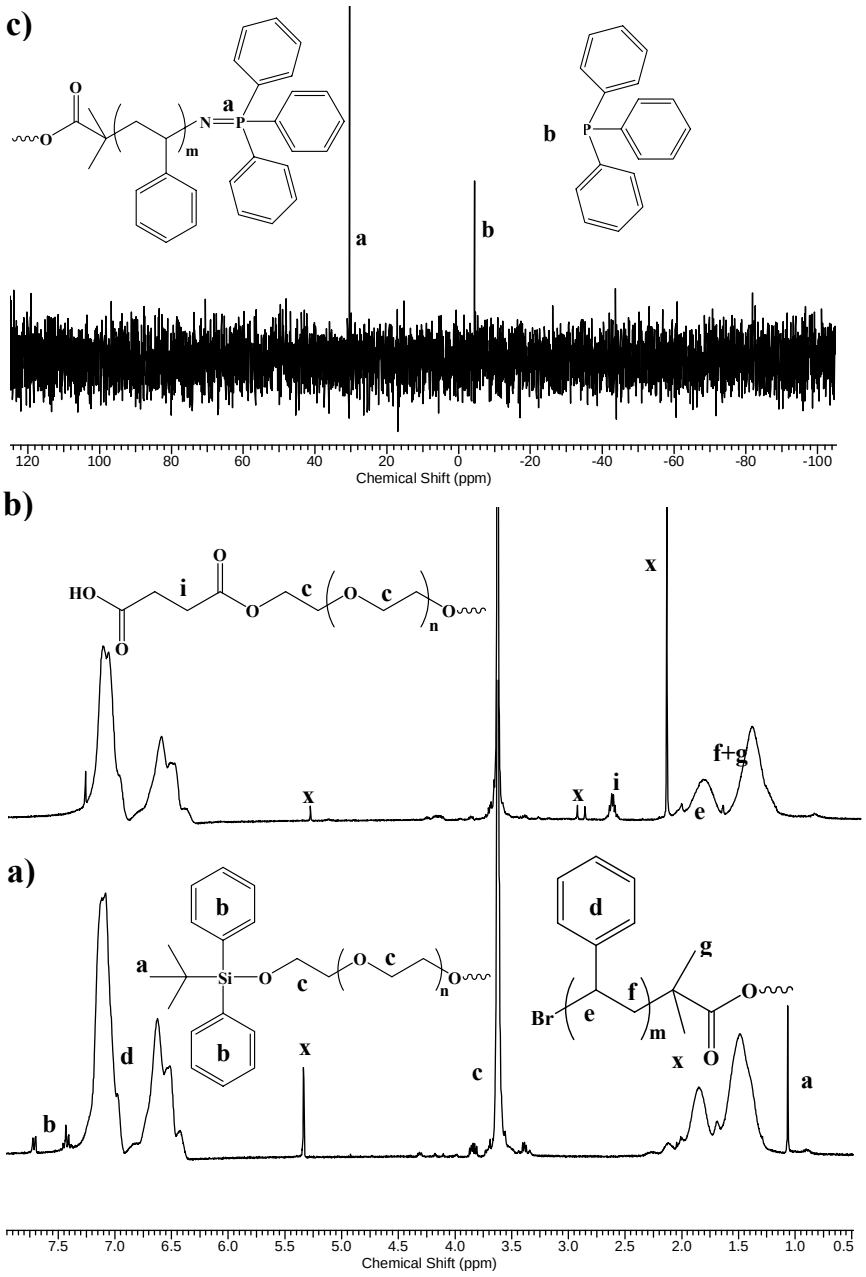

Figure 6.1. (a) $(Br)_2$-**S**-$(TBDPS)_2$; (b) ^{1}H-NMR spectrum of $(Br)_2$-**S**-$(COOH)_2$, and (c) ^{13}P-NMR of $((Ph)_3P{=}N)_2$-**S**-$(OH)_2$ and $P(Ph)_3$; "x" are solvent peaks.

Chemical modification of polymer **1** yields a range of the 4-arm amphiphilic star copolymers $(X\text{-}PEO)_2$-$(PS\text{-}Y)_2$ with different terminal groups, X and Y (Scheme 6.2). To simplify the notation, we use a shorter abbreviation $(X)_2$-**S**-$(Y)_2$ with **S** standing for the

star core and X and Y standing for different types of terminal groups (two groups for each type of arms). Table 6.2 summarizes the various combinations of terminal groups that are introduced here.

Table 6.2. List of functionalized $(X\text{-}PEO)_2\text{-}(PS\text{-}Y)_2$ heteroarm star copolymers.

No.	Polymer	Abbreviations
1	$(Br\text{-}PS)_2\text{-}(PEO\text{-}TBDPS)_2$	$(Br)_2\text{-}\mathbf{S}\text{-}(TBDPS)_2$
2	$(Br\text{-}PS)_2\text{-}(PEO\text{-}OH)_2$	$(Br)_2\text{-}\mathbf{S}\text{-}(OH)_2$
3	$(Br\text{-}PS)_2\text{-}(PEO\text{-}COOH)_2$	$(Br)_2\text{-}\mathbf{S}\text{-}(COOH)_2$
4	$(NH_2\text{-}PS)_2\text{-}(PEO\text{-}TBDPS)_2$	$(NH_2)_2\text{-}\mathbf{S}\text{-}(TBDPS)_2$
5	$(NH_2\text{-}PS)_2\text{-}(PEO\text{-}OH)_2$	$(NH_2)_2\text{-}\mathbf{S}\text{-}(OH)_2$
6	$(NH_2\text{-}PS)_2\text{-}(PEO\text{-}COOH)_2$	$(NH_2)_2\text{-}\mathbf{S}\text{-}(COOH)_2$

In summary, a different "mortar" material was explored in this work. A heteroarm star polymer, $(X\text{-}PEO)_2\text{-}(PS\text{-}Y)_2$ prepared from a combination of ionic and atom transfer radical polymerization (ATRP) bears different terminal groups. Ionic polymerization was used to grow the polyethyleneoxide (PEO) arm, and ATRP was used to grow the polystyrene (PS) arm. Various X and Y combinations of terminal groups at the ends of PS and PEO chains were explored in this work, which respectively include: Br/TBDPS, Br/OH, Br/COOH/, NH_2/TBDPS, NH_2/OH, and NH_2/COOH. They will be used for assembly of nanoparticles in the subsequent work.

CHAPTER 7

BIMETALLIC SILVER-GOLD NANOCOBS: DECORATING SILVER NANOWIRES WITH GOLD NANOPARTICLES

7.1. Introduction

Hybrid organic-metal and metal-metal nanostructures are critical for further advances in a design of efficient nanomaterials for chemical and biosensing via optical response. Raman shifts serving as signature for different chemical groups can be used for sensing of analyte molecules.[233] Coupling of plasmon resonances in adjacent metal nanostructures separated by nanoscale gaps is considered to be important for maximizing the enhancement of Raman scattering. Silver and gold nanoparticles possess distinctive absorption peak(s) within the visible and near-infrared region that can be tuned with shape, dimensions, inter-particle distance, and orientation, as supported by theoretical models. [234, 235] Experimentally, the methods of their syntheses are becoming commonplace leading to the production of high-quality and yield in grams quantity. [, 236, 237, 238, 239] Hybrid nanostructures are exploited as molecular rulers, [240] pH-meters, [241] light coupling nanowires, [242] and responsive microgels for medical applications, [243, 244] high-efficiency light-emitting structures, [245] and superlattices [246] with prospective applications as spectroscopic sensors, microoptics, waveguides, and optical computing elements.

Metal-metal nanostructures such as gold-silver core-shell nanoparticles have been recently introduced as active centers for surface enhanced Raman scattering (SERS). [247, 248] Multi-component hybrid metallic nanoparticles in the form of bimetallic alloys, core-

shells, [249] or particle-on-particle assemblies [250, 251] are another new class of materials that can lead to synergistic, novel properties. Some examples include silver-gold bimetallic nanowires, [252] CoPd nanocorns, [253] nanorice and dimers, [254,255] and hybrid gold nanoparticles on gold nanorods. [256] Detectable plasmon resonance shift is observed for these nanoparticles as a function of environmental dielectric constant, inter-particle distance, and orientation for anisotropic particles. An effective nanoparticles-based surface enhanced Raman substrate is often related to "hot spots" of nanoparticles aggregates, cross-junctions, or certain geometrical features of non-spherical nanoparticles responsible for high localized electromagnetic field. [257, 258, 259, 260]

Designing one-dimensional SERS-active structures which combine both high enhancement and uniformly oriented arrays capable of directional response is critical for prospective chemical sensing applications. [261] Tailoring of metal-metal nanostructures with a tunable gap between them is considered to be critical for designing plasmonic lattices with responsive optical properties. [262, 263] For instance, pairing of silver nanowires with nanoscale gaps between them was discussed as an effective means for sensing. [264] For the same reason, highly aligned nanowire bundles and multiwalled nanotubes have also been suggested for SERS arrays. [265, 266, 267]

Synthesis of core-shell bimetallic nanowires was utilized to increase SERS activity manifold similar to that designed for spherical nanoparticles. [, 268] Although a single nanowire SERS activity can in fact be achieved with proper selection of growth modes and polarization conditions, the overall SERS activity is generally compromised

due to reduced interaction with laser beams because of the shift of adsorption associated with longitudinal resonances far into the infra-red region. [, 269] The close match of the lattice spacings for silver and gold and their likelihood for their mutual displacement are favorable for alloyed nanoparticles, but not desirable for core-shell nanoparticles which is composed of separated layers of distinctive elements. [262, 270, 271, 272] Simple bimetallic core-shell without interlayer or using silicon oxide as an interlayer prevents the utilization of this "inner shell" space as prospective highly desirable hot spot for analyte molecules which can be created by growing gold nanoparticles on functionalized surfaces, as demonstrated by Halas. [273] Therefore, to fabricate SERS-active one-dimensional nanostructure such as bimetallic nanowires with enhanced SERS ability, novel designs should be sought.

Herein, we report a novel design of hybrid, bimetallic, silver-gold, core-double shell nanowires with greatly enhanced SERS ability. In this design, gold nanoparticles decorate the surface of silver nanowires aided by three-arm star polymer with functional terminal groups, which act as a linker (Figure 7.1). Gold nanoparticles form effective hybrid (polymer-gold) shell of 13 nm thick with 4 nm gold nanoparticles embedded within the polymer shell around a 65 nm silver core (Figure 7.1). We demonstrate that such hybrid, silver-gold nanowires resembling nanocobs, possess very significant SERS activity greatly exceeding (by about two orders of magnitude) Raman scattering from isolated "naked" silver nanowires. Moreover, it is manifold higher than that at the gap between two neighboring silver nanowires which is considered as the most efficient current SERS design for one-dimensional metal nanostructures.

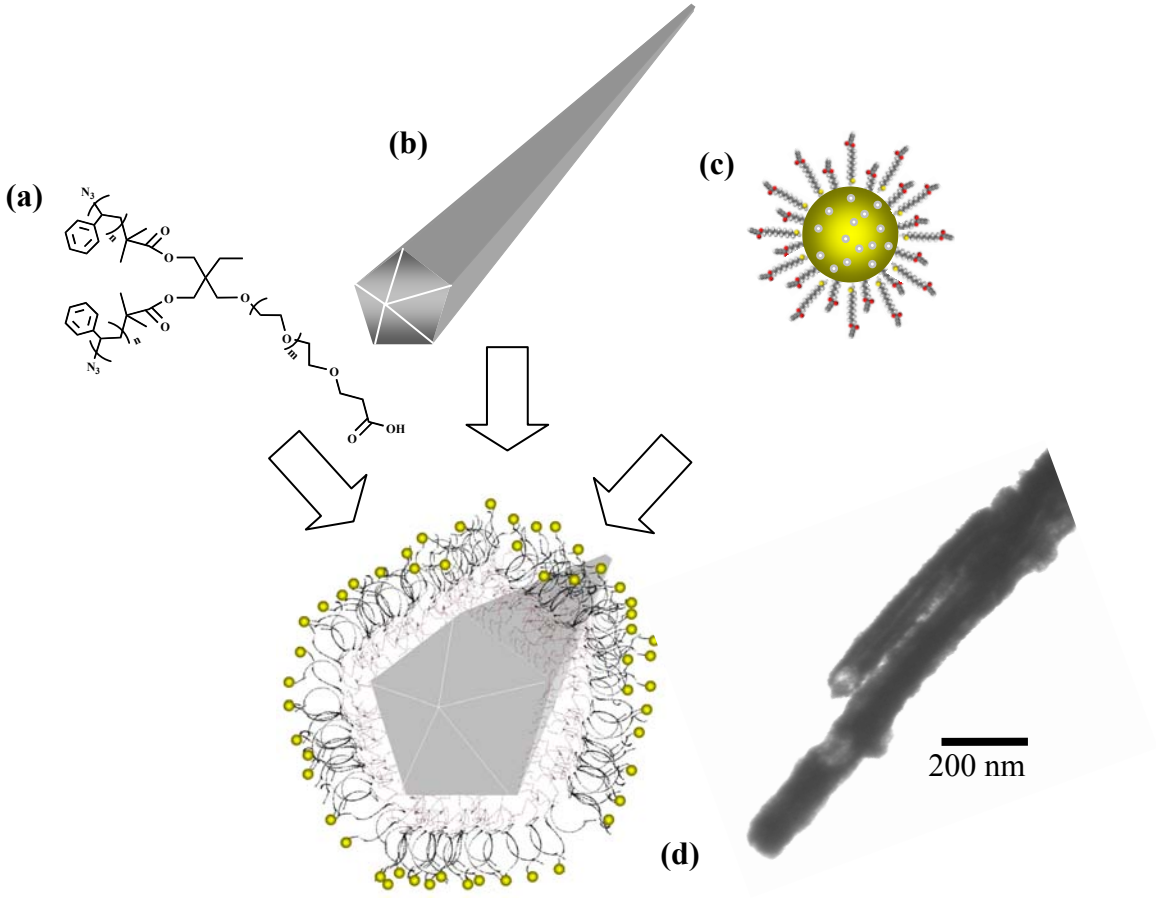

Figure 7.1. The three pre-formed building blocks: (a) PEO_1PS_2 star polymer modified with -COOH and $-N_3$ terminal groups, (b) Silver nanowire functionalized with 11-mercaptoundecanoic acid, (c) Gold nanoparticle functionalized with propynyl-11-mercaptoundecanoate, and (d) Silver-gold hierarchical hybrid nanostructure and corresponding TEM image at low resolution.

7.2. Sample preparations

7.2.1. Chemicals and materials

Assembly of pre-formed gold spherical nanoparticles (diameter = 4.1 $\pm$ 1 nm) has been conducted on the surface of one-dimensional silver nanowires (diameter = 65 $\pm$ 5

nm and lengths = 6 $\pm$ 2 μm) [274] aided by three-arm star polymer with functional terminal groups, which acts as a linker and as a shell.

The three-arms star polymer, (tert-butyldiphenylsilane-polyethyleneoxide)-S-(polystyrene-Bromine) or (TBDPS-PEO_1)-S-$(PS\text{-}Br)_2$ [275] was modified to obtain (COOH-PEO_1)-S-$(PS\text{-}N_3)_2$ according to the procedures described in the previous chapter (Figure 7.1a). [276] Its total molecular weight is M_n = 54,800 (PDI = 1.18) as determined from NMR and gel permeation chromatography (GPC). [277] From arm-disassembling technique, its composition was determined to be 159 units of ethylene oxide (M_n = 7,100) and 230 units of styrene (M_n = 23,900) for each of the PS arms. The functionalization of the PS arms with azide terminal groups provides a means for chemical grafting of ethyne-terminated gold nanoparticles around silver nanowires. Asymmetrical star polymer A-B_2, suggested here as a linker instead of traditional linear polymers has the ability to form much denser functionalized surface due to the fact that two functionalized PS chains exist per a single PEO chains grafted onto the silver surface.

7.2.2. Surface modification of silver and gold nanoparticles

The purified silver nanowires were initially capped by polyvinylpyrrolidone (PVP), and the spherical gold nanoparticles were capped with tetraoctylammonium bromide (TOAB) surfactant. The silver nanowires were treated with ligand-exchange reaction with 11-mercaptoundecanol under continuous stirring at room temperature (Figure 7.1b). [87] It precipitated within one-hour following the ligand exchange. Hierarchical assembly of the three pre-formed blocks involved estertification and click-

reaction. Estertification reaction between three-arm star polymer linkers and hydroxyl groups on 11-mercaptoundecanol functionalized silver nanowires was done in dry DMF under room temperature stirring for overnight according to the known procedure.[278] As for the spherical gold nanoparticles, propynyl-11-mercaptoundecanoate ligand was used (Figure 7.1c). The ligand-exchange reaction was achieved through phase-transfer reaction in accordance with a usual procedure. [279, 280] Functionalized gold nanoparticles were chemically grafted to azide groups by means of click-chemistry. [281, 282, 283] The final product was washed vigorously by repeated centrifugation and re-dispersion in excess of solvents until the supernatant was transparent. Considering our previous data on surface structure of this star block copolymer, we expected to have a polymer shell with a thickness of about 4 nm composed of PEO segments close to silver surface and PS chains in an outer shell. For modest grafting density the area per star molecule estimated from a mid-point of low-pressure plateau of Langmuir monolayers is 125 nm^2, and hence the density of the functionalized groups available for grafting gold nanoparticles can be estimated to be about 60 nm^2/group.

7.3. Results and discussions

SEM demonstrates dispersed morphology of the modified silver nanowires, with EDX spectroscopy confirming their gold-silver composition (Figure 7.2a, b). High-resolution TEM reveals the gold nanoparticles embedded within the PS matrix in the course of grafting in good solvent (Figure 7.2c). The average shell thickness was determined to be 13 $\pm$ 5 nm with occasional aggregates also observed. The distance that separates the gold nanoparticles from silver nanowires is 4.3 $\pm$ 1.4, and is similar to that

expected from the thickness of star polymer monolayer. Both TEM and AFM images show that the grafted gold nanoparticles are coated with polymer layer (compare surface morphology of original silver nanowires and silver-gold nanocobs) (Figure 2c, d, e).

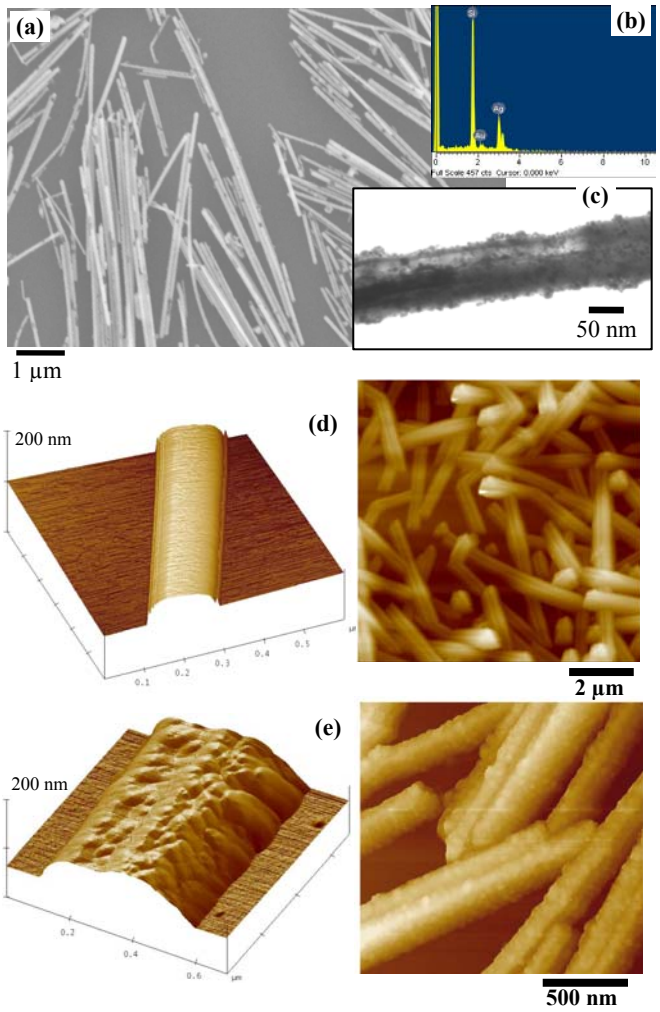

Figure 7.2. Silver-gold nanocobs: (a and b) SEM image and its corresponding EDX spectrum, and (c) high resolution TEM image. AFM height images of: (d) as-synthesized silver nanowires (z = 200 nm), and (e) silver-gold nanocobs.

Direct counting on TEM image shows average of 27 $\pm$ 10 particles over 50 x 50 nm^2 surface area (corrected for curvature). The grafting density of about 80 nm^2/nanoparticle deduced from these data is close to that estimated for the density of functional terminal groups (60 nm^2/group) suggesting that most of terminal groups participated in grafting. This grafting density corresponds to 21% surface coverage, about half of the maximum area coverage for randomly-placed circular features ("jamming" limit) of 55%. [284] The overall number of gold nanoparticles can be estimated as $1.8x10^4$ per a single nanowire with a liner density as high as 250 gold nanoparticles surrounding every 100 nm length of the silver core. This is much higher than that obtained for other combinations.

The Raman spectra (λ = 514.5 nm, surface area 4 x 4 μm) obtained from dense silver-gold nanocobs and original silver nanowires with star polymer linker similar to that in Figure 7.2a showed several strong bands (Figure 7.3a). The Raman peaks at 1000 cm^{-1}, 1360 cm^{-1} and 1580 cm^{-1} can be attributed to the symmetric ring breathing, [285] bending and wagging of CH_2 groups and in-plane C-C stretching of phenyl rings from PS chains, respectively. [286] A contribution around 2900 cm^{-1} corresponds to (CH) stretching vibrations (barely seen in plots because of scaling). [286, 287] The intensity of the main Raman bands after decorating with gold nanoparticles increased dramatically, by thirty-fold, (Figure 7.3a). Even more pronounced increase is observed for isolated nanowires with overall increase reaching 50-80 times after decorating with gold nanoparticles (Figure 7.3b). In addition, we observed significant enhancement when the polarization direction is 90° with respect to nanowire longitudinal-axis (Figure 7.3c). The SERS

enhancement estimated from 1580 cm^{-1} band is 5-6 higher for the polarization direction perpendicular to the main axis (Figure 7.3c).

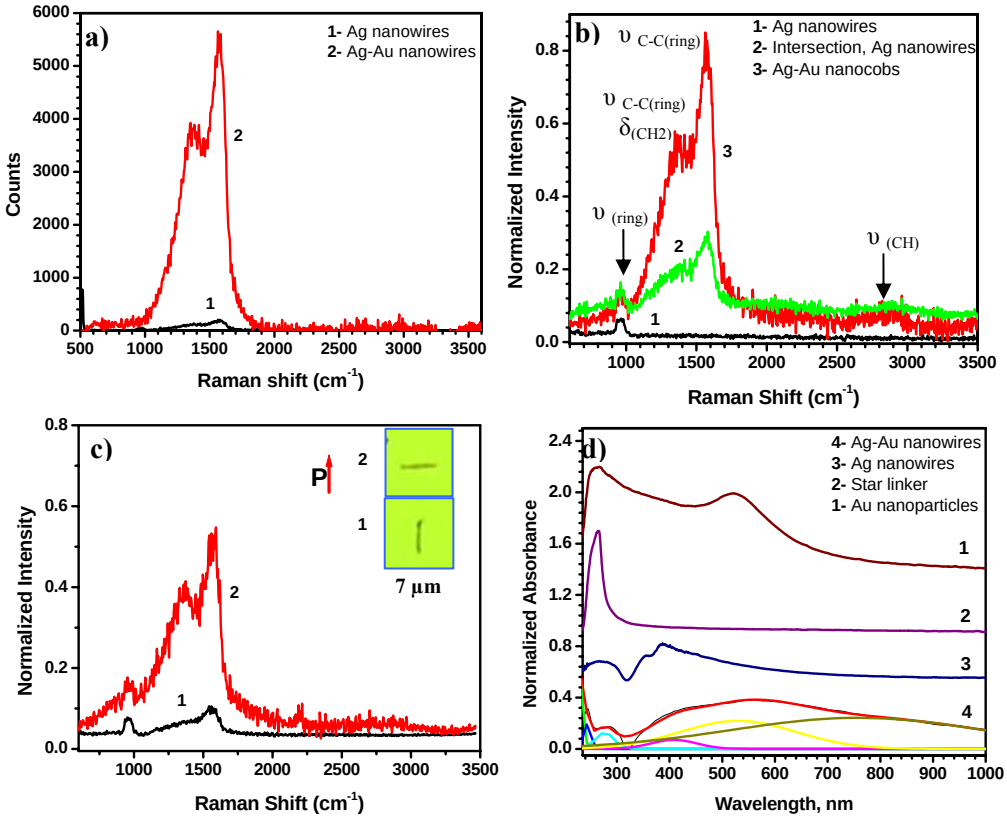

Figure 7.3. Raman spectra for: (a) aggregates of AgNWs and Ag-Au nanocobs; (b) individual AgNWs, intersecting AgNWs, and Ag-Au nanocobs (single spot, 360x360 nm, see spots in Figure 7.4); (c) individual Ag-Au nanocobs measured at 0° and 90° polarization (1 s integration time, 10 accumulations), inset shows actual optical images. (d) UV/Vis absorption spectra of the three pre-formed building blocks and the silver-gold nanocob structure (AgNWs in methanol, all others in chloroform).

UV/Vis extinction spectra of the three pre-formed building blocks, as well as the hierarchical silver-gold nanocob structure in organic solvents demonstrate different

plasmon resonances and their coupling. Silver-gold nanocobs display an extremely wide absorption range from 300 nm to beyond 1000 nm (Figure 7.3d). Gaussian fitting yields the deconvoluted peaks above 300 nm (lower wavelength bands mainly belong to polymer component) at 406 nm, 530 nm, and 740 nm (Figure 7.3d). As-synthesized silver nanowires show two peaks at 350 nm and 380 nm. The peak at 406 nm can therefore be attributed to silver nanowires and coupling between silver core and gold shell (Figure 7.3d). [263, 267, 288] A broad maximum at 530 nm can be attributed to tethered gold nanoparticles (gold nanoparticles show peak at 520 nm). [289] In addition, a very broad maximum covering 600-1000 nm range can be associated with inter-particle and core-particle resonances, strongly dependent upon coupling of gold nanoparticles and core-shell interactions. [290] The overall broad absorption range (effective absorption ranging from 330 nm to beyond 1000 nm) is an important signature of our nanocob structures allowing for effective plasmon excitation not limited to a single wavelength and providing exclusively broad "bandgap" for SERS activation.

Confocal Raman mapping at the highest resolution (360x360 nm spot size) presented at 1580 cm^{-1} clearly show notable differences in SERS signal intensities between conventional silver nanowires and silver-gold nanocobs designed here (Figure 7.4). For silver nanowires functionalized with star polymer, the only noticeable Raman signal is detected at the intersection point of two silver nanowires (twenty-fold enhancement) (Figure 7.4b and spectra at Figure 7.3b, **2**). In contrast, silver-gold nanocobs show very strong Raman scattering exceeding that for original silver nanowires by about two orders of magnitude (Figure 7.4a and spectrum at Figure 7.3b, **1**). The

effect observed here exceeds significantly that reported for conventional silver-gold core-shell one-dimensional structures. Such high Raman intensity makes silver-gold nanocob structures designed here interesting as prospective highly SERS-active markers which can be utilized for large-scale organized SERS arrays for sensitive analyte detection with directional sensitivity, a rarely observed ability. Moreover, our nanocob design of silver nanowires decorated with gold nanoparticles which are separated from silver core with a nanoscale polymer shell composed of both hydrophilic and hydrophobic blocks allows for trapping of guest molecules of different types inside these pre-designed "hot inner shell" making these nanocobs interesting for applications in SERS-based sensor for a wide range of analytes and a broad range of excitations. [291, 292, 293]

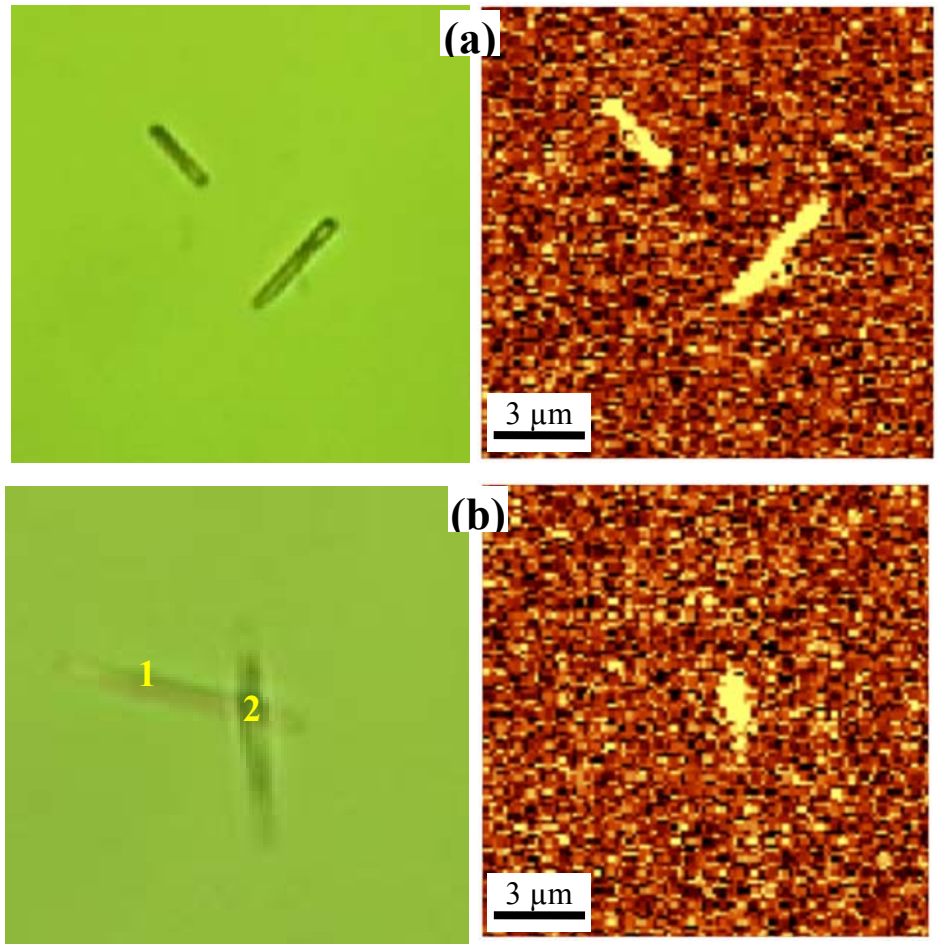

Figure 7.4. Optical images (left) and Raman mapping (right) of individual nanowires: (a) silver-gold nanocobs and (b) silver nanowires modified with star block copolymer at 1580 cm-1 under identical scanning conditions (0.1 sec at each pixel) (see corresponding Raman spectra in Figure 3b).

In summary, using a three-arm $(X\text{-}PEO)_1\text{-}(PS1\text{-}Y)_2$ star polymer linker, spherical gold nanoparticles were assembled onto a silver nanowire surface. We demonstrated that such hybrid, silver-gold nanowires resembling nanocobs, possess significant SERS ability. The SERS enhancement exceeds Raman scattering from isolated silver nanowires by about two orders of magnitude. The effective plasmon excitation provides

a broad absorption band for SERS activation which is also directionally dependent thereby making the nanocobs intriguing for arrayed structures. The intra-particle interactions within a hybrid silver-gold nanowire structure possess significant SERS ability. The effective plasmon excitation provides a broad absorption band for SERS activation which is also directionally dependent thereby making the nanocobs intriguing for arrayed structures.

CHAPTER 8

BIMETALLIC CORE-SHELL NANOSTRUCTURES: GOLD NANOPARTICLES ASSEMBLY ON 1-D AND 2-D SILVER NANOPARTICLES SURFACE

8.1. Introduction

Silver and gold nanoparticles exhibit interesting optical properties such as localized surface plasmon resonances (LSPR) that are tunable with their shape, [294] size, [295] and aggregation, [296] as predicted by theoretical models and well-supported experimentally. [297,298, 299] Oscillating plasmons results in a local electromagnetic field along the nanoparticles surface causing the characteristic Raman bands of organic molecules greatly enhanced, which is the fundamental of surface enhanced Raman spectroscopy (SERS). LSPR within the UV/Vis region occurs when the dimension of the nanostructures is significantly smaller than the wavelength of the exciting electromagnetic radiation, within 5-100 nm. [300, 301, 302, 303] The high Raman enhancement demonstrated by Kneipp *et al* and Nie *et al*, [303] which in turned allow a single-molecule detection, was attributed to a simultaneously operating long-range electromagnetic (EM) and short-range chemical (CHEM) enhancement mechanisms. [304,305] It is now well-established that EM enhancement is best obtained at the interstitial sites between neighboring nanoparticles. [306, 307,308] El-Sayed *et al* investigated the plasmon shift for a series of gold nanodisk dimers separated at various distances between 2-210 nm. [309] Similarly, Lee *et al* showed that changing silver inter-nanowire gap from 35 nm to 10 nm increases the SERS intensity by 200-fold.

Single-molecule detection based on SERS phenomenon by utilizing silver nanoparticles has been demonstrated by Kneip *et al* and Nie *et al*, and later confirmed independently by other groups. [310] For single molecule detection, an enhancement factor within the order of 10^{14}-10^{15} is required. [311] The high enhancement factor demonstrated by Kneip *et al* and Nie *et al* was attributed to a simultaneously operating long-range electromagnetic (EM) and short-range chemical (CHEM) enhancement mechanisms. [312] While the EM mechanism is due to the increased electromagnetic field arising from the nearby oscillating electron on metallic nanoparticles surface, CHEM mechanism is due to the electronic coupling of molecules adsorbed onto the metallic nanoparticles surface. EM is a more superior SER-enhancement mechanism than CHEM; the enhancement factor can reach up to 10^{12} for the former, but only 10-100 for the latter. [313]

It is now well-established that EM enhancement is best obtained at the interstitial sites between neighboring nanoparticles. [314, 315] This is because the oscillating plasmon on one nanoparticle surface couples with its neighbor within the confined junction, thus leading to increased in the local electromagnetic field. The phonon oscillation frequency was found to follow exponential decay with increasing nanoparticles distance. [316] Prashant *et al* investigated the plasmon shift for a series of gold nanodisk dimers (diameter=88 nm and thickness=25 nm) separated at various distances between 2-212 nm. The red-shift in their plasmon absorption peaks implied significant plasmon coupling between the nanoparticles dimer. [317] Significant interaction was observed within 2-27 nm. Similarly, Lee *et al* showed that changing silver inter-nanowire gap from 35 nm to 10 nm increases the SERS intensity by 200-fold.

Exhaustive studies have been undertaken to achieve the optimum SERS enhancement as a function of nanoparticles shapes, [318] compositions, [319] and, configurations [320, 321] both theoretically and experimentally. In terms of geometrical effect, the strongest SERS effect has been determined for nanoparticles having sharp features. [322] Further works were focused towards various designs of hybrid nanostructures that are either metallic alloy nanostructures or organic-inorganic hybrids. Gold nanoparticles assembly on silica nanoparticles substrate, for instance, led to high-surface area of controlled plasmon-plasmon interactions. [323] And the plasmon resonance frequency of the new design of dielectric core-metal shell nanorice is tunable with its respective radius. [324] Other examples include Ag-Au coreshell nanoparticles, [325] gold-silica composite nanoparticle, [326] ensemble of gold droplet on silicon nanowire, [327] silver-nanoparticle-decorated single silver nanowire, [328] and gold-core-paladium-shell nanoparticles. [329] While many studies have been devoted to the design of nanoparticles array, we have previously reported that a silver-gold nanocob hybrid core-shell structure can function as a single nanostructure SER substrate. This is due to particle-particle coupling between the silver nanowire core and the gold nanoparticles shell that result in enhanced localized magnetic field, i.e., SERS enhancement *via* EM mode. The enhancement significantly exceeds that of isolated silver nanowires by two-orders of magnitude. [330] In addition, the one-dimensional nanocob structure exhibits anisotropy; the SERS enhancement is strongest when a polarized excitation laser is perpendicular to the direction of the individual nanocob structure. In this design, the gold nanoparticles were assembled onto the surface of silver nanowires by a combination of estertification

and click-chemistry. A well-defined three-arm $(X\text{-}PEO)_1\text{-}(PS\text{-}Y)_2$ star polymer linker was utilized as the organic linker. The organic polymer component links the two metallic nanoparticles together within which intra-particle electromagnetic SERS enhancement is active.

Herein, we report an alternative approach towards a hierarchical assembly of gold nanoparticles by electrostatic interactions. Electrostatics assembly is facile because it can be done at room temperature and applicable to a wide range of applications, also known as layer-by-layer assembly approach. [331, 332] In contrast to the covalent approach, electrostatics interaction exists only within a certain range of pH. In this way, electrostatics assembly approach maybe reversible. Moreover, the polyelectrolyte component is capable of trapping analytes [333] for the previously proposed single nanoparticle SERS-substrate application. Secondly, we demonstrate that this method can be extended to a two-dimensional silver nanoplates core.

8.2. Attaching gold nanoparticles onto silver nanowires and silver nanoplates by electrostatics

A certain amount of the methanolic solution of silver nanowires can be easily isolated from its solution by brief centrifugation at 3,300 rpm for less than five minutes. On the other hand, silver nanoplates required centrifugation at 5,500 rpm for 20 minutes to completely isolate from its solution. Following the centrifugation in pre-weighed centrifuge tubes the transparent supernatant is pipetted out, and the silver nanoparticles residue is dried in vacuum to remove excess of solvents. In this way, the silver

nanoparticles solution concentration could be determined. A typical concentration used for the subsequent procedure is 1-3 mg/mL.

The gold nanoparticles densities on silver nanoparticles substrates are varied as follows. To obtain a low-density gold nanoparticles, 0.1 mL solution of the as-prepared Au:DMAP solution is diluted in a 2.4 mL nanopure water (pH 7, $2x10^{-3}$ M phosphate buffer). Next, this solution mixture is added dropwise into a stirring solution of 2.5 mL of negatively-charged silver nanoparticles (1 mg/mL concentration, pH 7, $2x10^{-3}$ phosphate buffer). The solution mixture is sonicated for 30 seconds and vortexed for 2 minutes to ensure uniform gold nanoparticles attachment onto the silver nanoparticles surface. Excess of unattached gold nanoparticles are then removed by centrifugation (3,300 rpm, 5 minutes). The silver-gold nanoparticles residue is then redispersed in a PAA solution (2 mg/mL, 0.01M phosphate buffer) with the aid of brief sonication and vortexing (0.5 mg/mL concentration). Excess of unattached PAA is removed with multiple centrifugation and redispersion cycle in nanopure water. This is to coat the outer shell with PAA (Scheme 8.1). Otherwise, the silver-gold nanoparticles are not-dispersible in water. For a high-density gold nanoparticles, 0.5 mL solution of the as-prepared Au:DMAP solution is used instead for the same amount of silver nanoparticles. Correspondingly, fivefold phosphate buffer concentration is used.

8.3. Results and Discussions

8.3.1 Nanoparticles building blocks

Figure 8.1 shows TEM images of the bimetallic core-shell nanoparticle building blocks, one-dimensional silver nanowires (AgNWs) and two-dimensional silver nanoplates (AgNPls) core components, and spherical gold nanoparticles (AuNPs) shell component. The lengths of AgNWs are on average, L=6±2 μm and diameter, D=75±20 nm (aspect ratio, A.R.=80). The average height of AgNPls is 30±10 nm, which exhibits a bimodal widths distribution, 190 ± 60 nm and 470 ± 60 nm. The diameter of spherical AuNPs is, D= 4.1±1 nm.

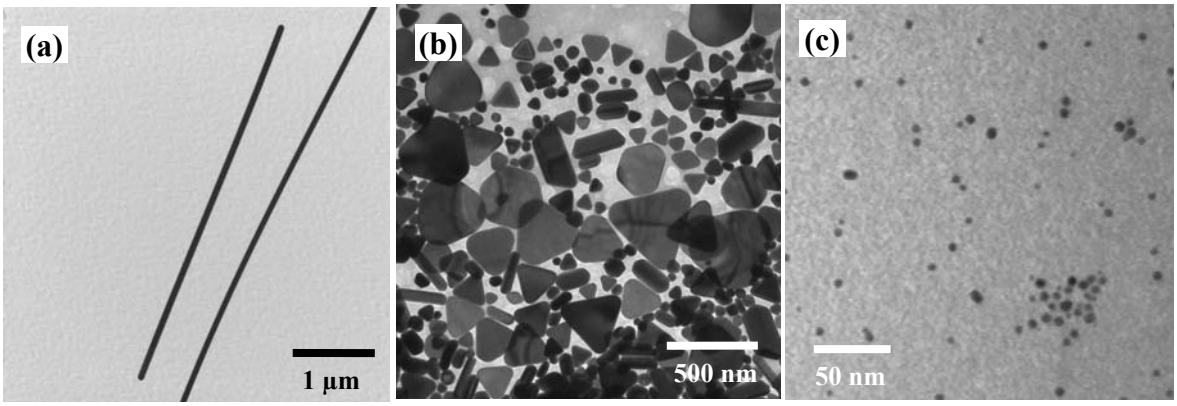

Figure 8.1. TEM images of as-synthesized: (a) silver nanowires, AgNWs:PVP, (b) silver nanoplates, AgNPls; and (c) 4-DMAP functionalized spherical gold nanoparticles, Au:DMAP.

8.3.2. Absorption spectra of building blocks nanoparticles

The UV-Vis absorption spectra were obtained for each of the purified nanoparticle building blocks in solution state (Figure 8.2). A characteristic double-peak spectrum is seen for AgNWs (Figure 8.2a). The shoulder peak at 350 nm is due to the quadrupole resonance excitation of nanowires. The other peak at 393 nm is due to transverse plasmon resonance of nanowires, which is proportional to its diameter.

According to the linear relations between absorbance maximum and nanowire diameter which is given by $\lambda_{max} = 361.3 + 0.41\ D_{nanowire}$, this peak position corresponds to 77.3 nm diameter. [334] This equation was derived from AgNWs with diameters in the range of 70-450 nm. The positive slope in the equation means that increasing nanowire diameter is accompanied by red-shift in the maximum peak absorbance. The longitudinal plasmon peak is not seen within 200-1,000 nm range because of the high aspect-ratio nanowires, [335] which is in the microns range.

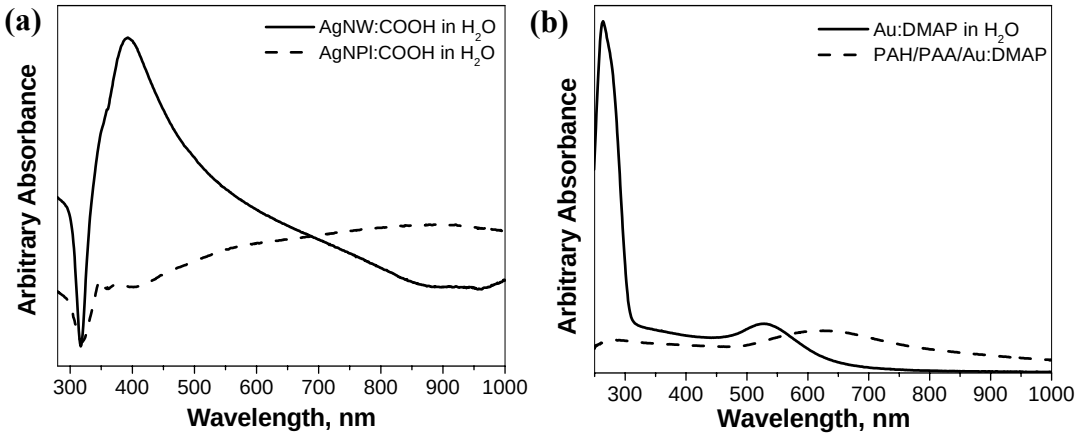

Figure 8.2. UV-Vis absorption spectra of: (a) AgNWs: PVP and AgNPls: PVP core, and (b) Au:DMAP.

AgNPls exhibit the similar double-peak resonance spectrum with AgNWs (Figure 8.2a), with the addition of a broad peak that peaks at 890 nm. Due to its two-dimensional shape, silver nanoplates can have in-plane and out-of plane dipole and quadrupole resonances. The peak at 350 nm can be assigned to a weak dipole out-of-plane resonance and the peak at 377 is assigned to a weak quadrupole out-of-plane resonance (Figure 8.1a). [294, 336] Due to the wide distribution in nanoplates nanoplate dimension and shape,

the in-plane- and out-of-plane dipole, and in-plane quadrupole resonances give rise to the broad halo between 300-1000 nm; the dipolar in-plane resonance mode red-shifts with increasing nanodisk diameter.

For the 4-dimethylamino pyridine modified gold nanoparticles, Au: DMAP (Figure 8.2c), two prominent peaks are seen. The first peak at 264 nm is indicative of the pyridinium ring from 4-DMAP molecule and the other peak at 530 nm belongs to the dipole Plasmon resonance energy of the spherical gold nanoparticles.

8.3.3. Absorption peaks of shell nanoparticles in the solid state

To understand the plasmon absorption shift for Au:DMAP in the solid-aggregated state, the aqueous solution of Au:DMAP is dropcasted onto poly(allylamine hydrochloride)/poly(acrylic acid) (PAH/PAA) layer. The absorption spectrum of PAH/PAA/Au:DMAP in its film state reveals only a single peak at 623 nm (Figure 8.1). Since this value is within the range of interacting gold nanoparticles, [337] a conduction channel between neighboring nanoparticles is probably absent. [315, 338] The absence of a peak within the 530 nm region implies that all of the gold nanoparticles are strongly interacting, and within a similar distance. [339] AFM topographical image reveals that the adsorbed gold nanoparticles appear to be uniform, but occasional aggregates are seen (Figure 8.3). A scratch was made to directly determine the thickness of the adsorbed gold nanoparticles film. The heights of the occasional aggregates reach up to 45 nm, and the surrounding film thickness of gold are within 10 nm. Considering that the underlying PAH/PAA film has a certain thickness that maybe up to 5 nm, [340] the surrounding layer

can be said to be a mono- and bi-layer of gold nanoparticles. The average diameter of these nanoparticles was previously measured directly from its TEM image to be 4.1 $\pm$ 0.5 nm.

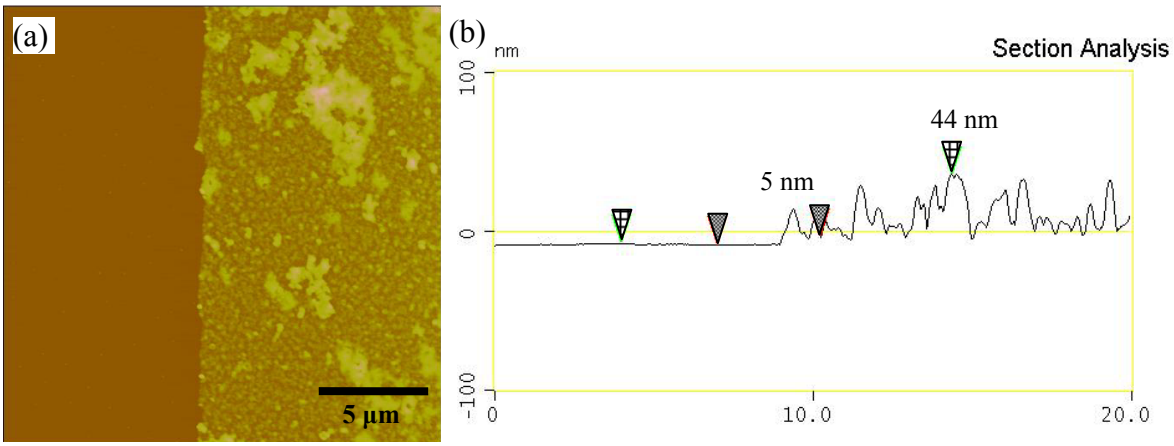

Figure 8.3. AFM topography of scratched films of Au:DMAP with its corresponding cross-sectional analysis.

8.3.4. Absorption spectra of silver core-gold nanoparticles shell hybrid nanostructures

Scheme 8.1 illustrates the multi-step assembly of positively-charged shell nanoparticles (Au:DMAP) onto the negatively-charged one-dimensional silver nanowires or the negatively-charged two-dimensional silver nanoplates. In the final step, the hybrid nanostructures are coated with PAA to stabilize them in solutions. Without this outer coating the hybrid nanostructures tend to form irreversible aggregates that are not dispersible in solution. The final products are thus abbreviated as Ag/Aun/PAA, where Ag represents silver nanowire (AgNW) or silver nanoplate (AgNPl) and n refers to the relative concentration of gold nanoparticles used in the preparation of the silver-gold hybrid nanostructures, where n=1 or 5 (more on this below). The final product is

dispersible in methanol or water when subjected to sonication and vortexing, but precipitate out of solution within five minutes.

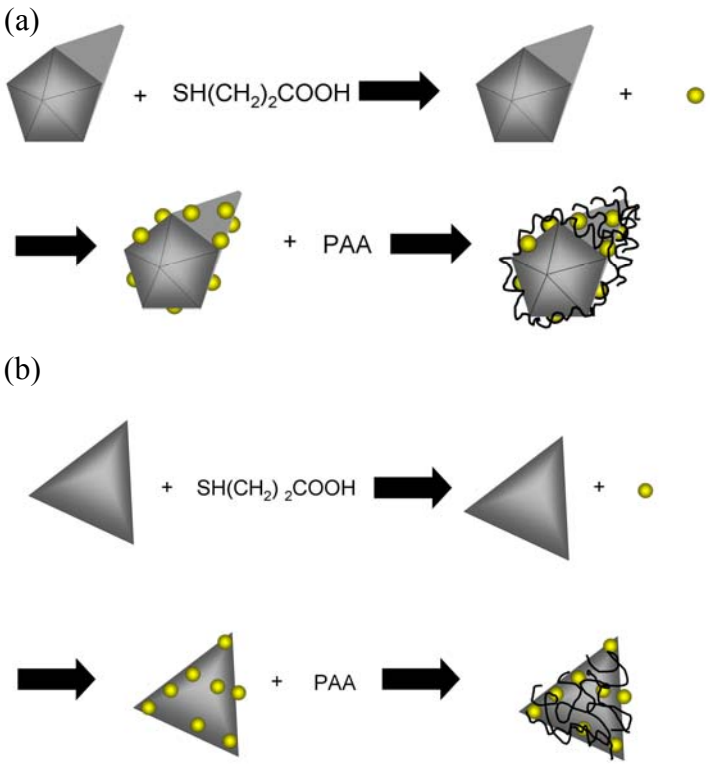

Scheme 8.1. Gold nanoparticles assembly onto silver nanowires surface: (a) AgNW/Au/PAA and (b) AgNPl/ Au/PAA.

Figure 8.4 and Figure 8.5 show the UV/Vis absorption spectra of the silver nanoparticles as they undergo several modification steps. Surface modification with 3-mercaptopropanoic acid causes the quadrupole peak to blue-shift in the case of silver nanowires, from 393 nm to 388 nm (Figure 2a). Furthermore, the peak intensity difference between the bulk resonance and the quadrupole resonance decreases. Likewise, the quadrupole resonance peak of silver nanoplates blue-shifts following the

ligand exchange procedure. It shifts from 376 nm to 366 nm. Upon the introduction of gold nanoparticles, the formed silver-gold hybrid nanostructures exhibit a combined resonance spectrum (compare Figure 8.2 with Figure 8.3), as previously reported for the hybrid silver-gold nanocobs. [330] Moreover, as seen from the relative absorption intensity due to gold nanoparticles, control of gold nanoparticles density on silver nanoparticles surface is achieved by varying the concentration of positively-charged gold nanoparticles solution (Figure 8.3). This is further confirmed from AFM and TEM images (compare Figure 8.3 with Figure S2).

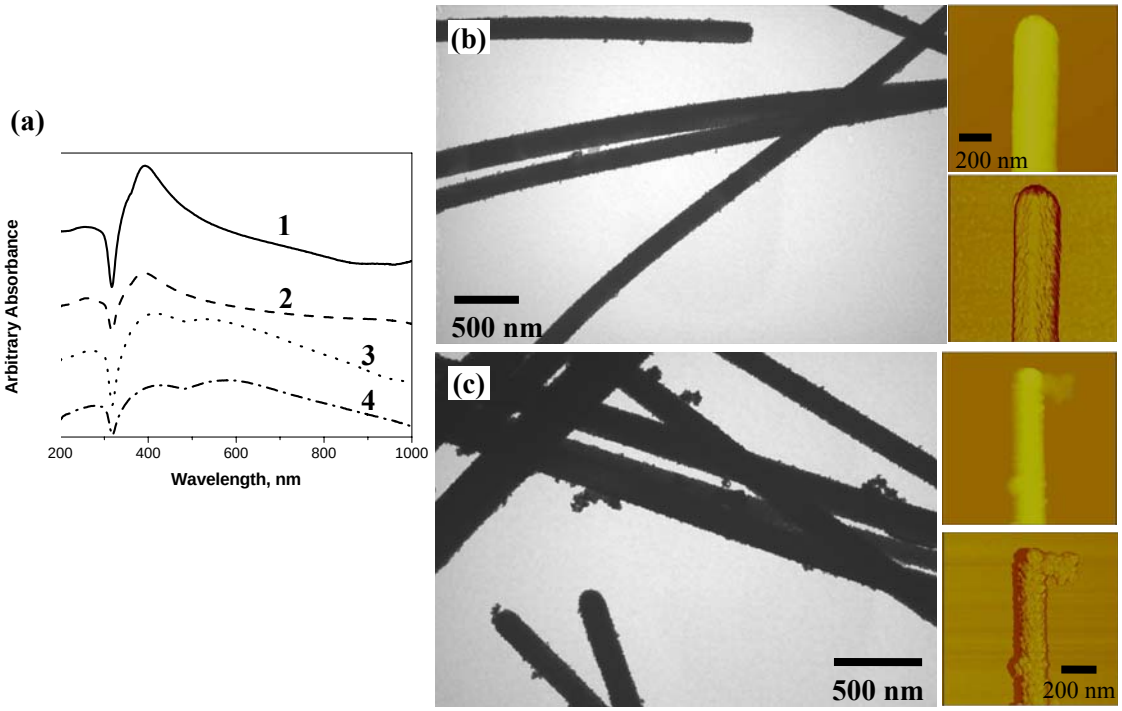

Figure 8.4. UV-Vis absorption spectra of: (a) 1. AgNWs: PVP, 2. AgNWs: COOH, 3. AgNW/Au1/PAA, 4. AgNW/Au5/PAA. (b and c) The corresponding TEM and AFM images. Top right is height (z = 200 nm) and bottom right is phase image. Note that the baseline of each spectrum has been offset for easy comparison.

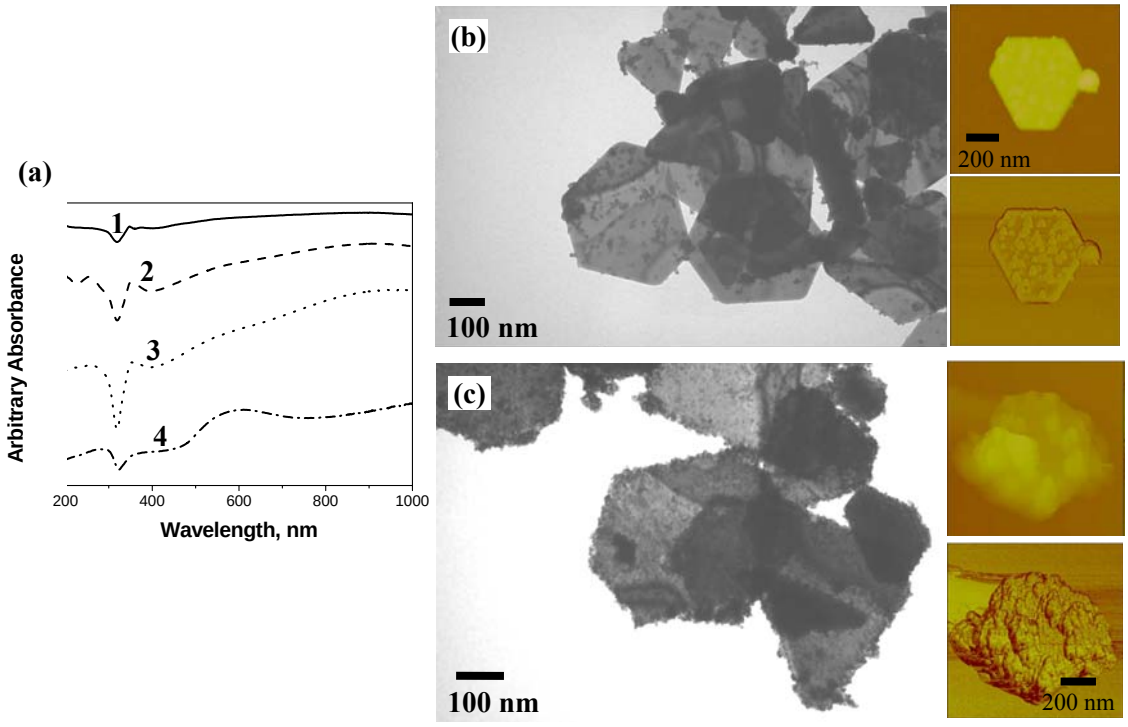

Figure 8.5. UV-Vis absorption spectra of: (a) 1. AgNPls: PVP, 2. AgNPls: COOH, 3. AgNPl/Au1/PAA, 4. AgNPl/Au5/PAA and (b and c) the corresponding TEM and AFM images. Top right is height (z = 200 nm) and bottom right is phase image. Note that the baseline of each spectrum has been offset for easy comparison.

The amount of shift in the absorption peak due to gold nanoparticles can give hints about the nanoparticles interactions. For AgNW/Au1/PAA this peak occurs at 536 nm, which is only a slight red-shift from 530 nm (Figure 8.4a). In this case, AFM and TEM images show an extremely sparse distribution of gold nanoparticles (Figure 8.4b). Therefore, it can be said that the red-shift is mainly due to gold-silver interaction and little from gold nanoparticle-to-gold nanoparticle interactions. Further red-shift in the gold nanoparticles absorption peak is seen for AgNW/Au5/PAA (Figure 8.4a). The value

occurs at 583 nm. This implies significant interactions between the gold nanoparticles, which is in agreement with the obtained AFM and TEM images (Figure 8.4c). Nonetheless, the nanoparticles density may not be as much as it is in the film state as discussed earlier. In the film state, the absorbance peak occurs at 623 nm. Likewise, the transversal plasmon resonance peak from silver nanowires red-shifts from 393 to 416 nm for AgNW/Au1/PAA and from 393 to 428 nm for AgNW/Au5/PAA. The gold nanoparticles absorption peak is not immediately discernible for AgNPl/Au1/PAA, and it occurs at 590 nm for AgNPl/Au5/PAA (Figure 8.5a). AFM and TEM images confirm the gold nanoparticles distribution for AgNPl/Au1/PAA and AgNPl/Au5/PAA (compare Figure 8.5a with Figure 8.5b).

To further understand the plasmon interaction between the gold nanoparticles with silver nanowire, UV/Vis measurement of individual silver-gold nanowires on a quartz substrate was performed (Figure 8.6). Under such experimental condition, the overall shape of UV/Vis absorption spectrum of randomly oriented array of AgNW/Au1/PAA is comparable with that in solution state (Figure 8.6a). The characteristic peaks belonging to silver and gold nanoparticles occur at 421 nm, and 531 nm and 760 nm, respectively. In this case, the quadrupole resonance peak is absent and the transverse plasmon peak has shifted significantly from 393 nm as a result of interaction between nanowires due to aggregation and difference in dielectric environment. The plasmon peak due to gold at 531 nm is consistent with non-interacting state, whereas the plasmon peak at 760 nm suggests nanoparticle-to-nanoparticle plasmon coupling. For the higher density gold nanoparticles, AgNW/Au5/PAA, the plasmon

peaks due to gold nanoparticles is more red-shifted at 571 nm and 725 nm (Figure 8.6d). This is consistent with increased nanoparticle-to-nanoparticle plasmon coupling (Figure 8.2b).

UV/Vis measurement of a single silver-gold nanowire with polarized light reveals significant difference in the short- and the long-axis (Figure 8.6 b&c and Figure 8.6 e&f for AgNW/Aun/PAA, n=1 and n=5, respectively). [341] For AgNW/Au1/PAA nanostructure the transversal LSPR due to silver nanowire is strongly excited at 424 nm accompanied by the resonance peak due to gold nanoparticles at 585 nm (Figure 8.6b). However, only absorption due to gold nanoparticle LSPR is seen when the excitation light is polarized along the long-axis (broad maximum at around 618 nm and 767 nm) (Figure 8.6c). Compared with the solution case this value is much red-shifted and can be attributed to localized aggregation in the form of dimers and trimers that becomes significant in a dry state. Similar trend is seen for AgNW/Au5/PAA, except that in this case the plasmon coupling between gold nanoparticles is more significant due to the higher gold nanoparticles density (Figure 8.6 e&f). This is seen from the more significant red-shift in the gold nanoparticle LSPR, λ_{max} = 624 nm and 787 nm when the light excitation is polarized along the long-axis (Figure 8.6f).

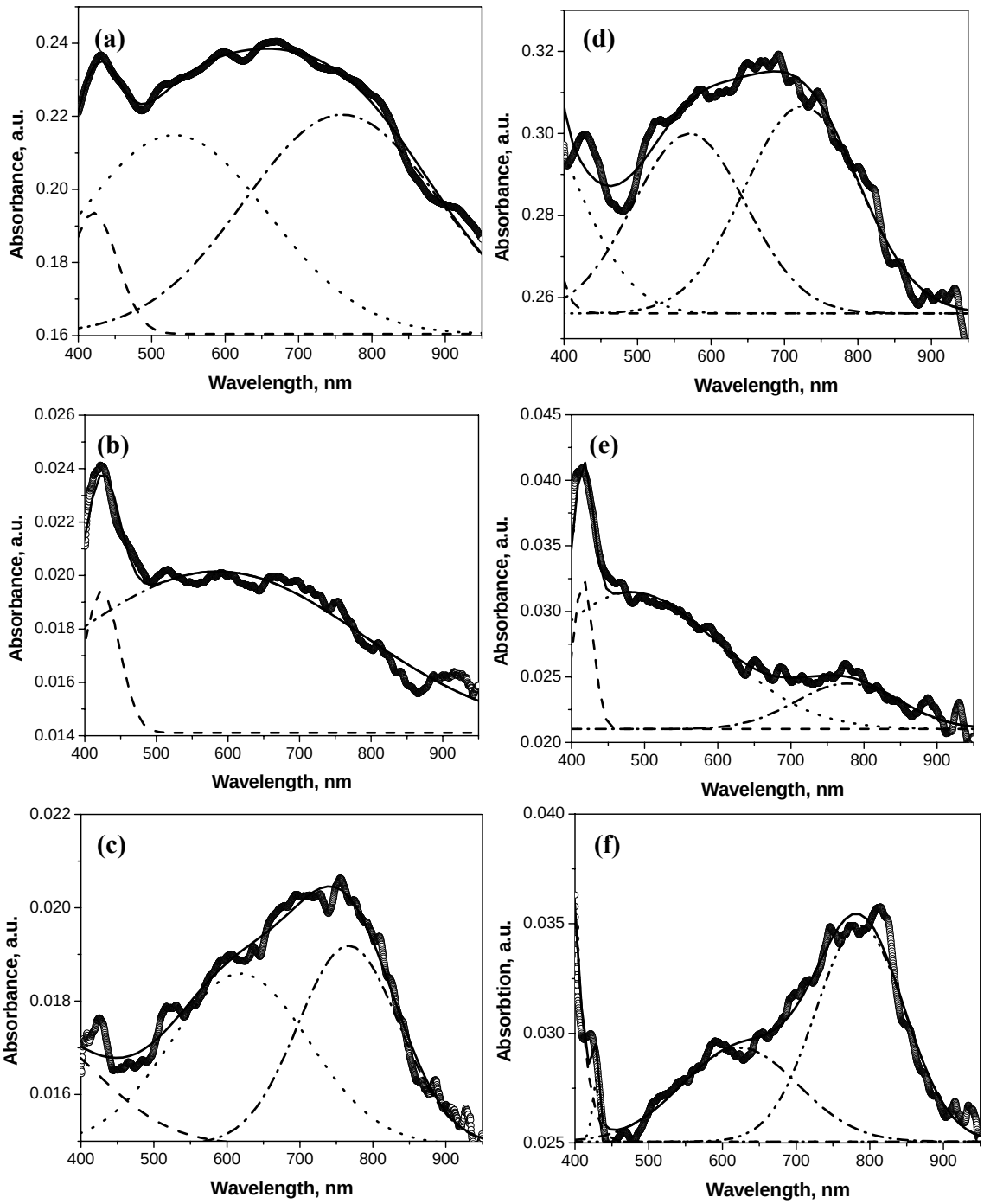

Figure 8.6. UV/Vis Absorption spectra of: randomly oriented array of (a) AgNW/Au1/PAA and (d) AgNW/Au5/PAA and a single nanowire measured with polarized light along the short- and long-axis for (b and c) AgNW/Au1/PAA and (e and f) AgNW/Au5/PAA.

8.3.5. SERS effect due to silver-gold Ag/Aun/PAA core-shell nanoparticles

Solutions of Ag/Aun/PAA were dropcasted onto a series of cleaned silicon wafer and incubated in different concentrations of aqueous Rh6G solutions (10^{-12}-10^{-4} M). We have selected Rh6G as the model analyte because its SERS property is widely reported in literatures. The peak assignment of Rh6G adsorbed on colloidal silver has been described in detailed by Hildenbrandt *et al* and will not be discussed any further here: [342] 614 cm^{-1} (C-C-C ring in-plane bending); 774 cm^{-1} (C-H in-plane bending); 1,129 cm^{-1} (C-H in-plane bending), 1,183 cm^{-1}; 1,310 cm^{-1}, 1,363 cm^{-1}, 1,509 cm^{-1}, 1,572 cm^{-1}, and 1,648 cm^{-1} (aromatic C-C stretching). The relative enhancement factor will be determined throughout from the intensity band at 1,648 cm^{-1}. Raman mappings were performed on each sample, between 1,630 and 1,680 cm^{-1}. A plot of Rh6G concentration versus Raman intensity is obtained. When silver nanowire is used as the core, laser polarization with respect to nanowire orientation is noted. We performed two independent measurements, in one case the laser polarization is perpendicular to and in another case the laser polarization is parallel to the nanowire orientation as seen in (Figure 8.7a and Figure 8.7b). The enhancement is stronger when it is oriented perpendicular to the laser polarization, as previously reported for silver-gold nanocob as well as other one-dimensional SER-substrates. [343, 344, 345, 346] Similarly, the Raman enhancement increases with increasing gold nanoparticles density. When it is oriented perpendicular to laser polarization, AgNW/Au5/PAA could detect the presence of Rh6G down to 10^{-8} M. On the other hand, AgNW/Au1/PAA could only detect down to 10^{-7} M concentration, one order of magnitude lower (Figure 8.8a and Figure 8.8b). This

difference could be attributed to the active transverse plasmon resonance of silver nanowire coupling with the nearby spherical nanoparticles to give enhanced electromagnetic field when the laser polarization is perpendicular to it as discussed earlier (Figure 8.8d). If the laser polarization is parallel to silver nanowire orientation coupling between the spherical gold nanoparticles is dominant.

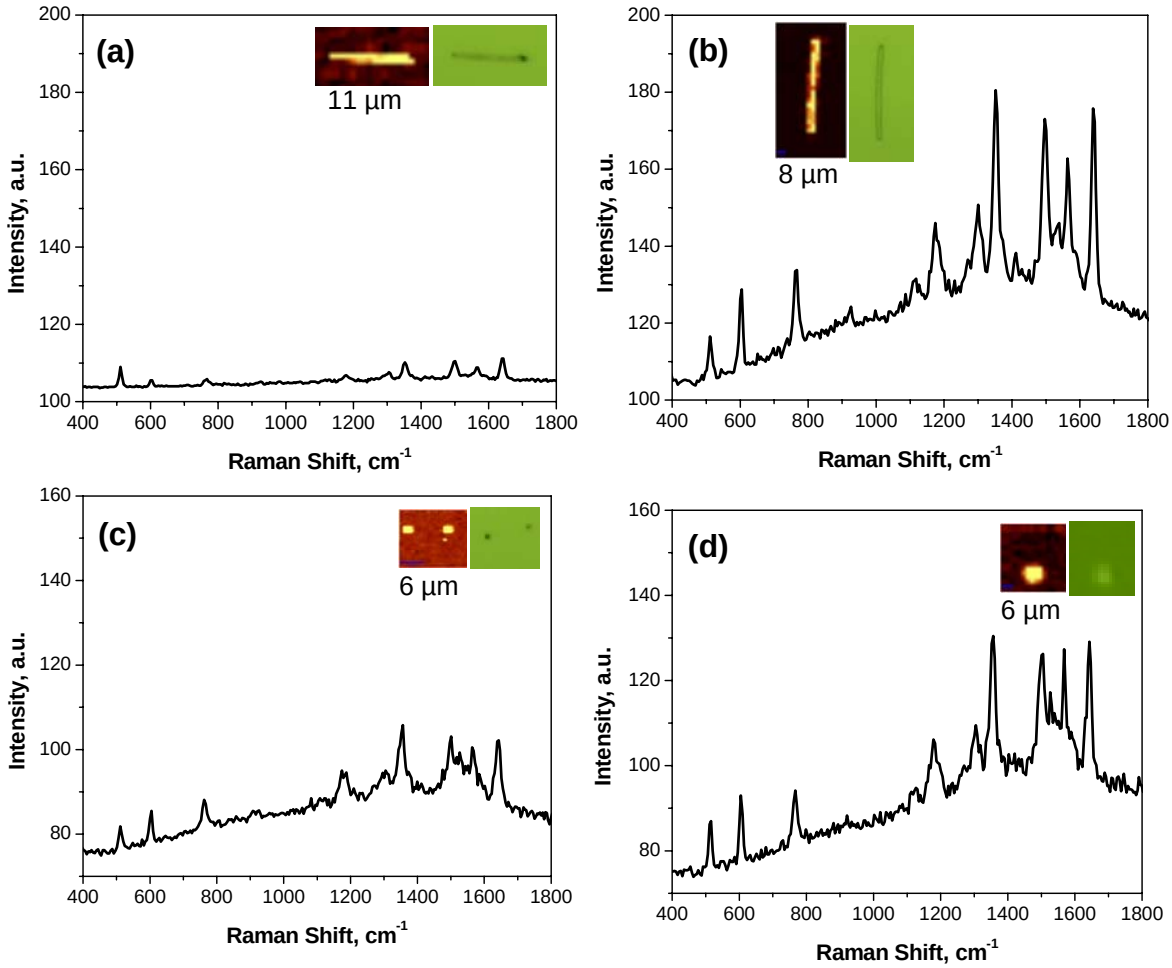

Figure 8.7. SERS spectra of Rh6G on: (a) AgNW/Au5/PAA with laser polarized parallel and (b) perpendicular to nanowire orientation and (c and d) AgNPl/Aun/PAA for n=1 and n=5, respectively. Insets are Raman Intensity mapping within 1,630-1,680 cm^{-1}, which corresponds to aromatic C-C stretching.

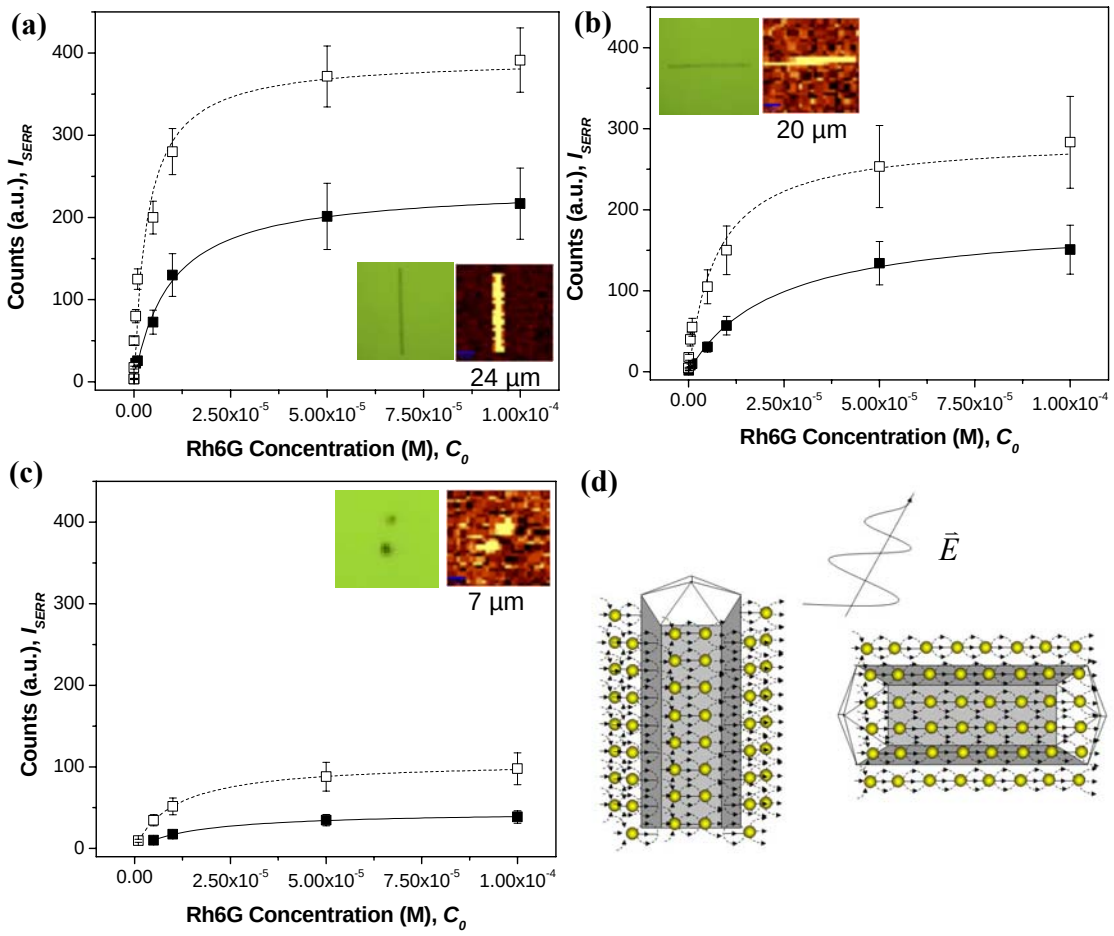

Figure 8.8. Plot of Raman Intensity, I_{SERR}, versus Rhodamine 6G concentration, C_0, for: (a and b) AgNW/Aun/PAA and (c) AgNPl/Aun/PAA. Laser polarization is (a) perpendicular to and (b) parallel to nanowire orientation, respectively. Insets are representative (left) brightfield image and (right) Raman map within 1,630 and 1,680 cm^{-1} at the saturation concentration. Dotted line represents n=1 curve and solid line represents n=5 curve. (d) Induced electromagnetic field within silver nanowires decorated with spherical gold nanoparticles in the presence of exciting laser that is polarized in the horizontal direction.

The minimum detection limit for AgNPl/Aun/PAA is two orders of magnitudes lower than it is for AgNW/Aun/PAA (Figure 8.8c), down to $5x10^{-6}$ M for the low- and 10^{-6} M for the high-density of gold nanoparticles. Again, we noticed a gold-nanoparticle density-dependent on the Raman intensity of AgNPl/Aun/PAA (Figure 8.8c). The lower performance seen for AgNPl core compared with AgNW core is in agreement with Zhang *et al* on their study on the SERS performance of silver colloids of different shapes. In terms of EM effect, silver nanoplates geometry is dominated by its two-dimensional feature that sits parallel to the substrate, in contrast to the pentagonal cross-section silver nanowire which has sharp features that function as "hot sites". In addition, the maximum plasmon absorption of silver nanowires coincides more closely with the excitation laser (λ_{exc}=514 nm) than it is for the silver nanoplates (Figure 8.2a). In terms of CHEM effect, they correlate the analyte absorption to the crystalline facets exposed on the crystals, that is, more facets are exposed for AgNWs than it is for AgNPls, thus allowing greater analyte absorption leading to CHEM mode of Raman enhancement.

The plot of Raman intensity with respect to Rh6G concentration can be fitted according to the Langmuir's adsorption isotherm equation. A least-square regression fit was done on Origin software which required it to be re-arranged in its implicit form, where c_0 being the dependent variable and I_{SERR} the independent variable (see Equation 1). [347] This equation was previously derived by Hildebrandt *et al* to describe Raman enhancement of Rh6G adsorbed onto colloidal silver that is dispersed in a certain Rh6G concentration, c_0. $K_{s,max}$ is saturation concentration, at which the value of I_{SERR} reaches a maximum and A is an arbitrary constant. The obtained value of ω_s can be used to

estimate the adsorption energy, G_{ad}, (Equation 2) which is found to be within 37-42 kJ/mol for AgNW/Aun/PAA (n = 1 and 5), indicating a strong affinity of Rh6G molecules with the surface. In the equation R is gas constant and c_{H_2O} is molarity of water (55.346 mol/L). [263, 346] The corresponding threshold concentration is within $1x10^{-6}$ M -$5x10^{-6}$ M.

$$c_0 = \frac{\omega_s . I_{SERR}{}^2 - I_{SERR} . A - K_{s,\max} . \omega_s . A . I_{SERR}}{[\omega_s . A . (I_{SERR} - KA)]} \qquad (Equation\ 1)$$

$$G_{ad} = -RT \ln(c_{H_2O}) \qquad (Equation\ 2)$$

Since the maximum absorption of Rh6G is in the 520 nm range and it is strongly fluorescent, Raman measurement with 514 nm excitation laser is not possible. To further quantify the performance of our single hybrid nanoparticle SERS substrate, they were compared with dense array of silver nanowires [263] and silver nanoplates prepared by Langmuir-Blodgett technique. Despite a large area of highly-ordered and densely-packed monolayer of silver nanoparticles, defects in the form of aggregates or multi-layers were occasionally seen (Figure 8.9a inset and Figure 8.9c inset). The monolayer films were incubated in 10^{-4} M (saturation concentration) Rh6G for 10 minutes and Raman mapping within 1,630-1,680 cm^{-1} was obtained (Figure S5b and Figure S5d). The Raman mappings show sporadic SERS "hot-spots" at the nanoparticles junctions (<10 nm) for silver nanowires [348] and likewise for silver nanoplates where the "hot spots" appear in the aggregated regions or interacting nanoplates. This is contrary to the silver-gold hybrid nanoparticle which uniformly enhances Raman throughout its nanowires or nanoplates

surface. Taking the average intensity across the whole area of Raman map of several locations, under identical conditions the best performing AgNW/Au5/PAA SER-substrate is on par with the dense silver nanowire or silver nanoplates array. The Rh6G intensity is only twenty-fold better for silver nanowires array and it is only five-fold better for silver nanoplates array. Tao *et al* previously estimated that 1-hexadecanethiol functionalized silver nanowires array exhibit an enhancement factor, EF= $2x10^9$. [263]

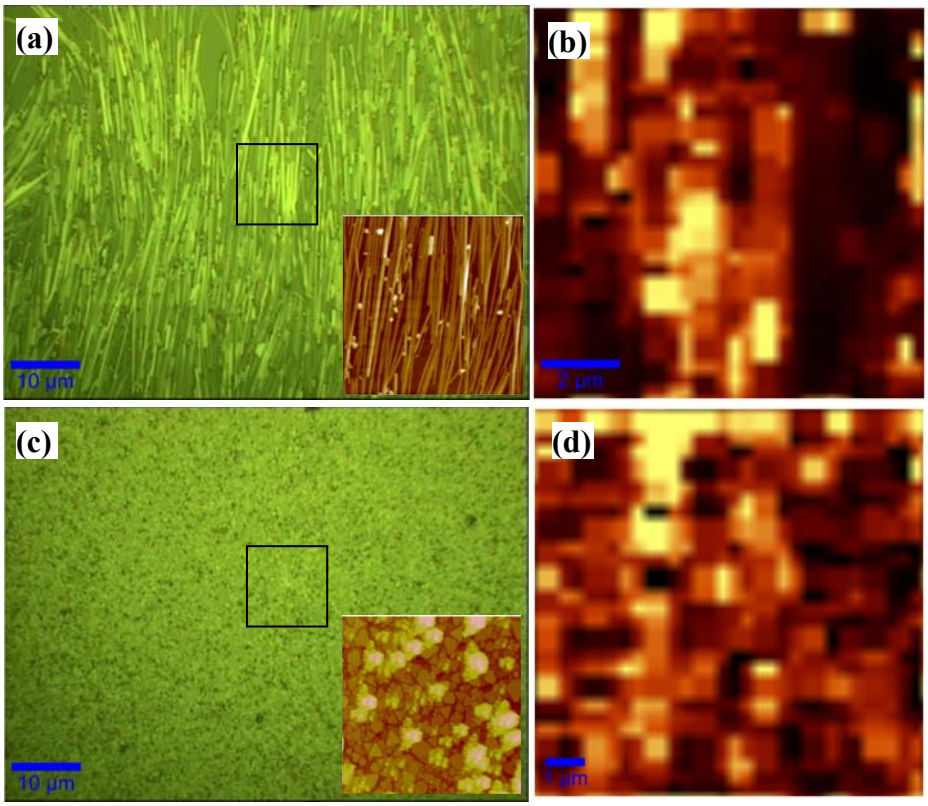

Figure 8.9. Brightfield images of silver nanowires and silver nanoplates array with their corresponding Raman map within 1,630-1,680 cm^{-1} after 10 minutes incubation in 10^{-4} M Rh6G solution (b and d). a and c insets are the corresponding AFM images (z=300 nm). Scan area is 20x20 μm^2 and 5x5 μm^2, respectively.

8.3.6. SERS effect due to bare silver nanoparticles core and gold nanoparticles shell

To compare the SERS performance of the hybrid nanostructure, the initial components of the hybrid nanostructures were also drop-casted onto a silicon wafer and incubated in various concentrations of Rh6G solutions. Raman mapping within 1,630-1,680 cm^{-1} region reveals no discernible Raman signal from the individual AgNW:COOH and AgNPl:COOH nanoparticles due to Rh6G after ten minutes incubation in Rh6G solution below $c_0 < 10^{-4}$ M (not shown). Likewise for PAH/PAA/Au:DMAP SER-substrate within the monolayer region (Figure 8.10). Nevertheless, the gold nanoparticles aggregate is capable of detecting the presence of Rh6G solution down to 10^{-6} M concentration. This value is equivalent with silver nanoplate-gold nanoparticles hybrid. However, it should be noted that in the case of silver-nanoplate-gold nanoparticles hybrid the gold nanoparticles form a monolayer on silver nanoplate substrate (Figure 8.4 and Figure 8.5), in contrast to the multi-layered gold nanoparticles aggregates that are up to 45 nm high (Figure 8.10).

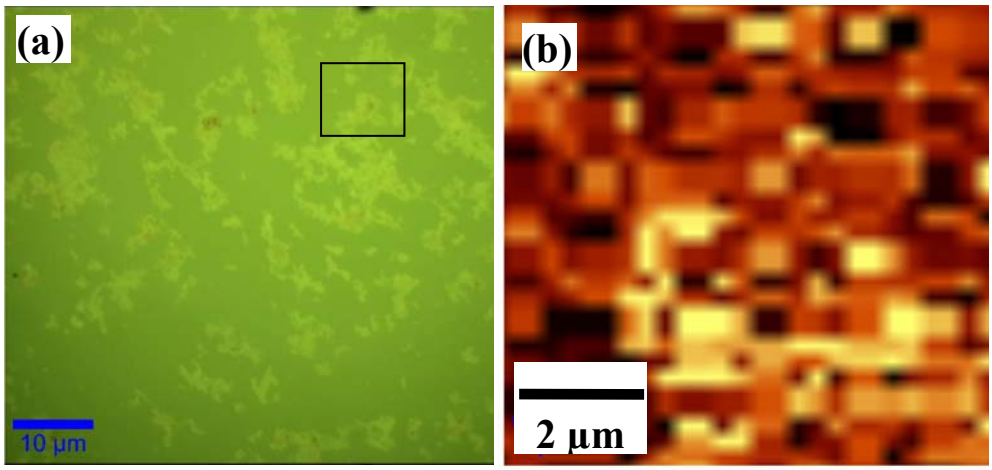

Figure 8.10. Images of Au:DMAP adsorbed onto PAH/PAA polyelectrolytes LbL: (a) brightfield image and (b) Raman map within within 1,630-1,680 cm^{-1}.

In conclusions, facile wet-assembly approach of nanosized particles onto one- and two-dimensional submicron nanoparticles substrates has been demonstrated. The result is a core-shell hybrid nanostructure having a synergistic optical property. Gold nanoparticles were assembled onto the 1-D silver nanowires and 2-D silver nanoplates at variable density. Such bimetallic core-shell hybrid nanostructure is capable of trapping analyte within the polyelectrolyte matrix, thus subjecting the absorbed analyte to an amplified electromagnetic field to give rise to enhancement in its characteristic Raman vibrations. Polarization dependence behavior is also evident when silver nanowire is used as the core particle. We found that silver nanowire-gold nanoparticles outperforms silver-nanoplate-gold nanoparticles hybrid nanoparticle by two orders of magnitude in their ability to detect Rh6G molecules in solution. And finally, under identical experimental condition the Raman signal due to Rh6G silver nanowire array performs twenty-fold better and silver nanoplates array five-fold better than single-nanoparticle

AgNW/Au5/PAA. Judicious selection of shell nanoparticles can lead to a design of SER-substrate that is comparable or better than silver nanowire array and is currently under investigation. A successful design of a single nanoparticle SERS-substrate based on wet-assembly technique proposed here can lead to a compact, low-cost, and label-free means of chemical detection.

CHAPTER 9

GENERAL DISCUSSION AND CONCLUSIONS

This work has demonstrated a successful bottom-up assembly of some representative geometrically-defined inorganic building blocks with the aid of functional-group bearing organic molecules. To this end, (1) ultra-thin LbL nanocomposite film and (2) silver-gold hybrid nanostructures were assembled from these building blocks by either covalent or ionic interactions. The silver and gold inorganic blocks is mainly responsible for the overall property of the hybrid structure, "bricks" component, and the organic block serves as the "mortar" component to give synergystic optical, mechanical, and electrical properties; and, more importantly, the resulting organic/inorganic structures have practical handability for further manipulations or incorporation into microfabricated platforms.

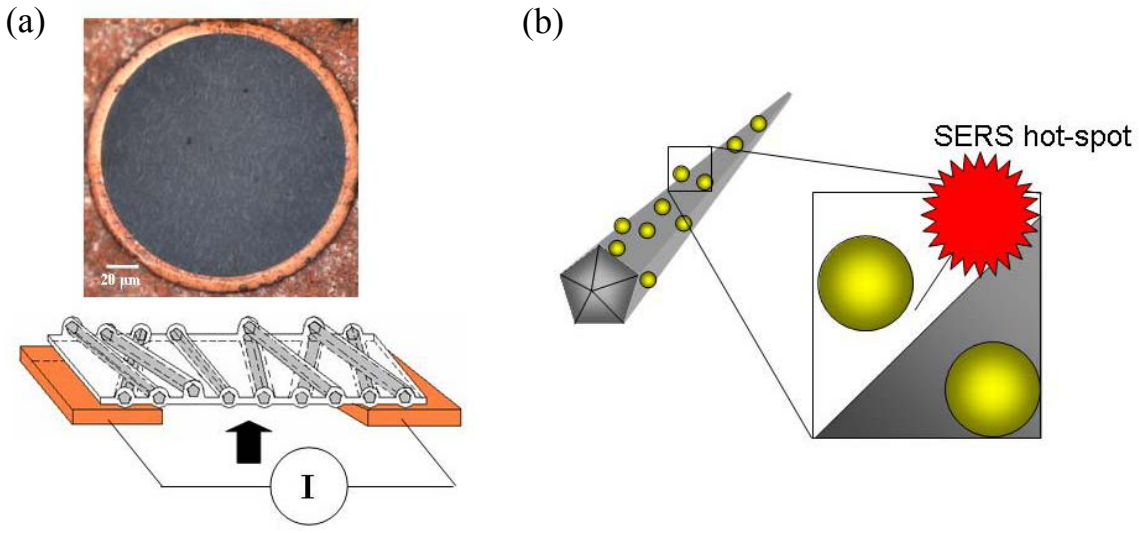

Figure 9.1. (a) Ultra-thin composite film-based sensor and (b) single nanoparticle SERS-based chemical sensor.

Two potential applications have been explored as a result of this study: (a) ultra-thin nanocomposite film-based sensor and (b) single nanoparticle SERS-based chemical sensor (Figure 9.1). Respectively, the design of the novel organic/inorganic hybrid nanostructures presented here can be categorized into two major classes:

1. Silver-nanowire reinforced LbL film for a film-based pressure sensor application: We have demonstrated the fabrication of a robust, nanometer-thin silver nanowires reinforced ultrathin composite films (thickness < 100 nm) with tailored mechanical properties and can exhibit electrical conductivity. The silver nanowires are well-dispersed within the composite film to give a uniform and strongly improved mechanical property. The composite films are robust and can be easily transferred onto various substrates, which is necessary for their characterizations. We have also shown that the one-dimensional silver nanowire "filler" can be incorporated either as a random-network or as a unidirectionally aligned array. The former design results in a mechanically isotropic film and the latter design results in a mechanically anisotropic nanofilm caused by the silver nanowires orientation.

To achieve the former design, a series of free-standing layer-by-layer (LbL) films with encapsulated silver nanowires was fabricated at controlled volume fractions, ϕ = 2.5 - 22.5%. Silver nanowires were sandwiched between $(PAH/PSS)_{10}$ films resulting in a mechanically isotropic nanocomposite structures with a general formula $(PAH/PSS)_{10}$ Ag $(PAH/PSS)_{10}$. The ultra-thin composite film (<100 nm thick) was found to exhibit a

greatly improved mechanical property than a pristine LbL film. The Young's modulus is improved up to three-fold when 22.5 vol% of silver nanowires are incorporated into the LbL film. The nanowire diameter (73 nm) higher than the thickness of the LbL films (about 50 nm) resulted in an asymmetrical cross-section with silver nanowires protruding the planar LbL film. As part of this study, an experimental technique was developed based on Newton's ring interferrometry to determine the Young's modulus, toughness, ultimate stress, and ultimate strain of the freestanding film of silver nanowire-reinforced LbL film.

Nanowire-containing LbL films possess the ability to sustain significant elastic deformation with the ultimate strain reaching 1.8%. The Young's modulus increased with increasing nanowire content reaching about 6 GPa due to the filler reinforced effect common for composite materials. The ultimate strengths of these composites were within 60-80 MPa and their toughness reached 1000 KJ/m^3 at intermediate nanowire content which is comparable to LbL films reinforced with carbon nanotubes. These values are excellent mechanical properties well-above pristine polymeric LbL nanocomposite films.

Figure 9.2 shows a representative dark-field optical image of the silver-nanowire reinforced freestanding film, $(PAH/PSS)_{10}AgNW(PAH/PSS)_{10}$ (2.5%). The Young's modulus of the films can be well-predicted according to the well-known Halpin-Tsai equation for randomly oriented fiber-reinforced laminate composites (see Appendix C).

This implies a strong interfacial interaction between the silver nanowire filler and the LbL polymeric matrix.

The robust free-standing 2D array of silver nanowires with peculiar mechanical, and conducting properties combined with excellent micromechanical stability could serve as a prospective element for microscopic acoustic, pressure, and photothermal sensors.

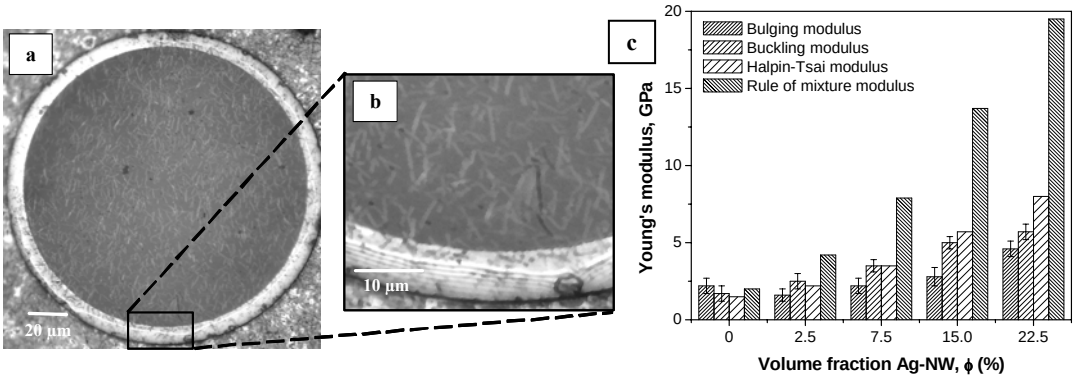

Figure 9.2. (a) Darkfield optical images of $(PAH/PSS)_{10}AgNW(PAH/PSS)_{10}$ (2.5%) with its corresponding high-magnification image (b). (c) A graph of Young's modulus of silver nanowire reinforced composite at various volume fractions.

Next, unidirectionally oriented silver nanowires encapsulated into a nanoscale polymeric film result in a mechanically anisotropic film with much significantly enhanced mechanical properties (fivefold) in the direction of nanowire orientation. This difference is caused by the fact that under a longitudinal compressive stress (parallel to the direction of orientation) the individual nanowires undergo the buckling process, thus, contributing into the higher composite stiffness of the film. The value is 0.73 ± 0.5 GPa for the direction perpendicular to the nanowire orientation with much higher value of

3.82 $\pm$ 0.5 GPa obtained for the direction along the nanowire orientation (Figure 9.3). The Young's modulus in the longitudinal and transversal directions with respect to fiber orientation can be well-predicted according to the Halpin-Tsai equation for unidirectionally oriented fibers, which also implies a strong adhesion between silver nanowire and the LbL polymer matrix (see Appendix C). And finally, the phenomenon of the buckling of the silver nanowires array encapsulated into ultrathin polymer film by the application of the compressive stress along their long axis is suggested as a straightforward and fast way for the evaluation of the elastic properties of the metal nanowires by measuring their buckling periodicity.

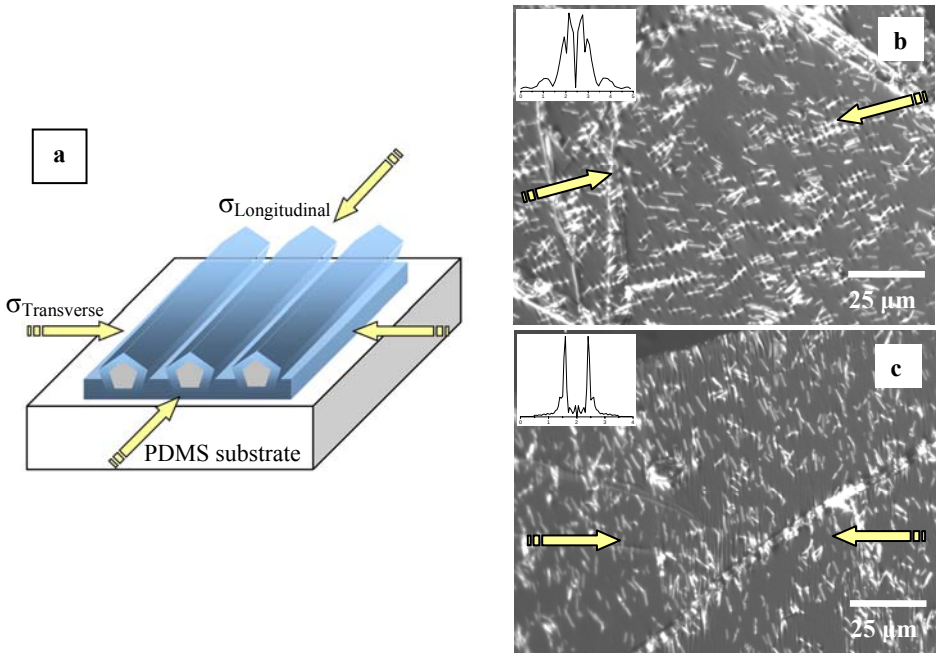

Figure 9.3. LbL of silver nanowires reinforced composite film deposited on PDMS substrate and buckled in the longitudinal and transversal directions (a) and corresponding optical images (b, c). Insets are a representative 1D FFTs for selected cross-sections of buckled nanowires. X-axis is 1/µm.

2. Bimetallic core-shell hybrid nanostructure for a SERS-based chemical sensor application: The early designs of SERS substrate that are capable of a single-molecular detection rely on an array of aggregated nanoparticles. An array of nanoparticles in close proximity, in the presence of an exciting laser could enhance the surrounding electromagnetic field due to nanoparticle-to-nanoparticle plasmon coupling. A Raman-active molecule in the proximity of such enhanced electromagnetic field will experience an enhanced Raman scattering.

Rather than utilizing array of nanoparticles aggregate to create hot-spots that require a large area of uniformly distributed nanoparticles, here we designed a Raman marker as a single core-shell nanostructure that is comprised of a silver nanoparticle core decorated with smaller gold nanoparticles shell. In this design, gold nanoparticles are assembled onto the surface of silver nanowires linked together by star polymer with terminal functional groups to resemble silver-gold nanocobs which possess dramatic increase in SERS activity, two orders of magnitude compared with bare silver nanowire.

Such a high Raman intensity and one-dimensional geometry makes silver-gold nanocob structures designed here highly attractive as prospective highly SERS-active markers which can be utilized for large-scale organized SERS arrays for sensitive analyte detection with directional sensitivity, a rarely observed ability. The unique feature of the resulting silver-gold hybrid core-shell nanostructure is the particle-to-particle interaction that subjects trapped organic molecules to an enhanced electromagnetic field. Array of

gold nanoparticles are separated from silver core with nanoscale polymer shell that is composed of both hydrophilic and hydrophobic blocks that allows for trapping of guest molecules of different types inside these pre-designed "hot inner shell" making these nanocobs interesting for applications in SERS-based sensor for a wide range of analytes.

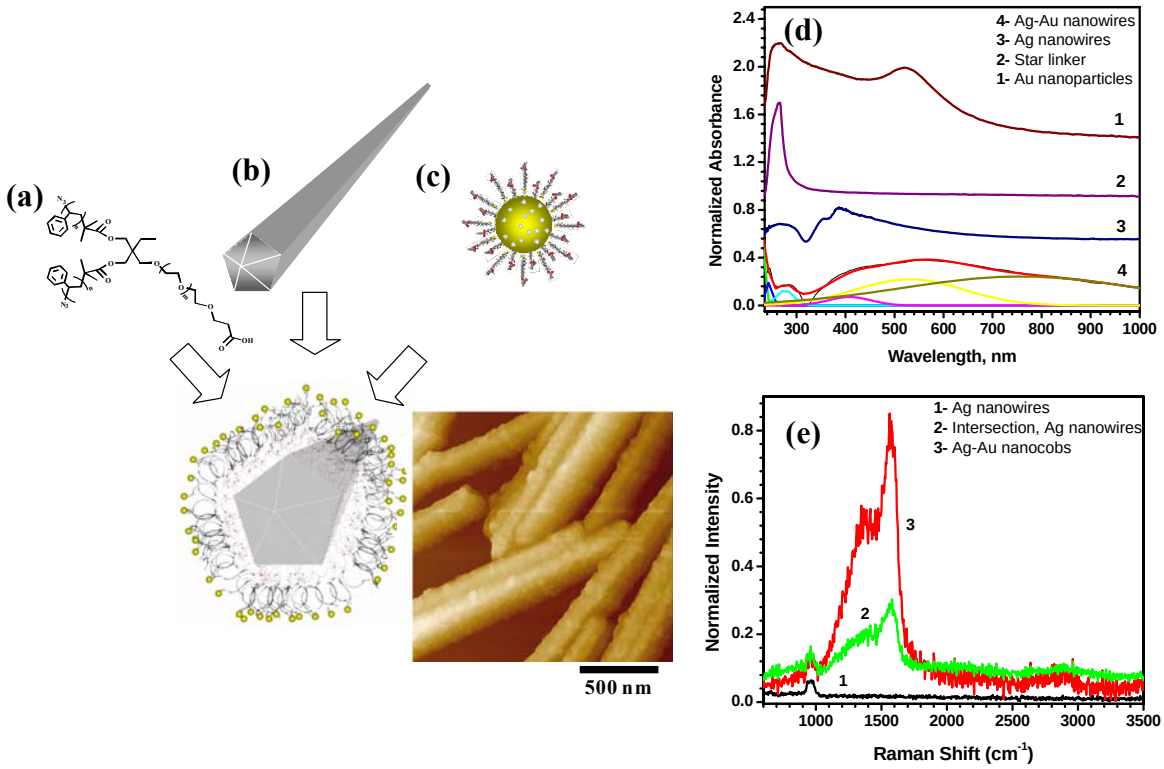

Figure 9.4. The three building blocks for a hierarchical assembly of bimetallic silver-gold nanocob: (a) a three-arm star polymer, (b) silver nanowire, (c) spherical gold nanoparticle with the corresponding AFM image of the bimetallic silver-gold nanocob. (d) UV/Vis spectra of the three building blocks and the bimetallic silver-gold nanocob, and (e) Raman spectra comparing silver nanowire with bimetallic silver-gold nanocob.

In this way, the silver-gold hybrid core-shell nanostructure is capable of a single-nanoparticle SER-substrate. The SERS enhancement exceeds Raman scattering from isolated silver nanowires by about two orders of magnitude. The effective plasmon excitation provides a broad absorption band for SERS activation which is also directionally dependent thereby making the nanocobs intriguing for a single-nanostructure SERS-substrate (Figure 9.4). Moreover, since gold nanoparticles and silver nanowires exhibit different plasmon absorption signatures, the silver-gold hybrid structure possesses a broad range of excitations.

Next, we demonstrated that ionic interactions provide an alternative approach to the synthesis of silver-gold hybrid core-shell nanostructures. In this work we used 1-D silver nanowires, 2-D silver nanoplates, and spherical gold nanoparticles as representative building blocks for the bottom-up assembly due to their facile preparations. The gold nanoparticles were ionically bound onto the 1-D silver nanowires and the 2-D silver nanoplate substrates to give 1-D and 2-D bimetallic core-shell nanostructures, respectively (Figure 9.5a, b). A different range of optical absorption is seen with change in the geometry of the core silver nanostructure, *i.e.*, silver nanowire versus silver nanoplate core (Figure 9.5c, d). The SERS ability of the hybrid nanostructures was compared with the individual nanoparticles blocks using Rhodamine 6G solution as the model analyte. At the best-found condition, a single silver nanowire-core outperforms silver nanoplate-core by four-folds, and it is in par with silver nanowires array, thus facilitating unique, extremely bright 1D Raman markers (Figure 9.5e, f).

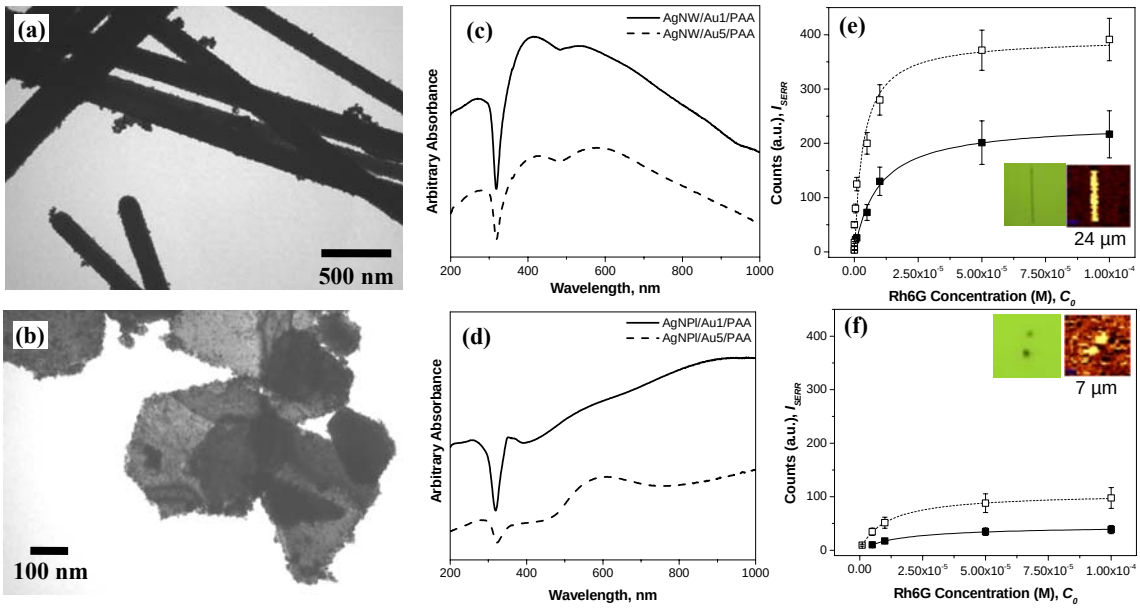

Figure 9.5. TEM images of bimetallic core-shell silver-gold (a) nanowire and (b) nanoplates with their corresponding UV/Vis absorption spectra (c, d) and Raman intensity for adsorbed Rhodamine 6G model analyte (e, f). Optical images of Langmuir-Blodgett array of: (g) silver nanowires and (i) silver nanoplates with their corresponding Raman maps (h and j, respectively). Insets are the corresponding AFM images (z=300 nm). Scan area is 20x20 μm^2 and 5x5 μm^2, respectively.

Furthermore, consistent with the previous design of silver-gold nanocob which utilized three-arm star polymer linker we found that the SERS effect due to the one-dimensional silver nanowire-gold hybrid nanostructure exhibits polarization dependence. The Raman intensity is five-times stronger when the laser polarization is perpendicular to silver nanowire orientation than when it is parallel to the silver nanowire orientation. And finally, the Raman intensity of the best performing silver-gold hybrid core-shell nanostructure was comparable with the dense array of silver nanowires and silver nanoplates that were prepared by means of LB technique (Figure 9.6). In contrast with

dense array of silver nanowires and silver nanoplates that display sporadic SERS "hot spots", the hybrid silver-gold nanoparticles display a uniform SERS "hot spot" throughout the surface (compare Figure 9.5e&f with Figure 9.5b&d). An optimized design of single nanoparticle SER-substrate based on wet-assembly technique proposed here can serve as a compact and low-cost alternative to the designs of single-nanoparticle SERS structure.

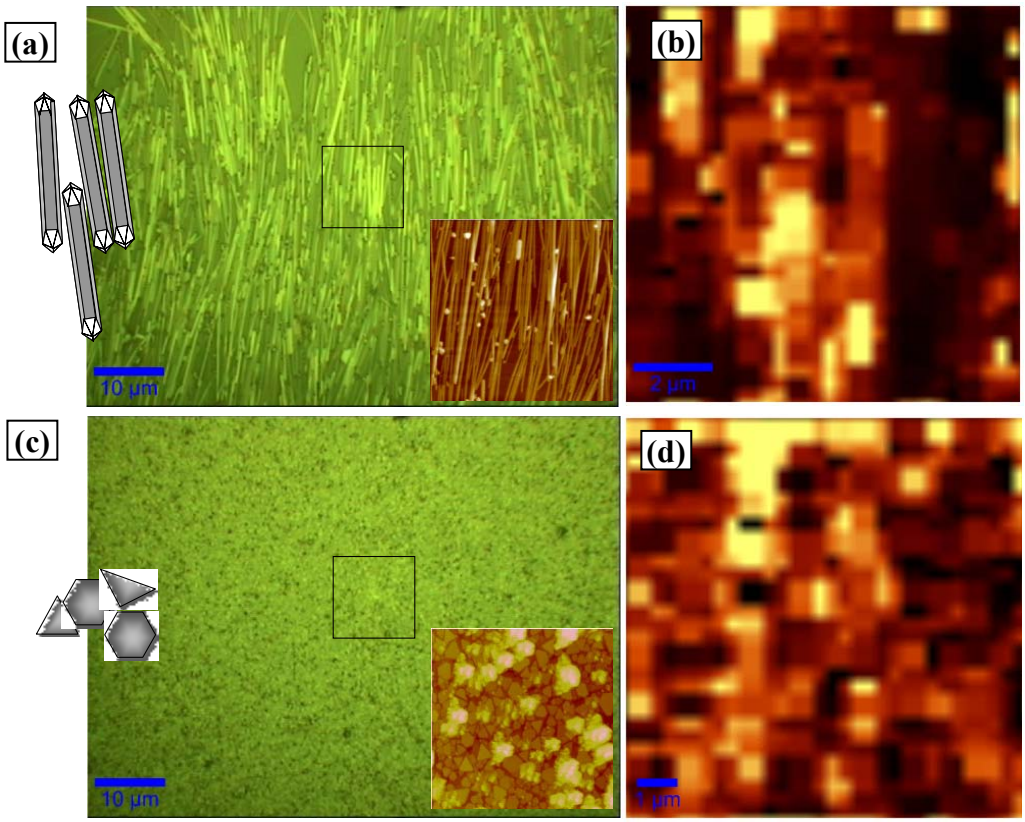

Figure 9.6. Optical images of Langmuir-Blodgett array of: (a) silver nanowires and (c) silver nanoplates with their corresponding Raman maps (b and d, respectively). Insets are the corresponding AFM images (z=300 nm). Scan area is 20x20 μm^2 and 5x5 μm^2, respectively.

In closing, we have selected representative inorganic silver and gold nanostructure building blocks due to their facile synthesis, surface modifications, and shape/configuration dependent mechanical, electrical, and optical properties for a proof-of-concept design of hierarchical assembly of novel and functional micro-nano-structures. In addition, two methods were developed for the mechanical characterization of such micro-nano-structures. Nonetheless, the established procedures can be well-extended to other nanostructures materials. Such knowledge is essential to fully utilize the burgeoning field of miniaturized systems.

The key findings from this study can be summarized as follows:

(1) Successful fabrication of ultrathin organic/inorganic films (thickness < 100nm) with tailored mechanical and electrical properties that is either isotropic or anisotropic. The nanocomposite film is robust and can be easily transferred onto various microfabricatedsubstrates.

(2) Developed mechanical characterization techniques for determining the micromechanical properties of: (a) the resulting organic/inorganic hybrid composite films based on Newton's ring interferometry of bulged film and (b) an array of highly-oriented one-dimensional metallic nanostructure by means of buckling instability.

(3) Synthesized novel bimetallic nanoparticle that exhibits tailored optical plasmon absorption spectrum within the visible and near-infrared region, as well as enhanced Raman scattering.

(4) Demonstrated proof-of-concept designs of: (a) ultra-thin composite film-based sensor and (b) single nanoparticle SERS-nanostructure chemical sensor.

CHAPTER 10

BIOGRAPHY

10.1. Refereed publications directly related to this dissertation

1. **Gunawidjaja, R.**; Kharlampieva, E.; Choi, I.; Tsukruk, V. V. Bimetallic core-shell nanostructures: gold nanoparticles assembly on 1-D and 2-D silver nanoparticles surface, 2009, Submitted to Small.
2. **Gunawidjaja, R.**; Peleshanko, S.; Ko, H.; Tsukruk, V. V. Bimetallic Nanocobs: Decorating Silver Nanowires with Gold Nanoparticles, *Advanced Materials* **2008**, *20*, 1544.
3. **Gunawidjaja, R.**; Ko, H.; Jiang, C.; Tsukruk, V. V. Buckling behavior of highly oriented silver nanowires encapsulated within layer-by-layer films. *Chemistry of Materials* **2007**, *19*, 2007.
4. **Gunawidjaja, R.**; Jiang, C.; Peleshanko, S.; Ornatska, M.; Singamaneni, S.; Tsukruk, V. V. Flexible and robust 2D arrays of silver nanowires encapsulated within freestanding layer-by-layer films, *Advanced Functional Materials* **2006**, *16*, 2024.
5. **Gunawidjaja, R.**; Jiang, C.; Ko, H.; Tsukruk, V. V. Free-standing 2D arrays of silver nanorods, *Advanced Materials* **2006**, *18*, 2895.
6. **Gunawidjaja, R.**; Peleshanko, S.; Tsukruk, V. V. Functionalized $(X\text{-}PEO)_2\text{-}(PS\text{-}Y)_2$ Star Block Copolymers at the Interfaces: Role of Terminal Groups in Surface Behavior and Morphology. *Macromolecules* **2005**, *38*, 8765.

10.2. Other related refereed publications

1. Netzer, N. L.; **Gunawidjaja, R.**; Hiemstra, M.; Zhang, Q.; Tsukruk V. V., Jiang, C. Formation and Optical Properties of Compression Induced Nanoscale Buckles on Silver Nanowires 2009, Submitted to ACS Nano.
2. **Gunawidjaja, R.**; Luponosov, Y. N.; Huang, F.; Ponomarenko, S. A.; Muzafarov, A. M.; Tsukruk, V. V. Surface molecular ordering of functionalized bithiophenesilane monodendrons. *Langmuir* **2009,** Accepted.
3. **Gunawidjaja, R.**; Huang, F.; Gumenna, M.; Klimenko, N.; Nunnery, G. A.; Shevchenko, V.; Tannenbaum, R.; Tsukruk, V. V. Bulk and Surface Assembly of Branched Amphiphilic Polyhedral Oligomer Silsesquioxane Compounds. *Langmuir* **2009**, *25*, 1196.
4. Liu, L.; Kim, J.-K.; **Gunawidjaja, R.**; Tsukruk, V. V.; Lee, M. Toroid Morphology by ABC-Type Amphiphilic Rod-Coil Molecules at the Air-Water Interface. *Langmuir* **2008**, *24*, 12340.
5. Liu, L.; Moon, K.-S., M.; **Gunawidjaja, R.**; Lee, E.; Tsukruk, V. V.; Lee, M. Molecular Reorganization of Paired Assemblies of T-Shaped Rod-Coil Amphiphilic Molecule at the Air-Water Interface. *Langmuir*, **2008**, *24*, 3930.
6. Jiang, C.; Wang, X.; **Gunawidjaja, R.**; Lin, Y.-H.; Gupta, M. K.; Kaplan, D. L.; Naik, R. R.; Tsukruk, V. V. Mechanical Properties of Robust Ultrathin Silk Fibroin Films. *Advanced Functional Materials* **2007**, *17*, 2229.
7. **Gunawidjaja, R.**; Peleshanko, S.; Genson, K. L.; Tsitsilianis, C.; Tsukruk, V. V. Surface Morphologies of Langmuir-Blodgett Monolayers of PEO_nPS_n Multiarm Star Copolymers. *Langmuir* **2006**, *22*, 6168.

8. Peleshanko, S.; **Gunawidjaja, R.**; Petrash, S.; Tsukruk, V. V. Synthesis and Interfacial Behavior of Amphiphilic Hyperbranched Polymers: Poly(ethylene oxide)-Polystyrene Hyperbranches. *Macromolecules* **2006**, *39*, 4756.
9. Peleshanko, S.; **Gunawidjaja, R.**; Jeong, J.; Shevchenko, V. V.; Tsukruk, V. V. Surface Behavior of Amphiphilic Heteroarm Star-Block Copolymers with Asymmetric Architecture. *Langmuir* **2004**, *20*, 9423.

10.3. Presentations and Proceedings

1. **Gunawidjaja, R.**; Huang, F.; Gumenna, M.; Klimenko, N.; Grady A. Nunnery, Shevchenko, V. V.; Tannenbaum, R.; Tsukruk, V. V. Silver-gold polymer composite nanocob structures. ACS National Meeting, Salt Lake City, UT, Unites States, Spring 2009. (Oral presentation)
2. **Gunawidjaja, R.**; Peleshanko, S.; Ko, H.; Tsukruk. V. V. Silver-gold polymer composite nanocob structures. ACS National Meeting, Salt Lake City, UT, Unites States, Spring 2009.
3. **Gunawidjaja, R.**; Jiang, C., Tsukruk, V. V. Determination of silver nanowires elastic modulus by means of longitudinal buckling instability. ACS National Meeting, New Orleans, LA, United States, Spring 2008. (Oral presentation)
4. **Gunawidjaja, R.**; Peleshanko, S.; Tsukruk, V. V. "Gold nanoparticles assembly on silver nanowires surface for potential Raman-based sensor" ACS National Meeting, New Orleans, LA, United States, Spring 2008. (Oral presentation)

5. **Gunawidjaja, R.**; Jiang, C.; Wang, X.-Y.; Lin, Y.-H. Gupta, M. K. David, K. L.; Naik, R. R.; Tsukruk, V. V. "Buckling and Bulging Mechanical Measurements of Nanoscale Silk Fibroin Films." MRS, San Francisco, CA, United States, Spring 2008.
6. **Gunawidjaja, R.**; Ponomarenko, S. A.; Luponosov, Y. N.; Muzafarov, A. M.; Tsukruk V. V. "Surface Morphology of n^{th} Generation Thiophene Mono-dendrons." MRS, San Francisco, CA, United States, Spring 2008.
7. **Gunawidjaja, R.** Tsukruk, V. V. Silver Nanowires Reinforced Anisotropic Polymer Composite Membrane, Nanotechnology for Defense Applications, San Diego, CA, United States, Spring 2007.
8. Jiang, C.; Wang, X.; **Gunawidjaja, R.**; Lin, Y.-H.; Naik, R. R.; Gupta, M. K.; Kaplan, D. L.; Tsukruk, V. V. Robust and biocompatible ultrathin silk fibroin films. ACS National Meeting, Chicago, IL, United States, Spring 2007.
9. Peleshanko, S.; **Gunawidjaja, R.**; Tsukruk, V. V. Role of the architecture of block copolymers on their interfacial behavior. ACS National Meeting, Washington DC, Fall 2007
10. **Gunawidjaja, R.**; Jiang, C.; Peleshanko, S.; Ornatska, M.; Singamaneni, S.; Tsukruk, Vladimir V. Freely suspended silver nanowires, MRS, Boston, MA, Fall 2006.
11. Peleshanko, S.; **Gunawidjaja, R.**; Tsitsilianis, C.; Tsukruk, V. V. Multiarm PEOn-PSn star polymers at the interfaces. ACS National Meeting, Atlanta, GA, United States, Fall 2006.
12. Peleshanko, S.; **Gunawidjaja, R.**; Tsukruk, V. V. Surface characterization of novel amphiphilic hyperbranched copolymers. ACS National Meeting, Washington DC, United States, Fall 2005.

13. **Gunawidjaja, R.**; Peleshanko, S.; Tsukruk, V. V. Influence of terminal groups on interfacial behavior and surface morphology of $(X\text{-}PEO)_2\text{-}(PS\text{-}Y)_2$ star copolymers. ACS National Meeting, Washington DC, United States, Fall 2005.
14. Peleshanko, S.; **Gunawidjaja, R.**; Tsukruk, V. V. Synthesis and characterization of novel amphiphilic hyperbranched polymers via self-condensing vinyl polymerization. National Meeting, Washington, DC, United States, Fall 2005.

APPENDIX A

PRINCIPLE OF RAMAN SPECTROSCOPY AND SURFACE ENHANCED RAMAN SEPCTROSCOPY (SERS) [349]

When molecules are irradiated with a monochromatic laser, the scattered light is composed of (1) Rayleigh scattering that has the same frequency as the source, v_0 and (2) Raman scattering that has a frequency of $v_0 \pm v_m$. $v_0 \pm v_m$ is called Stokes and $v_0 - v_m$ is called anti-Stokes. v_m is vibrational frequency of the molecule. The expression for electric field strength of the laser beam fluctuating with time is given by Equation A.1. Raman scattering is observed when the irradiated molecules experience vibrational transition (within 10^4-10^2 cm^{-1} region) that induces an electric dipole moment, P. The magnitude of the electric dipole moment is proportional to the electric field strength of the excitation laser, E (Equation A.2). α is the proportionality constant, which is called molecular polarizability. For a small amount of vibration α can be written as a linear equation as a function of nuclear displacement, q, *i.e.*, $\alpha(q)$.

$$E = E_0 \cos 2\pi v_0 t \qquad \text{(Equation A.1)}$$

$$P = \alpha E \qquad \text{(Equation A.2)}$$

$$\alpha(q) = \alpha_0 + \left(\frac{\partial \alpha}{\partial q}\right)_0 q_0 \qquad \text{(Equation A.3)}$$

Substituting Equation A.1 and Equation A.3 into A.2:

$$P = \alpha E_0 \cos 2\pi v_0 t + \left(\frac{\partial \alpha}{\partial q}\right)_0 q_0 E_0 \cos 2\pi v_0 t \qquad \text{(Equation A.4)}$$

An expression for nuclear displacement, q, for a molecule vibrating with a frequency v_m is:

$$q = q_0 \cos 2\pi v_m t \qquad \text{(Equation A.5)}$$

Further substituting Equation A.5 into A.4 yields:

$$P = \alpha E_0 \cos 2\pi v_0 t + \left(\frac{\partial \alpha}{\partial q}\right)_0 q_0 E_0 \cos 2\pi v_0 t \cos 2\pi v_m t \qquad \text{(Equation A.6)}$$

Applying trigonometric identity, the above equation can be re-written as:

$$P = \alpha E_0 \cos 2\pi v_0 t + \frac{1}{2}\left(\frac{\partial \alpha}{\partial q}\right)_0 q_0 E_0 \left[\cos\{2\pi(v_0 + v_m)t\} + \cos\{2\pi(v_0 - v_m)t\}\right]$$

(Equation A.7)

The first term on the right hand side refers to the Rayleigh scattering having the initial frequency, v_0. The second term refers to the Raman scattering frequencies v_0+v_m (Stokes) and v_0-v_m (anti-Stokes). In order for a molecule to be Raman active the change

in polarizability with respect to change nuclear displacement, $(\partial\alpha/\partial q)_0$ should be non-zero.

If the intensity of Raman scattering is proportional to the square of the induced electric dipole moment, *P*, it can be increased by either increasing the molecular polarizability, α, of electric field, *E*. The former is called chemical enhancement (CHEM) and the latter is called electromagnetic enhancement (EM). Noble metallic nanoparticles, (gold, silver, and platinum) scatter light in the visible region. The scattering is the result of the conducting electrons that locally oscillates on the confined nanoparticle surface in the presence of electric field (laser). The absorption frequency is dependent upon environment, nanoparticles shape, size, interactions between them. The maximum absorption peak coincides with the resonance frequency of the given nanoparticle shape, size and distribution, also known as localized surface plasmon (LSP). Due to the LSP phenomena, electric field within the nanoparticles vicinity is amplified (or enhanced). This mechanism refers to the electromagnetic (EM) mode. Alternatively, a chemical in the vicinity of a noble metal can experience a charge transfer (C-T) and form a bond, thus increasing its polarizability, α. This mechanism is called chemical (CHEM) mode. Raman spectroscopy measurement of a certain molecule in the presence of noble metallic nanoparticles is known as surface enhanced Raman spectroscopy (SERS).

Depending on the electronic confinement on the nanoparticle surface, several plasmon modes will be observed. The simplest example is for spherical a nanoparticle, which due to its isotropic shape, only one mode of plasmon resonance is observed, *i.e.*,

dipole resonance. Silver nanoplate, on the other hand exhibits two kinds of dipolar in-plane modes, one along its plane and another one perpendicular to its plane (Figure A.1a and Figure A.1b). [350] Two pair of positive/negative charge separation could occur simultaneously and results in a quadrupole mode (Figure A.1c and Figure A.1d).

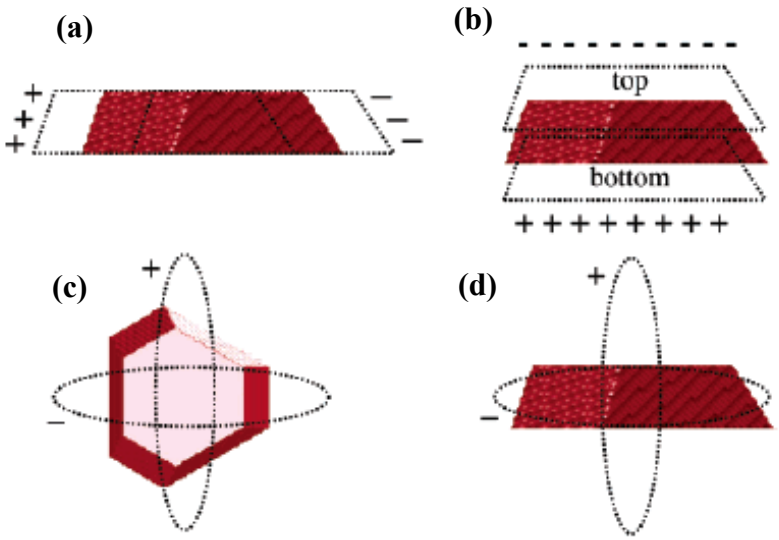

Figure A.1. Resonance plasmon modes in silver nanoplates: dipole mode (a) in-plane dipole and (b) out-of-plane dipole modes; (c) in-plane quadrupole and (d) out-of-plane quadrupole modes. [350]

APPENDIX B

PRINCIPLE OF MICROMECHANICAL MEASUREMENTS

B.1. Determination of mechanical properties of film by means of bulging measurements

The general shape of Pressure, P, versus deflection, d, curve obtained from a bulging measurement can be modeled as a circular elastic plate clamped at stiff edges, as previously derived in literature (Equation B.1). [351]

$$P = P_0 + \left[C_0 \frac{E}{(1-\nu^2)} \frac{h^4}{a^4} + C_1 \frac{\sigma_0 h^2}{a^2} \right] \left(\frac{d}{h} \right) + \left[C_2 \frac{E}{(1-\nu)} \frac{h^4}{a^4} \right] \left(\frac{d}{h} \right)^3 \qquad \text{(Equation B.1)}$$

In the above equation, P_0= initial pressure, E = Young's modulus, ν = poisson's ratio, σ_0 = residual stress, and h = film thickness. C_0, C_1, and C_2 are constant coefficients that describe the plate geometry. Simply put the above equation is a polynomial equation of the following form, where a_0, a_1, and a_2 are constant coefficients (Equation B.2):

$$P = a_0 + a_1 d + a_2 d^3 \qquad \text{(Equation B.2)}$$

This equation is applicable within the elastic region of a deformed film. Two parameters that can be derived from this equation are residual stress, σ_0, and Young's modulus, E. Furthermore, a full Pressure versus deformation curve of a film bulged

towards its failure can be converted into a stress, σ, versus strain, ε, curve according to the following expressions:

$$\varepsilon = \frac{2}{3}\left(\frac{d}{h}\right)^3 \quad \text{(Equation B.3)}$$

$$\sigma = \frac{\mathrm{Pr}^2}{4hd} \quad \text{(Equation B.4)}$$

A given set of Pressure-deflection data, n, can be fit numerically to the polynomial equation (Equation B.2) by least-square regression to give the constant coefficients, a_0, a_1, and a_2. [352] In a matrix form, the set of Pressure-deflection data can be written as Equation B.5.

$$[P] = [d][a] \quad \text{(Equation B.5)}$$

The next step is to minimize the sum of square differences on either side of the equations by multiplying with transpose matrix of [d] (Equation B.6)

$$\left[[d]^T [P]\right] = \left[[d]^T [d]\right][a] \quad \text{(Equation B.6)}$$

Finally, [a] can be solved by multiplying both sides of the equation by matrix inversion:

$$[a] = \left[[d]^T [d] \right]^{-1} \left[[d]^T [P] \right] \quad \text{(Equation B.7)}$$

A Visual Basic program was written to greatly simplify this routine analysis (SEMA research Lab. PI: Dr. Vladimir V. Tsukruk).

B.2. Buckling of film on an elastic substrate

The equation which describes an out-of-plane buckling of a polymeric film on an elastic foundation was derived from the classical Euler-Bernoulli beam equation (Equation B.8), where E is Young's modulus of beam, I is moment of inertia that dependes on the cross-sectional geometry of the beam, and EI is a constant. For beam having a rectangular cross-section, $I = \omega h^3/12$. h is thickness and ω is width of beam cross-section. In the equation, the left hand side of the equation refers to beam's deflection and the right hand side of the equation refers to the applied load. [353]

$$\bar{E}I \frac{d^4 y}{dx^4} = w(x) \qquad \text{(Equation B.8)}$$

For a beam residing on an elastic soft foundation, $w(x)$ can be represented as the sum of reaction force due to the elastic foundation, q, and a downward force due to the downward bending beam, p (Figure B.1):

$$\bar{E}I \frac{d^4 y}{dx^4} = p + q \qquad \text{(Equation B.9)}$$

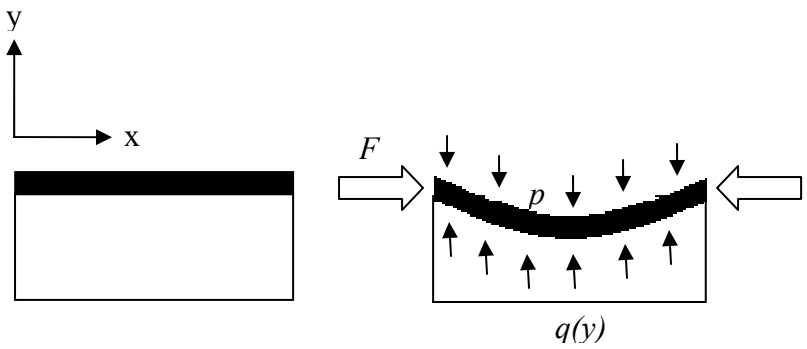

Figure B.1. Beam residing on an elastic foundation. Left is in a relaxed state and right is in a compressed state.

The deformation of the elastic foundation can be described in the form of Hooke's law as $q(y) = ky$ (Equation B.10). F is compressive force and k is Winkler modulus of half-space or modulus of resistance to displacement into the elastic substrate that is similar to Hooke's constant (Equation B.11). In Equation B.3, E_2 is Young's modulus of the elastic foundation and λ is buckling wavelength and it is valid for sinusoidal deflection (Equation B.12). Furthermore, for a deformable beam the Young's modulus, $\overline{E}$, can be re-written as Equation B.13; where v is Poisson's ratio.

$$\overline{E}I\frac{d^4y}{dx^4} + F\frac{d^2y}{dx^2} + ky = 0 \qquad \text{(Equation B.10)}$$

$$k = \frac{E\omega}{(1-v^2)}\left(\frac{\pi}{\lambda}\right) \qquad \text{(Equation B.11)}$$

$$y = A\sin\left(\frac{2\pi x}{\lambda}\right) \qquad \text{(Equation B.12)}$$

$$\overline{E} = \frac{E_1}{(1-v_1^2)} \qquad \text{(Equation B.13)}$$

Substituting Equation B.11-B.13 into Equation B.10 and solving for F yields: [354]

$$F = E_1 I\left(\frac{4\pi^2}{(1-\nu_1^2)\lambda^2} + \frac{E\omega}{4\pi(1-\nu^2)E_1 I}\lambda\right) \qquad \text{(Equation B.14)}$$

The three equations that can be derived from Equation B.14 are critical buckling wavelength, λ_{crit}, critical buckling stress, σ_{crit}, and critical buckling strain, ε_{crit}. The critical buckling wavelength can be determined from Equation B.14 by taking its derivative with respect to λ, *i.e.*, $\sigma_{crit} = dF/d\lambda$ (Equation B.15). The critical buckling stress is simply force divided by cross-sectional area of the rectangular beam, $\sigma_{crit} = F/(h\omega)$ (Equation B.16). Similarly, the critical strain is simply stress divided by Modulus of beam, $\varepsilon_{crit} = \sigma_{crit} / E_1$ (Equation B.17). In Equation B.17 Poisson's ratio is assumed negligible.

$$\lambda = 2\pi h \sqrt[3]{\frac{(1-\nu^2)E_1}{3(1-\nu_1^2)E}} \qquad \text{(Equation B.15)}$$

$$\sigma_{crit} = \sqrt[3]{\frac{9E_1E^2}{64(1-\nu_1^2)(1-\nu^2)^2}} \qquad \text{(Equation B.16)}$$

$$\varepsilon_{crit} = \sqrt[3]{\frac{9E^2}{64E_1^2}} \qquad \text{(Equation B.17)}$$

APPENDIX C

PREDICTION OF YOUNG'S MODULUS AND CONDUCTIVITY OF A FIBER-REINFORCED COMPOSITE FILM

C.1. Modulus prediction of fiber-reinforced composite film

The simplest estimation for the Young's modulus of binary composite is by employing the rule-of-mixture equation, where E_c is Young's modulus of composite, V_A is volume fraction of A component, E_B is Young's modulus of B component:

$$E_c = (V_A * E_A) + (1 - V_A)E_B \qquad \text{(Equation C.1)}$$

Alernatively, the Young's modulus of a fiber-reinforced composite can be estimated using the Halpin-Tsai equation. This equation allows a simple and rapid estimation of composite properties without the hassle of going through the tedious procedure in finite-elemental analysis. It accounts for the fiber volume fraction, V_f; fiber aspect ratio (l/d), and fiber orientation-dependent Young's modulus, i.e., Young's modulus in the Longitudinal, E_L, (Equation C.2) and Transversal, E_T, (Equation C.3) direction with respect to fiber orientation or the composite Young's modulus for randomly-oriented fiber-reinforced composite, E_{Random}, (Equation C.4). [355]

$$E_L = \left(\frac{1 + (2l/d)\eta_L V_f}{1 - \eta_L V_f} \right) E_m \qquad \text{(Equation C.2)}$$

$$E_T = \left(\frac{1 + 2\eta_T V_f}{1 - \eta_L V_f} \right) E_m \qquad \text{(Equation C.3)}$$

$$E_{Random} = \frac{3}{8} E_L + \frac{5}{8} E_T \qquad \text{(Equation C.4)}$$

, where

$$\eta_L = \frac{(E_f / E_m) - 1}{(E_f / E_m) + 2(l/d)} \qquad \text{(Equation C.5)}$$

$$\eta_T = \frac{(E_f / E_m) - 1}{(E_f / E_m) + 2} \qquad \text{(Equation C.6)}$$

C.2. Prediction of conductivity for a fiber-reinforced 2-D film

Percolation threshold, ϕ_c, of arbitrary objects embedded within a matrix is given by the following equations for two-dimensional (2D) and three-dimensional (3D) case: [356]

$$\phi_{c,2D} = 1 - Exp\left(-\frac{< A_{ex} >}{< A_e >} \times A \right) \qquad \text{(Equation C.7)}$$

$$\phi_{c,3D} = 1 - Exp\left(-\frac{< V_{ex} >}{< V_e >} \times V \right) \qquad \text{(Equation C.8)}$$

, where $<A_{ex}>$ ($<V_{ex}>$) are total excluded area (volume); $<A_e>$ ($<V_e>$) are local excluded area (volume), or average excluded area (volume); and A (V) are area (volume) of particles, respectively. The above equations take into account rod-to-rod maximum disorientation angle and the dimensions of the object. The aerial space around the object

in which the center of another such object can be placed in such a way that they will overlap is the excluded area, $\langle A_e \rangle$. For an isotropic object like a 2-D circle, $\langle A_e \rangle = 4\pi r^2$. The total excluded area is given by $\langle A_{ex} \rangle = n_c \langle A_e \rangle$ where n_c is the critical number of objects per given area. The same principle applies for excluded volume. The value of total excluded area, $\langle A_{ex} \rangle$, and total excluded volume, $\langle V_{ex} \rangle$, are determined by monte-carlo calculation, and from literature it is found to be $\langle A_{ex} \rangle$=3.57 and $\langle V_{ex} \rangle$=1.41 for a one-dimensional object. [357] For one-dimensional objects, $\langle A_e \rangle$ and $\langle V_e \rangle$ can be calculated from Equation C.9 and Equation C.10, respectively. For randomly oriented one-dimensional object in two-dimension, $\theta_\mu = \pi/2$. Whereas for the three-dimensional case, $\langle \sin\gamma \rangle_\mu = \pi/4$. W and L are width and length of the one-dimensional objects.

$$< A_e >= 4WL + W^2 + (L/2\theta_\mu)^2[4\theta_\mu - 2\sin(2\theta_\mu)] \qquad \text{(Equation C.9)}$$

$$< V_e >= (4\pi/3)W^3 + 2\pi W^2 L + 2WL^2 < \sin\gamma >_\mu] \qquad \text{(Equation C.10)}$$

REFERENCES

[1] Xia, Y.; Yang, P.; Sun, Y.; Mayers, B.; Gates, B.; Yin, Y.; Kim, F.; Yan, H. *Advanced Materials* **2003**, 15, 353.

[2] Kuchibhatla; Satyanarayana V. N. T.; Karakoti, A. S.; Bera, D.; Seal, S. One dimensional nanostructured materials. *Progress in Materials Science* **2007**, *52*, 699.

[3] Richard Turton, The Quantum Dot: A Journey into the Future of Microelectronics, Oxford University Press, USA, July 26, 1996.

[4] Nicol, E.; Habib-Jiwan, J.-L.; Jonas, A. M. *Langmuir* **2003**; *19*; 6178.

[5] Maspoch, D.; Domingo, N.; Ruiz-Molina, D.; Wurst, K.; Tejada, J.; Rovira, C.; Veciana, J. *J. Am. Chem. Soc.* **2004**; *126*; 730.

[6] Wilson, M.; Kannangara, K.; Smith, G. in Michelle Simmons, Burkhard Reguse in Nanotechnology: basic science and emerging technologies, Chapman & Hall/CRC, 2002.

[7] Halford, B. *Chemical & Engineering News* **2005**, August.

[8] Burda, C.; Chen, X.; Narayanan, R.; El-Sayed, M. A. *Chemical Reviews* **2005**, *105*, 1025.

[9] Salem, A. K.; Chen, M.; Hayden, J.; Leong, K.W.; Searson, P.C. *Nano Letters* **2004**, *4*, 1163.

[10] Yang, P.; Kim, F. *Chem. Phys. Chem.* **2002**, *3*, 503.

[11] Image is taken from: www.mooreed.com.au and "www.stochastix.wordpress.com"

[12] Xiong, Y.; Wiley, B. J.; Xia, Y. *Angewandte Chemie, International Edition* **2007**, *46*, 7157.

[13] Wiley B.; Sun Y.; Mayers B.; Xia Y. *Chemistry* (Weinheim an der Bergstrasse, Germany) **2005**, *11*, 454.

[14] Zhang, J.; Liu, H.; Wang, Z.; Ming, N. A*pplied Physics Letters* **2007**, *91*, 133112.

[15] Wang, L.; Chen, X.; Zhan, J.; Chai, Y.; Yang, C.; Xu, L.; Zhuang, W.; Jing, B. *J. Phys. Chem. B* **2005**, *109*, 3189.

[16] Xie, J.; Lee, J-Y.; Wang, I. C. (Daniel), *Chem. Mater.* **2007**, *19*, 2823.

[17] Murphy, C. J.; Gole, A. M.; Hunyadi, S. E.; Orendorff, C. J. *Inorganic Chemistry* **2006**, *45*, 7544.

[18] Ko, H.; Singamaneni, S.; Tsukruk, V. V. *Small* **2008**, *4*, 1576.

[19] Wiley, B. J.; Im, S. H.; Li, Z-Y.; McLellan, J.; Siekkinen, A.; Xia, Y. *J. Phys. Chem. B* **2006**, *110*, 15666.

[20] Huang, W.; Qian, W.; Jain, P. K.; El-Sayed, M. A. *Nano Lett.* **2007**, ASAP article.

[21] (a) Van Duyne In *Chemical and Biochemical Applications of Lasers*, C. B. Moor, Ed.; Academic Press: New York, 1979; Vol 4, pp 101-185. (b) Moskovits, M. *Rev. Mod. Phys.* **1985**, *47*, 783.

[22] Campion, A.; Ivanecky, J. E.; Child III., C. .M.; Foster, M. C. *J. Am. Chem. Soc.* **1995**, *117*, 11807.

[23] Qian, X.-M.; Nie, S. M. *Chem. Soc. Rev.* **2008**, *37*, 912.

[24] Lassiter, J. B.; Aizpurua, J.; Hernandez, L. I.; Brandl, D. W.; Romero, I.; Lai, S.; Harfner, J. H.; Nordlander, P.; Halas, N. J. *Nano Lett.* **2008**, *8*, 1212.

[25] Huang, W.; Qian, W.; Jain, P. K.; El-Sayed, M. A. *Nano Lett.* **2007**, *7*, 3227.

[26] Murphy, C. J.; Sau, T. K.; Gole, A. M.; Orendorff, C. J.; Gao, J.; Gou, L.; Hunyadi, S. E.; Li, T. *J. Phys. Chem. B* **2005**, *109*, 13857.

[27] Lal, S.; Grady, N. K.; Goodrich, G. P.; Halas, N. J. *Nano Lett.* **2006**, *6*, 2338.

[28] Bishnoi, S. W.; Rozell, C. j.; Levin, C. S.; Gheith, M. K.; Johnson, B. R.; Johnson, D. H.; Halas, N. J. *Nano Lett.*, **2006**, *6*, 1688.

[29] Karg, M.; Pastoriza-Santos, I.; Pérez-Juste, J.; Hellweg, T.; Liz-Marzán, L. M. *Small* **2007**, *7*, 1222.

[30] Das, M.; Sanson, N.; Fava, D.; Kumacheva, E. *Langmuir* **2007**, *23*, 196.

[31] Sun, Y.; Xia, Y. *Analyst* **2003**, *128*, 686.

[32] Mcdowell, M. T.; Leach, A. M.; Gall, K. *Modelling Simul. Mater. Sci. Eng.* **2008**, *16*, 1.

[33] Lucas, M.; Leach, A. M.; McDowell, M. T.; Hunyadi, S. E.; Gall, K.; Murphy, C. J.; Riedo, E. *Phys. Rev. B.* **2008**, *77*, 245420.

[34] Li, X.; Gao, H.; Murphy, C.J. ; Caswell, K. K. *Nano Lett.* **2003**, *3*, 1495.

[35] Cao, Y.; Allameh, S.; Nankivil, D.; Sethiaraj, S.; Otiti, T.; Soboyejo, W. Mater. Sci. Eng., A 2006, 427, 232.

[36] Hu, M.; Hillyard, P.; Hartland, G. V.; Kosel, T.; Perez-Juste, J.; Mulvaney, P.

Nano Lett. **2004**, *4*, 2493.

[37] Wampler, H. P.; Ivanisevic, A. *Micron* **2009**, *40*, 444.

[38] Burda, C.; Chen, X.; Narayanan, R.; El-Sayed, M. A. *Chem. Rev.* **2005**, *105*, 1025.

[39] (a) Teoh, L. G. *Current Nanoscience* **2009**, 5, 113. (b) Silvestri, B.; Luciani, G.; Costantini, A.; Tescione, F.; Branda, F.; Pezzella, A. *Journal of Biomedical Materials Research, Part B: Applied Biomaterials* **2009**, *89B*, 369. (c) Hassanzadeh, A.; Moazzez, B.; Haghgooie, H.; Nasseri, M.; Golzan, M. M.; Sedghi, H. *Central European Journal of Chemistry* **2008**, *6*, 651. (d) Chen, Y. W.; Qiao, Q.; Liu, Y. C.; Yang, G. L. *Journal of Physical Chemistry C* **2009**, *113*, 7497.

[40] Reyhani, A.; Mortazavi, S. Z.; Novinrooz, A. J. *Synthesis and Reactivity in Inorganic, Metal-Organic, and Nano-Metal Chemistry* **2009**, *39*, 31.

[41] Singh, D. P.; Ojha, A. K.; Srivastava, O. N. *Journal of Physical Chemistry C* **2009**, *113*, 3409.

[42] Zhang, Z.; Brown, S.; Goodall, J. B. M.; Weng, X.; Thompson, K.; Gong, K.; Kellici, S.; Clark, R. J. H.; Evans, J. R. G.; Darr, J. A. *Journal of Alloys and Compounds* **2009**, *476*, 451.

[43] Li, Y.; Guo, M.; Zhang, M.; Wang, X. *Materials Research Bulletin* **2009**, *44*, 1232.

[44] Wang, R.; Ruan, C.; Kanayeva, D.; Lassiter, K.; Li, Y. *Nano Letters* **2008**, *8*, 2625.

[45] Liu, B.; Aydil, E. S. *Journal of the American Chemical Society* **2009**, *131*, 3985.

[46] (a) Thongtem, S.; Wannapop, S.; Thongtem, T. *Ceramics International* **2009**, *35*, 2087. (b) Chandradass, J.; Kim, K. H. *Materials and Manufacturing Processes* **2009**, *24*, 541. (c) Ogi, T.; Kaihatsu, Y.; Iskandar, F.; Tanabe, E.; Okuyama, K. *Advanced Powder Technology* **2009**, *20*, 29. (d) Islam, M. R.; Podder, J. *Crystal Research and Technology* **2009**, *44*, 286.

[47] Wang, Y.; Wu, J.; Wei, F. *Carbon* **2003**, *41*, 2939.

[48] (a) Yin, W.; Cao, M.; Luo, S.; Hu, C.; Wei, B. *Crystal Growth & Design* **2009**, *9*, 2173, (b) Chen, Y.; Tong, Z.; Luo, L. *Chinese Journal of Chemical Engineering* **2008**, *16*, 485. (c) Zhang, H.; Zhang, Q.; Tang, J.; Qin, L.-C. *Journal of the American Chemical Society* **2005**, *127*, 2862. (d) Yang, Q.; Jian, S.; Ma, X.; Ji, Y.; Yang, D. *Superconductor Science and Technology* **2004**, *17*, L31.

[49] Yu, D.; Hu, L.; Qiao, S.; Zhang, H.; Len, S.-E. (Andy); Len, L. K.; Fu, Q.; Chen, X.; Sun, K. *Journal of Physics D: Applied Physics* **2009**, *42*, 055110.

[50] Pileni, M.-P. *Nature* **2003**, *2*, 145.

[51] Lisiecki, I. *J. Phys. Chem. B* **2005**, *109*, 12231.

[52] Murphy, C. J.; Sau, T. K.; Gole, A. M.; Orendorff, C. J.; Gao, J.; Gou, L.; Hunyadi, S. E. Li, T. *J. Phys. Chem. B*, **2005**, *109*, 13857.

[53] Xia, Y.; Xiong, Y.; Lim, B.; Skrabalak, S. E. *Angew. Chem. Int. Ed.* **2009**, *48*, 60.

[54] Wiley, B.; Sun, Y.; Xia, Y. *Acc. Chem. Res.* **2007**, *40*, 1067.

[55] Wiley, B.; Sun, Y.; Mayers, B.; Xia, Y. *Chem. Eur. J.* **2005**, *11*, 454.

[56] Xia, Y.; Xiong, Y.; Lim, B.; Skrabalak. S.E. *Angew. Chem. Int. Ed.* **2009**, *48*, 60.

[57] Wang, A.; Yin, H.; Ren M.; Liu, Y.; Jiang, T. *Applied Surface Science* **2008**, *254*, 6527.

[58] Jia, H.; Zeng, J.; An, J.; Song, W.; Xu, W.; Zhao, B. *Thin Solid Films* **2008**, *516*, 5004.

[59] Huang, L.; Cui, X.; Dukovic, G.; O'Brien, S.P. *Nanotechnology* **2004**, *15*, 1450.

[60] Gao, J.; Yu, M.; Itkis, M.E.; Bekyarova, E.; Zhao, B.; Niyogi, S.; Haddon, R.C. *J. Am. Chem. Soc.* **2004**, *126*, 16698.

[61] Lefebvre, J.; Lynch, J. F.; Llaguno, M.; Radosavljevic, M.; Johnson, A. T. *Applied Physics Letters* **1999**, *75*, 3014.

[62] Niemeyer, C.M.; Ceyhan, B. *Angew. Chem. Int. Ed.* **2001**. 40, 3685.

[63] Krstic, V.; Duesberg, G.S.; Muster, J.; Burghard, M.; Roth, S. *Chem. Mater* **1998**, *10*, 2338.

[64] Wu, Y.; Yan, H.; Huang, M.; Messer, B.; Song, J.H.; Yang, P. *Chem. Eur. J.* **2002**, 8, 1261.

[65] Wade, T.L.; Wegrowe, J.E. *The European Physical Journal Applied Physics.* **2005**, *29*, 3.

[66] Diehl, M.R.; Yaliraki, S.N.; Beckman, R.A.; Barahona, M.; Heath, J.R. *Angew. Chem. Int. Ed.* **2002**, *41*, 353.

[67] Hone, J.; Llaguno, M.C.; Nemes, N.M.; Johnson, A.T. Fischer, J.E.; Walters, D.A.; Casavant, M.J.; Schmidt, J.; Smalley, R.E. *Applied Physics Letters* **2000**, *77*, 666.

[68] Frankamp, B. L.; Boal, A. K.; Rotello, V. M. *J. Am. Chem. Soc.* **2002**, *124*, 15146.

[69] Maye, M. M.; Nykypanchuk. D.; Cuisinier, M.; van der Lelie, D.; Gang, O. *Nat. Mater.* **2009**, *8*, 388.

[70] Bockstaller, M. R.; Thomas, E. L. *J. Phys. Chem. B.* **2003**, *107*, 10017.

[71] Shan, J.; Nuopponen, M.; Jiang, H.; Viitala, T.; Kauppinen, E.; Kontturi, K.; Tenhu, H. *Macromolecules* **2005,** ASAP article.

[72] Whang, D.; Jin, S.; Wu, Y.; Liebler, C.M. *Nano Letters*. **2003**, 3(*9*), 1255.

[73] (a) Nykypanchuk, D., Maye, M. M., van der Lelie, D. & Gang, O. *Nature* **2008**, *451*, 549. (b) Park, S. Y.; Lytton-Jean A. K. R.; Lee, B.; Weigand, S.; Schatz, G. C.; Mirkin, C. A. *Nature* **2008**, *451*, 553.

[74] Kim, F.; Kwan, S.; Akana, J.; Yang, P. *J.Am.Chem. Soc.* **2001**, *123*, 4360.

[75] Hammond, P. T. *Adv. Mater.* **2004**, *16*, 1271.

76 (a) Tang, Z.; Wang, Y.; Podsiadlo, P.; Kotov, N. A. Adv. Mater. 2006, 18, 3203. (b) Srivastava, S.; Kotov, N. Accounts of Chemical Research 2008, 41, 1831.

77 Hammond, P. Adv. Mater. 2004, 16, 1271.

78 Jiang, C.; Tsukruk, V. V. 2006, 18, 829.

79 (a) Sukhishvili, S.; Kharlampieva,E.; Izumrudov, V. Macromolecules 2006, 39, 8873. (b) Kharlampieva, E.; Sukhishvili, S. A. Polymer Reviews 2006, 46, 377. (c) Sukhishvili, S. Current Opinion in Colloid and Interface Science 2005, 10, 37.

[80] Srivastava, S.; Kotov, N. A. *Acc. Chem. Res.* **2008**, *41*, 1831.

[81] Jiang, C.; Markutsya, S.; Pikus, Y.; Tsukruk, V. V. *Nat. Mater.* **2004**, *3*, 721.

[82] Mamedov, A. A.; Kotov, N. A.; Prato, M.; Guldi, D.; Wicksted, J. P.; Hirsch, A. *Nat. Mater.* **2002**, *1*, 190.

[83] Podsiadlo, P.; Kaushik, A. K.; Shim, B. S.; Agarwal, A.; Tang, Z.; Waas, A. M.; Arruda, E. M.; Kotov, N. A. *J. Phys. Chem. B* **2008**, *112*, 14359.

[84] Vozar, S.; Poh, Y-C.; Serbowicz, T.; Bachner, M.; Podsiadlo, P.; Qin, M.; Verploegen, E.; Kotov, N.; Hart, J. A. *Rev. Sci. Inst.* **2009**, *80*, 023903.

[85] Sun, Y.; Xia, Y. *Adv. Mater.* **2002**, *14*, 833.

[86] Aroca, R. F.; Goulet, P. J. G.; dos Santos, D. S.; Alvarez-Puebla, R. A.; Oliviera (J.r.), O. N. *Anal. Chem.* **2005**, *77*, 378.

[87] Tao, A.; Kim, F.; Hess, C.; Goldberger, J.; He, R.; Sun, Y.; Xia, Y.; Yang, P. *Nano Lett.* **2003**, *3*, 1229.

[88] Zhang, J.; Li, X.; Sun, X.; Li, Y. *J. Phys. Chem. B* **2005**, *109*, 12544.

[89] Brust, M.; Bethell, D.; Schiffrin, J.; Kiely, C. J. *Adv. Mater.* **1995**, *7*, 795.

[90] Tsukruk, V. V. *Rubber Chem. Technol.* **1997**, *70*, 430.

[91] Tsukruk, V. V.; Reneker, D. H. *Polymer*, **1995**, *36*, 1791.

[92] Xu, H.; Heger, F.; Mallwitz, F.; Blankenhagel, M.; Peyratout, C.; Goedel, W. A. *Macromol. Symp.* **2002**, *177*, 175.

[93] Mallwitz, F.; Goedel, W. A. *Angew. Chem. Int. Ed.* **2001**, *40*, 2645.

[94] Goedel, W. A.; Heger, R. *Langmuir* **1998**, *25*, 3470.

[95] J. W. Beams, *in Structure and Properties of Thin Solid Films* (Eds: Neugebauer, C.A.; J. B. Newkirk, D. A. Vermilyea), John Wiley, New York **1959**, p.183.

[96] Vlasak, J. J.; Nix, W. D. *J. Mater. Res.* **1992**, *7*, 3242.

[97] Markutsya, S.; Jiang, C.; Pikus, Y.; Tsukruk, V. V. *Adv. Func. Mater.* **2005**, *15*, 771.

[98] Volynskii, A. L.; Bazhenov, S.; Lebedeva, O. V.; Bakeev, N. F. *J. Mater. Sci.* **2000**, *35*, 547.

[99] Stafford, C. M.; Harrison, C.; Beers, K. L.; Karim, A.; Amis, E. J.; Vanlandingham, M. R.; Kim, H. C.; Volksen, W.; Miller, R. D.; Simonyi, E. E. *Nat. Mater.* **2004**, *3*, 545.

[100] Nolte, A. J.; Rubner, M. F.; Cohen, R. E. *Macromolecules* **2005**, *38*, 5367.

[101] Chou, K.-S.; Lai, Y.-S. *Mater. Chem. Phys.* **2004**, *83*, 82.

[102] Wiley, B.; Herricks, T.; Sun, Y.; Xia, Y. *Nano Lett.* **2004**, *4*, 1733.

[103] Murphy, C. J.; Sau, T. K.; Gole, A. M.; Orendorff, C. J.; Gao, J.; Gou, L.; Hunyadi, S. E.; Li, T. *J. Phys. Chem. B* **2005**, *109*, 13857.

[104] Sun, Y.; Yin, Y.; Mayers, B. T.; Herricks, T.; Xia, Y. *Chem. Mater.* **2002**, *14*, 4736.

[105] Sun, Y.; Gates, B.; Mayers, B.; Xia, Y. *Nano Lett.* **2002**, *2*, 165.

[106] Caswell, K. K.; Bender, C. M.; Murphy, C. J. *Nano Lett.* **2003**, *3*, 667.

[107] Zhang, S.-H.; Jiang, Z.-Y.; Xie, Z. X.; Xu, X.; Huang, R.-B.; Zheng, L.-S. *J. Phys. Chem. B* **2005**, *209*, 9416.

[108] Park, J.-H.; Oh, S.-G.; Jo, B.-W. *Mater. Chem. Phys.* **2004**, *87*, 301.

[109] A. Machulek (Jr); H. Paulo, H. P. Moisés de Oliviera, M. H. Gehlen, *Photochem. Photobiol. Sci.* **2003**, *2*, 921.

[110] Zheng, X.; Zhu, L.; Yan, A.; Wang, X.; Xie, Y. *J. Colloid Interface Sci.* **2003**, *268*, 357.

[111] Chen, S.; Carroll, D. L. *J. Phys.Chem. B.* **2004**, *108*, 5500.

[112] Rybak, B. M.; Ornatska, M.; Bergman, K. N.; Genson, K. L.; Tsukruk, V. V. *Langmuir* **2006**, *22*, 1027.

[113] Hong, B. H.; Bae, S. C.; Lee, C.-W.; Jeong, S.; Kim, K. S. *Science* **2001**, *294*, 348.

[114] Dickson, R. M.; Lyon, L. A. *J. Phys. Chem.B* **2000**, *104*, 6095.

[115] Jeong, D. H.; Zhang, Y. X.; Moskovits, M. *J. Phys. Chem.B* **2004**, *108*, 12724.

[116] Lee, S. J.; Morrill, A. R.; Moskovits, M. *J. Am. Chem. Soc.* **2006**, *128*, 2200.

[117] Orendorff, C.; Gole, A.; Sau, T. K.; Murphy, C. J. *Anal. Chem.* **2005**, *77*, 3261.

[118] Mamedov, A. A.; Kotov, N. A.; Prato, M.; Guldi, D. M.; Wicksted, J. P.; Hirsch, A. *Nat. Mater.* **2002**, *1*, 190.

[119] Hammond, P. T. *Adv. Mater.* **2004**, *16*, 1271.

[120] L. H. Sperling, *Polymeric Multicomponent Materials: An Introduction*, John Wiley & Sons, Inc, **1997**.

[121] A. Heilmann, in *Polymer Films with Embedded Metal Nanoparticles* (Eds: R. Hull, R. M. Osgood Jr., J. Parisi), Springer **2003**.

[122] Decher, G. *Science* **1997**, *277*, 1232.

[123] Decher, G.; Schlenoff, J. B. *Multilayer Thin Films*; Wiley-VCH: Weinheim, **2003**.

[124] Lvov, Y.; Price, R.; Gaber, B.; Ichinose, I. *Colloids Surf., A.*, **2002**, *198*, 375.

[125] Hammond, P. T. *Adv. Mater.* **2004**, *16*, 1271.

[126] Jiang, C.; Markutsya, S.; Pikus, Y.; Tsukruk, V. V. *Nat. Mater.* **2004**, *3*, 721.

[127] Mamedov, A. A.; Kotov, N. A.; Prato, V.; Guldi, D. M.; Wicksted, J. P.; Hirsch, A. *Nat. Mater.* **2002**, *1*, 190.

[128] Chu, Y.-C.; Wang, C.-C.; Chen, C.-Y. *J. Membr. Sci.* **2005**, *247*, 201.

[129] Jiang, C.; Tsukruk, V. V. *Adv. Mater.* **2006**, *18*, 829.

[130] Lu, Y.; Liu, G. L.; Lee, L. P. *Nano Lett.* **2005**, *5*, 5.

[131] a) Ko, H.; Jiang, C.; Tsukruk, V.V. *Chem. Mater.* **2005**, *17*, 5489. b) Jiang, C.; Markutsya, S.; Shulha, H.; Tsukruk, V. V. *Adv. Mater.* **2005**, *17*, 1669.

[132] Jiang, C.; Rybak, B. M.; Markutsya, S.; Kladitis, P. E.; Tsukruk, V. V. *Appl. Phys. Lett.* **2005**, *86,* 121912.

[133] Jiang, C.; Ko, H.; Tsukruk, V. V. *Adv. Mater.* **2005**, *17,* 2127.

[134] G. Schmid, *Nanoparticles from Theory to Application*; Wiley-VCH, 2004.

[135] Gunawidjaja, R.; Jiang, C.; Ko, H.; Tsukruk, V. V. *Adv. Mater.* **2006,** accepted.

[136] Jiang, C.; Tsukruk, V. V.*Soft Matter.* **2005**, *1*, 334.

[137] Jiang, C.; Lio, W. Y.; Tsukruk, V. V. *Phys. Rev. Let.* **2005**, *95*, 115503.

[138] Jiang, C.; Markutsya, S.; Tsukruk, V. V. *Langmuir* **2004**, *20*, 882.

[139] Jiang, C.; Ko, H.; Tsukruk, V. V. *Adv. Mater.* **2005**, *17*, 2127.

[140] Cho, J.; Char, K.; Hong, J.-D.; Lee, K.-B. *Adv. Mater.* **2001**, *13*, 1076.

[141] Chiarelli, P. A.; Johal, M. S.; Casson, J. L.; Roberts, J. B.; Robinson, J. M.; Wang, H.-L. *Adv. Mater.* **2001**, *13*, 1167.

[142] Mamedov, A. A.; Kotov, N. A. *Langmuir.* **2000**, *16*, 5530.

[143] Jana, N. R.; Gearheart, L.; Murphy, C. J. *Chem. Commun.* **2001**, 617.

[144] Chen, D.; Gao, L. *J. Cryst. Growth* **2004**, *264*, 216.

[145] Gao, Y.; Jiang, P.; Song, L.; Liu, L.; Yan, X.; Zhou, Z.; Liu, D.; Wang, J.; Yuan, H.; Zhang, Z.; Zhao, X.; Dou, X.; Zhou, W.; Wang, G.; Xie, S. *J. Phys. D: Appl. Phys.* **2005**, *38*, 1061.

[146] Gasga-Reyes, J.; Elechiguerra, J. L.; Liu, C.; Camacho-Bragado, A.; Montejano-Carrizales, J. M.; Jose Yacaman, M. *J. Cryst. Growth* **2006**, *286*, 162.

[147] Murphy, C. J.; Sau, T. K.; Gole, A. M.; Orendorff, C. J.; Gao, J.; Gou, L.; Hunyadi, S. E.; Li, T. *J. Phys. Chem. B* **2005**, *109*, 13857.

[148] Jayaraman, S.; Edwards, R. L.; Hemker, K. J. *J. Mater. Res.* **1999**, *14*, 688.

[149] Poilane, C.; Delobelle, P.; Lexcellent, C.; Hayashi, S.; Tobushi, H. *Thin Solid Film* **2000**, *379*, 156.

[150] S. N. Magonov, *Surface analysis with STM and AFM: experimental and theoretical aspects of image analysis*; VCH: Weinheim: Germany, and New York, 1996.

[151] D. D. Agarwal, L. J. Broutman, *Analysis and Performance of Fiber Composites*, Second Edition, John Wiley & Sons, 1990, p.129.

[152] Ko, H.; Jiang, C.; Shulha. H.; Tsukruk, V. V. *Chem. Mater.* **2005,** *17*, *2490.*

[153] Li, X.; Gao, H.; Murphy, C. J.; Caswell, K. K. *Nano Lett.* **2003**, *3*, 1495.

[154] Kraft, O.; Volkert, C. A. *Adv. Mat.* **2001**, *3*, 99.

[155] Kalkman, A. J.; Vebruggen, A. H.; Janssen, G. C. A. M. *Rev. Sci. Instrum.* **2003**, *74*, 1383.

[156] D. K. Felbeck, A. G. Atkins, in *Strength and Fracture of Engineering Solids*, Prentice-Hall, **1984**.

[157] Hashemi, S. *J. Mat. Sci.,* **1997,** *32*, 1563.

[158] R. N. Rothon, in *Particulate Filled Polymer Composites*, Rapra Technology Limited: **2003**.

[159] Heaney, M. B. Electrical conductivity and resistivity. In: Webster, J. G., editor. Electrical Measurement, Signal Processing and Displays. Boca Raton, FL: CRC Press; 2003.

[160] E. K. Sichel, in *Carbon Black Polymer Composites: The physics of Electrically Conducting Composites*, Marcel Dekker, Inc., New York and Basel **1982**.

[161] Celzard, A.; McRae, E.; Deleuze, C.; Dufort, M.; Furdin, G.; Marêché, J. F. *Phys. Rev. B* **1996**, *53*, 6209.

[162] Balberg, I.; Anderson, C. H.; Alexander, S.; Wagner, N. *Phys. Rev. B* 1984, *30*, 3933.

[163] Sönnichsen, C.; Alivisatos, A. P. *Nano Lett.* **2005**, *5*, 301.

[164] Murphy, C. J.; Sau, T. K.; Gole, A. M.; Orendorff, C. J.; Gao, J.; Gou, L.; Hunyadi, S. E.; Li, T. *J. Phys. Chem., B.* **2005**, *109*, 13857.

[165] Dickson, R. M.; Lyon, L. A. *J. Phys. Chem., B* **2000**, *104*, 6095.

[166] Graff, A.; Wagner, D.; Ditlbacher, H.; Kreibig, U. *Eur. Phys. J. D* **2005**, *34*, 263.

[167] Sanders, A. W.; Routenberg, D. A.; Wiley, B. J.; Xia, Y.; Dufresne, E. R.; Reed, M. A. *Nano Lett.* **2006**, *6*, 1822.

[168] Maier, S. A.; Kik, P. G.; Atwater, H. A.; Meltzer, S.; Harel E.; Koel, B. E.; Requicha, A. A. *Nat. Mater.* **2003**, *2*, 229.

[169] Du, F.; Fischer, J. E.; Winey, K. I. *Phys. Rev., B.* **2005**, *72*, 121404.

[170] Thostenson, E. T.; Chou, T-W. *Carbon* **2004**, *42*, 3003.

[171] Whang, D.; Jin, S.; Wu, Y.; Lieber, C. M. *Nano Letters* **2003**, *3*, 1255.

[172] Jin, S.; Whang, D.; McAlpine, M. C.; Friedman, R. S.; Wu, Y.; Lieber, C. M. *Nano Letters* **2004**, *4*, 915.

[173] Kim, F.; Kwan, S.; Akana, J.; Yang, P. *J. Am. Chem. Soc.* **2001**, *123*, 4360.

[174] Jiang, C.; Tsukruk, V. V. *Adv. Mater.* **2006**, *18*, 829.

[175] Jiang, C.; Markutsya, S.; Pikus, Y.; Tsukruk, V. V. *Nat. Mater.* **2004**, *3*, 721.

[176] Jiang, C.; Kommireddy, D. S.; Tsukruk, V. V. *Adv. Func. Mater.* **2006**, *16*, 27.

[177] Markutsya, S.; Jiang, C.; Pikus, Y.; Tsukruk, V. V. *Adv. Func. Mater.* **2005**, *15*, 771.

[178] Jiang, C.; McConney, M. E.; Singamaneni, S.; Merrick, E.; Chen, Y.; Zhao, J.; Zhang, L.; Tsukruk, V. V. *Chem. Mater.* **2006**, *18*, 2632.

[179] Pérez-Juste, J.; Pastoriza-Santos, I.; Liz-Marzán, L. M.; Mulvaney, P. *Coord. Chem. Rev.* **2005**, *249*, 1870.

[180] Gupta, S.; Zhang, Q.; Emrick, T.; Russell, T. P. *Nano Lett.* **2006**, *6*, 2066.

[181] Nikoobakht, B.; Wang, Z. L.; El-Sayed, M. A. *J. Phys. Chem., B.* **2000**, *104*, 8635.

[182] Fendler, J. H. *Chem. Mater.* **1996**, *8*, 1616.

[183] Shan, J.; Nuopponen, M.; Jiang, H.; Viitala, T.; Kauppinen, E.; Kontturi, K.; Tenhu, H. *Macromolecules* **2005**, *38*, 2918.

[184] Fauré, M. C.; Bassereau, P.; Lee L. T.; Menelle A.; Lheveder C. *Macromolecules* **1999**, *32*, 8538.

[185] Peleshanko, S.; Jeong, J.; Gunawidjaja, R.; Tsukruk, V. V. *Macromolecules,* **2004**, *37*, 6511.

[186] Gunawidjaja, R.; Peleshanko, S.; Tsukruk, V. V. *Macromolecules*, **2005,** *38,* 8765.

[187] Peleshanko, S.; Gunawidjaja, R.; Petrash, S.; Tsukruk, V. V. *Macromolecules* **2006**, *39*, 4756.

[188] Gao, Y.; Jiang, P.; Liu, D. F.; Yuan, H. J.; Yan, X. Q.; Zhou, Z. P.; Wang, J. X.; Song, L.; Liu, L. F.; Zhou, W. Y.; Wang, G.; Wang, C. Y.; Xie, S. S.; Zhang, J. M.; Shen, D. Y. *J. Phys. Chem., B.* **2004**, *108*, 12877.

[189] Smith, J. N.; Meadows, J.; Williams, P. A. *Langmuir* **1996**, *12*, 3773.

[190] Olek, M.; Ostrander, J.; Jurga, S.; Moehwald, H.; Kotov, N.; Kempa, K.; Giersig, M. *Nano Lett.* **2004**, *4*, 1889.

[191] Jiang, C.; Singamaneni, S.; Merrick, E.; Tsukruk, V. V. *Nano Lett.* **2006**, *6*, 2254.

[192] Li, X.; Gao, H.; Murphy, C. J.; Caswell, K. K. *Nano Lett.* **2003**, *3*, 1495.

[193] Bhagwan D. Agarwal and Lawrence J. Broutman, *"Analysis and Performance of Fiber Composites,"* Second Edition, 1990, Pg 92.

[194] Volynskii, A. L.; Bazhenov, S.; Lebedeva, O. V.; Bakeev, N. F. *J. Mater. Sci.* **2000**, *35*, 547.

[195] R.C. Hibbeler, *"Mechanics of Materials,"* Prentice Hall, Fourth Edition, 2000, P. 652.

[196] Cao, Y.; Allameh, S.; Nankivil, D.; Sethiaraj, S.; Otiti, T.; Soboyejo, W. *Mater. Sci. Eng., A* **2006**, *427*, 232.

[197] Wu, B.; Heidelberg, A.; Boland, J. J.; Sader, J. E.; Sun, X.; Li, Y. *Nano Lett.* **2006**, *6*, 468.

[198] Cuenot, S.; Frétigny, C.; Demoustier-Champagne, S.; Nysten, B. *Phys. Rev., B* **2004**, *69*, 165410.

[199] Khangm D.-Y.; Xiao, J.; Kocabas, C.; MacLaren, S.; Banks, T.; Jiang, H.; Huang, Y. Y.; Rogers, J. A. *Nano Lett.* **2008**, *8*, 124.

[200] Voulgaris, D.; Tsitsilianis, C.; Esselink, F.J.; Hadziioannou, G. *Polymer* **1998**, 39, 6429.

[201] Narrainen, A.P.; Pascual, S.; Haddleton, D.M. *J. Polym. Sci.: Part A: Polym. Chem.* **2002**, *40*, 439.

[202] Voulgaris, D; Tsitsilianis, C. *Macromol. Chem. Phys.* **2001**, *202*, 3284.

[203] Ornatska, M.; Bergman, K. N.; Rybak, B.; Peleshanko, S.; Tsukruk, V. V. *Angew. Chem.* **2004,** *43*, 5246

[204] Ornatska, M.; Peleshanko, S.; Genson, K. L.; Rybak, B.; Bergman, K. N.; Tsukruk, V. V. *J. Am. Chem. Soc.*, **2004**, *126*, 9675.

[205] Ornatska, M.; Peleshanko, S.; Rybak, B.; Holzmueller, J.; Tsukruk, V. V., *Adv. Mater.* **2004,** *16*, 2206.

[206] Boyce, J. R.; Shirvanyants, D.; Sheiko, S. S.; Ivanov, D. A.; Qin, S.; Boerner, H.; Matyjaszewski, K. *Langmuir* **2004**, *20*, 6005.

[207] Lord, S. J.; Sheiko, S. S.; LaRue, I.; Lee, H.; Matyjaszewski, K. *Macromolecules* **2004**, *37*, 4235.

[208] Kanaoka, S.; Kanaoka, S.; Nakata, S.; Yamaoka, H. *Macromolecules* **1992**, *25*, 6414.

[209] Kanaoka, S.; Sawamoto, M.; Higashimura, T. *Macromolecules* **1993**, *26*, 254.

[210] Genson, K. L.; Hoffman, J.; Teng, J.; Zubarev, E. R.; Vaknin, D.; Tsukruk, V. V. *Langmuir,***2004,** *20,* 9044.

[211] Luzinov, I.; Minko, S.; Tsukruk, V. V. *Prog. Polym. Sci.* **2004**, *29,* 635.

[212] Holzmueller, J.; Genson, K. L.; Park, Y.; Yoo, Y.-S.; Park, M.-H.; Lee, M.; Tsukruk, V. V. *Langmuir,* **2005,** *21*, 6392.

[213] Kanaoka, S.; Nakata, S.; Yamaoka, H. *Macromolecules* **2002,** *35*, 4564.

[214] Herman, D.S.; Kinning, D.J.; Thomas, E.L.; Fetters, L.J. *Macromolecules* **1987**, *20*, 2940.

[215] Tselikas, Y.; Hadjichristidis, N.; Lescanec, R.L.; Honeker, C.C.; Wohlgemuth, M.; Thomas, E.L. *Macromolecules* **1996**, *29*, 2290.

[216] Pochan, D.J.; Gido, S.P.; Pispas, S.; Mays, J.W.; Ryan, A.J.; Fairclough, P.A.; Hamley, I.W.; Terrill, N.J. *Macromolecules* **1996**, *29*, 5091.

[217] Lin, Y.-H.; Teng, J.; Zubarev, E. R.; Shulha, H.; Tsukruk, V. V. *Nano Lett.* **2005***, 5*, 491.

[218] Julthongpiput, D.; Lin, Y-H.; Teng, J.; Zubarev, E. R.; Tsukruk*,* V. V. *J. Am. Chem. Soc.* **2003**, *125*, 15912.

[219] Pochan, D.J.; Gido, S.P.; Pispas, S.; Mays, J.W. *Macromolecules* **1996**, *29*, 5099.

[220] Gido, S.P.; Lee, C.; Pochan, D.J.; Pispas, S.; Mays, J.W.; Hadjichristidis, N. *Macromolecules* **1996**, *29*, 7022.

[221] Hadjichristidis, N.; Pitsikalis, M.; Iatrou, H.; Pispas, S. *Macromol. Rapid Commun.* **2003**, *24*, 979.

[222] Pispas, S.; Avgeropoulos, A.; Hadjichristidis, N.; Roovers, J. *Journal of Polymer Science, Part B: Polymer Physics* **1999**, 37, 1329.

[223] Houli, S.; Iatrou, H.; Hadjichristidis, N.; Vlassopoulous, D. *Macromolecules* **2002**, *35*, 6592.

[224] Okamoto, S.; Hasegawa, H.; Hashimoto, T.; Fujimoto, T.; Zhang, H.; Kazama, T.; Takano, A.; Isono, Y. *Polymer* **1997**, *38*, 5275.

[225] Zhao, Y.; Shuai, X.; Chen, C.; Xi, F. *Chem. Commun.* **2004**, 1608.

[226] Webster, O. W. *Science*, **1991**, *251*, 887.

[227]. Peleshanko, S.; Jeong, J.; Shevchenko, V., V.; Petrash, S.; Tsukruk, V. V. *Macromolecules* **2004**, *37*, 7497.

[228]. Huang, H-M.; Liu, I-C.; Tsiang, C-C. R. *Polymer* **2004**, *46*, 955.

[229]. Greene, T.W.; Wuts, P.G.M. *Protective Groups in Organic Synthesis;* Wiley-Interscience: New York, 3rd edition, 1999.

[230]. Carnahan, M.A.; Grinstaff, M.W. *Macromolecules* **2001**, *34*, 7648.

[231]. Luman, N.R.; Smeds, K.A.; Grinstaff, M.W *Chem. Eur. J.* **2003**, *9*, 5618.

[232]. Coessens, V.; Nakagawa, Y.; Matyjaszewski, K. *Polym. Bull.* **1998**, *40*, 135.

[233] Huang, W.;Qian, W.; Jain, P. K.; El-Sayed, M. A. *Nano Lett.* **2007**, *7*, 3227.

[234] Wiley, B. J.; Im, S. H.; Li, Z-Y.; McLellan, J.; Siekkinen, A.; Xia, Y. *J. Phys. Chem. B* **2006**, *110*, 15666.

[235] Sun, Y.; Xia, Y. *Analyst* 2003, *128*, 686.

[236] Burda, C.; Chen, X.; Narayanan, R.; El-Sayed, M. A. *Chem. Rev.* 2005, *105,* 1025.

[237] Wiley, B.; Sun, Y.; Mayers, B.; Xia, Y. *Chemistry-A European Journal* 2005, *11,* 454.

[238] Murphy, C. J.; Sau, T. K.; Gole, A. M.; Orendorff, C. J.; Gao, J.; Gou, L.; Hunyadi, S. E.; Li, T. *J. Phys. Chem. B* **2005**, *109*, 13857.

[239] Murphy, C. J.; Gole, A. M.; Hunyadi, S. E.; Orendorff, C. J. *Inorg. Chem.* **2006**, *45*, 7544.

[240] Lal, S.; Grady, N. K.; Goodrich, G. P.; Halas, N. J. *Nano Lett.* 2006, *6*, 2338.

[241] Bishnoi, S. W.; Rozell, C. J.; Levin, C. S.; Gheith, M. K.; Johnson, B. R.; Johnson, D. H.; Halas, N. J. *Nano Lett.* 2006, *6*, 1687.

[242] Knight, M. W.; Grady, N. K.; Bardhan, R.; Hao, F.; Norlander, P.; Halas, N. J. *Nano Lett.* **2007**, *7,* 2346.

[243] Karg, M.; Pastoriza-Santos, I.; Pérez-Juste, J.; Hellweg, T.; Liz-Marzán, L. M. *Small* **2007**, *3*, 1222.

[244] Das, M.; Sanson, N.; Fava, D.; Kumacheva, E. *Langmuir* **2007**, *23*, 196.

[245] Zhang, Q.;Atay, T.; Tischler, J. R.; Bradley, M. S.; Bulovic, V.; Nurmikko, A. V. *Nature Nanotechnology* **2007**, *2*, 555.

[246] Ghosh, S. K.; Pal, T. *Chem. Rev.* **2007**, *107*, 4797.

[247] Westcott, S. L.; Jackson, J. B.; Radloff, C.; Halas, N. J. *Phys. Rev. B: Condens. Matter.* **2002**, *66*, 155431.

[248] Xia, Y.; Halas, N. *MRS Bull.* **2005**, *30*, 338.

[249] Zhang, J.; Liu, H.; Wang, Z.; Ming, N. *J. Solid State Chem.* **2007**, *180*, 1291.

[250] Guo, S.; Wang, Y.; Fang, Y.; Wang, E. *J. Coll. Int. Sci.* **2007**, *315*, 363.

[251] Sainsbury, T.; Ikuno, T.; Okawa, D.; Pacilé, D.; J. Fréchet, J. M.; Zettl, A. *J. Phys. Chem C.* **2007**, *111*, 12992.

[252] Hunyadi, S. E.; Murphy, C. J. *J. Mater. Chem.* **2006**, *16*, 3929.

[253] Teranishi, T.; Inoue, Y.; Nakaya, M.; Oumi, Y.; Sano, T. *J. Am. Chem. Soc.* **2004**, *126*, 9914.

[254] Talley, C. E.; Jackson, J. B.; Oubre, C.; Grady, N. K.; Hollars, C. W.; Lane, S. M.; Huser, T. R.; Nordlander, P.; Halas, N. J. *Nano Lett.* **2005**, *5*, 1569.

[255] Wang, H.; Brandl, D. W.; Le, F.; Nordlander, P.; Halas, N. *Nano Lett.***2006**, *6*, 827.

[256] Pierrat, S.; Zins, I.; Breivogel, A.; Sonnichsen, C. *Nano Lett.* **2007**, 7, 259.

[257] Jana, N. R.; Pal, T. *Adv. Mater.* **2007**, *19*, 1761.

[258] Jung, H. Y.; Park, Y-K.; Park, S.; Kim, S. K. *Anal. Chim. Acta* **2007**, *602*, 236.

[259] Glembocki, O. J.; Prokes, S. M.; Szmacinski, H.; Liu, J.; Kub, F.; Kub, C. *Proc. of SPIE* **2005**, *6008*, 600809/1-600809/8.

[260] Zhang, J.; Li, X.; Sun, X.; Li, Y. *J. Phys. Chem B.* **2005**, *109*, 12544.

[261] Qin, L.; Zou, S.; Xue, C.; Atkinson, A.; Schatz, G. C.; Mirkin, C. A. *PNAS* **2006**, *103*, 13300.

[262] Schierhorn, M.; Liz-Marzán, L. M. *Nano Lett.* **2002**, *2*, 13.

[263] Tao, A.; Sinsermsuksakul, P.; Yang, P. *Nat. Nanotechnol.* **2007**, *2*, 435.

[264] Jeong, D-H.; You, X-Z.; Moskovits, M. *J. Phys. Chem. B.* **2004**, *108*, 12724.

[265] Lee, S. J.; Morrill, A. R.; Moskovits, M. *J. Am. Chem. Soc.* **2006**, *128***,** 2200.

[266] Sun, Y.; Xia, Y. *Adv. Mater*. **2004**, *16*, 264.

[267] Sun, Y.; Wiley, B.; Li, Z-Y.; Xia, Y. *J. Am. Chem. Soc.* 2004, *126*, 9399.

[268] Pande, S.; Ghosh, S. K.; Praharaj, S.; Panigrahi, S.; Basu, S.; Jana, S.; Pal, A.; Tsukuda, T.; Pal, T. *J. Phys. Chem. C* **2007**, *111*, 10806.

[269] Mohanty, P.; Yoon, I.; Kang, T.; Seo, K.; Varadwaj, K.; Kumar, S. K.; Choi, W.; Park, Q-H.; Ahn, J. P.; Suh, Y. D.; Hyotcherl, I.; Bongsoo, K. *J. Am. Chem. Soc.* **2007**, *129*, 9576.

[270] Liz-Marzán, L. M. *Langmuir* **2006**, *22*, 32.

[271] Wang, X.; Zhang, Z.; Hartland, G. V. *J. Phy. Chem. B* **2005**, *109*, 20324.

[272] Lee, K-S.; El-Sayed, M. A. *J. Phys. Chem. B* **2006**, *110*, 19220.

[273] Jackson, J. B.; Halas, N. J. *J. Phys. Chem. B* **2001**, *105*, 2743.

[274] Gunawidjaja, R.; Jiang, C.; Peleshanko, S.; Ornatska, M.; Singamaneni, S.; Tsukruk, V. V. *Adv. Funct. Mater.* **2006**, *16*, 2024.

[275] Peleshanko, S.; Jeong, J.; Shevchenko, V. V.; Genson, K. L.; Pikus, Y.; Ornatska, M.; Petrash, S.; Tsukruk, V. V. *Macromolecules* **2004**, *37*, 7497.

[276] Gunawidjaja, R.; Peleshanko, S.; Tsukruk, V. V. *Macromolecules* **2005**, *38*, 8765.

[277] Peleshanko, S.; Jeong, J.; Gunawidjaja, R.; Tsukruk, V. V. *Macromolecules* **2004**, *37*, 6511.

[278] Zubarev, E.; Xu, J.; Sayyad, A.; Gibson, J. D. *J. Am. Chem. Soc.* **2006**, *128*, 15098.

[279] Gittins, D. I.; Caruso, F. *Angew. Chem. Int. Ed.* **2001**, *40*, 3001.

[280] Peleshanko, S.; Gunawidjaja, R.; Petrash, S.; Tsukruk, V. V. *Macromolecules* **2006**, *39*, 4756.

[281] Malkoch, M.; Schleicher, K.; Drockenmuller, E.; Hawker, C. J.; Russell, T. P.; Wu, P.; Fokin, V. V. *Macromolecules* **2005**, *38*, 3663.

[282] Voggu, R.; Suguna, P.; Chandasekaran, S.; Rao, C. N. R. *Chem. Phys. Lett.* **2007**, *443*, 118.

[283] Ranjan, R.; Brittain, W. J. *Macromolecules* **2007**, *40*, 6217.

[284] Karim, A.; Tsukruk, V. V.; Douglas, J. F.; Satija, S. K.; Fetters, L. J.; Reneker, D. H. Foster, M. D. *J. de Phys.* **1995**, *5*, 1441.

[285] Ding, J.; Birss, V. I.; Liu, G. *Macromolecules* **1997**, *30*, 1442.

[286] Jiang, C.; Lio, W. Y.; Tsukruk, V.V. *Phys. Rev. Lett.* **2005**, *95*, 115503/1-115503/4.

[287] Furushima, Y.; Tazaki, K.; Fujimoto, H. *Solid State Commun.* **2006**, *140*, 240-244.

[288] Bruzzone, S.; Malvaldi, M.; Arrighini, G. P.; Guidotti, C. *Mater. Sci. Eng., C* **2007**, *27*, 1015.

[289] Hu, J. C.; Su, P. Y. ; Lapeyronie,V. ; Cheng, S. L. ; Lin, M. Y. ; Chen, L. J. *J. Electron. Mater.***2004**, *33*, 1058.

[290] Jiang, C. ; Markutsya, S. ; Tsukruk, V. V. *Langmuir* **2004**, *20*, 882.

[291] Kikuchi, M.; Shiratori, S. *Sens. Actuators B* **2005**, *108*, 564.

[292] Kim, J. H.; Kim, S. H.; Shiratori, S. *Sens. Actuators B* **2004**, *102*, 241.

[293] Sugimoto, I.; Nagaoka, T.; Seyamab, M.; Nakamurac, M.; Takahashi, K. *Sensors and Actuators B* **2007**, *124*, 53.

[294] Zhang, J.; Li, X.; Sun, X.; Li, Y. *J. Phys. Chem. B.* **2005**, *109*, 12544.

[295] Burda, C.; Chen, X.; Narayanan, R.; El-Sayed, M. A. *Chem. Rev.* **2005**, *105*, 1025.

[296] Zhang, B.; Wang, H.; Lu, L.; Ai, K.; Zhang, G.; Cheng, X. *Adv. Func. Mater.* **2008**, *18*, 2348.

[297] Sun, Y.; Xia, Y. *Analyst* **2003**, *128*, 686.

[298] Jain, P. K.; Huang, X.; El-Sayed, I. H.; El-Sayed, M. A. *Plasmonics* **2007**, *2*, 107.

[299] Yang, Y.; Matsubara, S.; Nogami, M.; Shi, J.; Huang, W. *Nanotechnology* **2006**, *17*, 2821.

[300] Ko, H.; Singamaneni, S.; Tsukruk, V. V. *Small* **2008**, *4*, 1576.

[301] Jana, N. R.; Pal, T. *Adv. Mater.* **2007**, *19*, 1761.

[302] (a) Xu, H.; Bjerneld, E. J.; Kall, M.; Borjesson, L. *Phys. Rev. Lett.* **1999**, *83*, 4357. (b) Moyer, P. J.; Schmidt, J.; Eng, L. M.; Meixner, A. J. *J. Am. Chem. Soc.* **2000**, *122*, 5409. (c) Haslett, T. L.; Tay, L.; Moskovits, M. *J. Chem. Phys.* **2000**, *113*, 1641.

[303] (a) Nie, S. M.; Emery, S. R. *Science* **1997**, *275*, 1102. (b) Kneipp, K.; Wang, Y.; Dasari, R. R.; Feld, M. S. *Appl. Spectrosc.* **1995**, *49*, 780. (c) Kneipp, K.; Wang, Y.; Kneipp, H.; Perelman, L. T.; Itzkan, I.; Dasari, R. R.; Feld, M. *Phys. Rev. Lett.* **1997**, *78*, 1667. (c) Nie, S. M.; Doering, W. *J. Phys. Chem. B* **2002**, *106*, 311.

[304] (a) R. P. Van Duyne, In *Chemical and Biochemical Applications of Lasers*, C. B. Moor, Ed.; Academic Press: New York, 1979; Vol 4, pp 101-185. (b) Moskovits, M. *Rev. Mod. Phys.* **1985**, *47*, 783.

[305] Campion, A.; Ivanecky, J. E.; Child III., C. M.; Foster, M. C. *J. Am. Chem. Soc.* **1995**, *117*, 11807.

[306] Qian, X.-M.; Nie, S. M. *Chem. Soc. Rev.* **2008**, *37*, 912.

[307] Lassiter, J. B.; Aizpurua, J.; Hernandez, L. I.; Brandl, D. W.; Romero, I.; Lai, S.; Harfner, J. H.; Nordlander, P.; Halas, N. J. *Nano Lett.* **2008**, *8*, 1212.

[308] Huang, W.; Qian, W.; Jain, P. K.; El-Sayed, M. A. *Nano Lett.* **2007**, *7*, 3227.

[309] Jain, P. K.; Huang, W.; El-Sayed, M. A. *Nano Lett.* **2007**, *7*, 2080.

[310] (a) Xu, H.; Bjerneld, E. J.; Kall, M.; Borjesson, L. *Phys. Rev. Lett.* **1999**, *83*, 4357. (b) Moyer, P. J.; Schmidt, J.; Eng, L. M.; Meixner, A. J. *J. Am. Chem. Soc.* **2000**, *122*, 5409. (c) Haslett, T. L.; Tay, L.; Moskovits, M. *J. Chem. Phys.* **2000**, *113*, 1641.

[311] (a) Nie, S. M.; Emery, S. R. *Science* **1997**, *275*, 1102. (b) Kneipp, K.; Wang, Y.; Kneipp, H.; Perelman, L. T.; Itzkan, I.; Dasari, R. R.; Feld, M. *Phys. Rev. Lett.* **1997**, *78*, 1667. (c) Nie, S. M.; Doering, W. *J. Phys. Chem. B* **2002**, *106*, 311.

[312] (a) R. P. Van Duyne In *Chemical and Biochemical Applications of Lasers*, C. B. Moor, Ed.; Academic Press: New York, 1979; Vol 4, pp 101-185. (b) Moskovits, M. *Rev. Mod. Phys.* **1985**, *47*, 783.

[313] Campion, A.; Ivanecky, J. E.; Child III., C. M.; Foster, M. C. *J. Am. Chem. Soc.* **1995**, *117*, 11807.

[314] Qian, X.-M.; Nie, S. M. *Chem. Soc. Rev.* **2008**, *37*, 912.

[315] Lassiter, J. B.; Aizpurua, J.; Hernandez, L. I.; Brandl, D. W.; Romero, I.; Lai, S.; Harfner, J. H.; Nordlander, P.; Halas, N. J. *Nano Lett.* **2008**, *8*, 1212.

[316] Huang, W.; Qian, W.; Jain, P. K.; El-Sayed, M. A. *Nano Lett.* **2007**, *7*, 3227.

[317] Jain, P. K.; Huang, W.; El-Sayed, M. A. *Nano Lett.* **2007**, *7*, 2080.

[318] Tiwari, V. S.; Oleg, T.; Darbha, G. K.; Hardy, W.; Singh, J. P.; Ray, P. C. *Chemical Physics Letters* **2007**, *446*, 77.

[319] Hunyadi, S. E.; Murphy, C. J. *Journal of Materials Chemistry* **2006**, *16*, 3929

[320] Jain, P. K.; Eustis, S.; El-Sayed, M. A. *J. Phys. Chem. B* **2006**, *110*, 18243.

[321] Jain, P. K.; El-Sayed, M. A. *Journal of Physical Chemistry C* **2008**, *112*, 4954.

[322] Vidhu, S. T.; Tovmachenko, O.; Gopala, K. D.; William, H.; Singh, J. P.; Paresh, C. R. *Chem. Phys. Lett.* **2007**, *446*, 77.

[323] Westcott, S. L.; Oldenburg, S. J.; Lee, T. R.; Halas, N. J. *Chemical Physics Letters* **1999**, *300*, 651.

[324] Wang, H.; Brandl, D. W.; Le, F.; Nordlander, P.; Halas, N. J. *Nano Letters* **2006**, *6*, 827.

[325] Xu, S.; Zhao, B.; Xu, W.; Fan, Y. *Coll. Surf. A: Physiochm Eng. Aspects* **2005**, *257*, 313.

[326] Wang, W.; Ruan, C.; Gu, B. *Analytica Chimica Acta* **2006**, *567*, 121.

[327] Becker, M.; Sivakov, V.; Gösele, U.; Stelzner, T.; Andrä, G.; Reich, H. J.; Hoffmann, S.; Michler, J.; Christiansen, S. H. *Small* **2008**, *4*, 398.

[328] Lee, S. J.; Baik, J. M.; Moskovits, M. *Nano Lett.* **2008**, *8*, 3244.

[329] Fang, P-P.; Li, J-F.; Yang, S-L.; Li, L-M.; Ren, B.; Tian, Z-Q. *Journal of Raman Spectroscopy* **2008**, *39*, 1679.

[330] Gunawidjaja, R.; Peleshanko, S.; Ko, H.; Tsukruk, V. V. *Adv. Mater.* **2008**, *20*, 1544.

[331] (a) Li, X.; He, S. *Nanotechnology* **2008**, *19*, 355501. (b) Vial, S.; Pastoriza-Santos, I.; Perez-Juste, J.; Liz-Marzan, L. M. *Langmuir* **2007**, *23*, 4606. (c) Ding, H.; Yong, K.-T.; Roy, I.; Pudavar, H. E.; Law, W. C.; Bergey, E. J.; Prasad, P. N. *J. Phys. Chem. C* **2007**, *34*, 12552.

[332] (a) Leonov, A. P.; Zheng, J.; Clogston, J. D.; Stern, S. T.; Patri, A. K.; Wei, A.; *ACS Nano* **2008**, *2*, 2481. (b) Koo, H. Y.; Choi, W. S.; Kim, D.-Y. *Small* **2008**, *4*, 742. (c) A. Gole; Murphy, C. J. *Langmuir* **2005**, *21*, 10756. (d) Jiang, C.; Tsukruk, V. V. *Soft. Matter* **2005**, *1*, 334.

[333] Ko, H.; Chang, S.; Tsukruk, V. V. *ACS Nano* **2009**, *3*, 181.

[334] Chen, C.; Wang, L.; Jiang, G.; Zhou, J.; Chen, X.; Yu, H.; Yang, Q. *Nanotechnology* **2006**, *17*, 3933.

[335] Schider, G.; Krenn, J. R.; Hohenau, A.; Ditlbacher, H.; Leitner, A.; Aussenegg, F. R. *Phys. Rev. B* **2003**, *68*, 155427.

[336] Brioude, A.; Pileni, M. P. *J. Phys. Chem. B* **2005**, *109*, 23371.

[337] Jiang, C.; Markutsya, S.; Tsukruk, V. V. *Langmuir* **2004**, *3*, 882.

[338] Gunnarsson, L.; Rindzevicius, T.; Prikulis, J.; Kasemo, B.; Käll, M.; Zou, S.; Schatz, G. C. *J. Phys. Chem. B.* **2005**, *109*, 1079.

[339] Hussain, I.; Brust, M.; Barauskas, J.; Cooper, A. I. *Langmuir* **2009**, *25*, 1934.

[340] Markutsya, S.; Jiang, C.; Pikus, Y.; Tsukruk, V. V. *Adv. Funct. Mater.* **2005**, *15*, 771.

[341] Zong, R.-L.; Zhou, J.; Li, Q.; Du, B.; Li, B.; Fu, M.; Qi, X.-W.; Li, L.T.; Buddhudu, S. J. Phys. Chem. B 2004, 108, 16713.

[342] Hildenbrandt, P.; Stockburger, M. *J. Phys. Chem.* **1984**, *88*, 5935.

[343] Mohanty, P.; Yoon, I.; Kang, T.; Seo, K.; Varadwaj, K. S. K.; Choi, W.; Park, Q-H.; Ahn, J. P.; Suh, T. D.; Ihlee, H.; Kim, B. *J. Am. Chem. Soc.* **2007**, *129*, 9576.

[344] Lee, S. J.; Baik, J. M.; Moskovits, M. *Nano Lett.* **2008**, *8*, 3244.

[345] Yoon, I.; Kang, T.; Choi, W.; Kim, J.; Yoo, Y.; Joo, S-W.; Park, Q-H.; Ihlee, H.; Kim, B. *J. Am. Chem. Soc.* **2009**, *131*, 758.

[346] Jeong, D. H.; Zhang, Y. X.; Moskovits, M. *J. Phys. Chem. B.* **2004**, *108*, 12724.

[347] Hildenbrandt, P.; Stockburger, M. *J. Phys. Chem.* **1984**, *88*, 5935.

[348] Tao, A. R.; Yang, P. *J. Phys. Chem. B Lett.* **2005**, *109*, 15687.

[349] John R. Ferraro, Kazuo Nakamoto, Chris W. Brown, "Introductory Raman Spectroscopy," Second Edition, Elsevier 2003.

[350] Brioude, A. ; Pileni, M. P., *J. Phys. Chem. B*, **2005**, *109*, 23371.

[351] Jayaraman, S.; Edwards, R. L.; Hemker, K. J. *J. Mater. Res.* **1999**, *14,* 688.

[352] Steven C. Chapra, Raymond P. Canale, "Numerical Methods for Engineers with Programming and Software Applications", Third Edition, McGraw-Hill, 1998.

[353] J. P. Den Hartog, Advanced Strength Materials, Dover, New York 1952.

[354] Volynskii, A. L.; Bazhenov, S. Lebeda, O. V.; Bakeev., N. F. *J. Mat. Sci.* **2000**, *35*, 547.

[355] Bhagwan D. Agarwal, Lawrence J. Broutman, "Analysis and Performance of Fiber Reinforced Composites", Second Edition, John Wiley and Sons 1990.

[356] (a) Celzard, A.; McRae, E.; Deleuze, C.; Dufort, M.; Gurdin, G.; Mareche, J. F. *Phys. Rev B* **1996**, *53*, 6209. (b) Balberg, I. *Phys. Rev. B* **1986**, *33*, 3618. (c) Balberg, I. *Philos. Mag B* **1987**, *56*, 991.

[357] Balberg, I. *Phys. Rev. B* **1985**, *31*, 4053.